Iron-Based, Freestanding Films Fabricated by Magnetron Sputtering for Biodegradable Implant Applications

Submitted in partial fulfillment of the requirements for
the degree of Doctor of Engineering
(Dr.-Ing.)

Kiel University,
Institute for Material Science,
Chair for Inorganic Functional Materials

Dissertation
by Till Jurgeleit

2018

Declaration

I hereby declare that I wrote this dissertation by myself and to the best of my knowledge and belief, and used none but the indicated sources.

Till Jurgeleit
Christian-Albrechts-Universität zu Kiel

Place, Date

Signature

Supervisor:

Dr. rer. nat. Christiane Zamponi

Reviewers:

Prof. Dr.-Ing. Eckhard Quandt
Prof. Dr. rer. nat. Lorenz Kienle

Date of the disputation
27.08.2018

Contents

1 Abstract

In the recent decade biodegradable metallic materials became subject of intense research. Those biodegradable metals are of interest for the intended use as temporary implants. Such implants are always beneficial if they do not have to replace a body function for the whole life of the patient, but serve its purpose for a certain healing period. After the healing a permanent implant is just a foreign body and involves the risks for complications like inflammation, tissue necrosis and thrombosis etc. The most prominent biodegradable metals are magnesium-based and iron-based material, but also zinc-based material have been proposed. The advantage of iron based material is its degradation without significant hydrogen evolution and its high mechanical strength. Iron-based material is mainly proposed for the fabrication of vascular implants like (stents). However, first in vivo studies showed that the degradation occurs too slow. Additionally the ferromagnetic nature of iron can become a problem when it comes to magnetic resonance imaging. Thus, the research goal formulated by the pioneers in the field are to accelerate the degradation time and to get rid of the ferromagnetic properties. In order to accelerate the degradation different approaches are possible. If the geometry of an implant is not or just partially determined by its function, the design and thus the relative surface is one option to accelerate the degradation. Of course the freedom of design depends also on the mechanical properties because a high strength allows more filigree structures. Furthermore, thinner struts are anyways beneficial because less foreign material is brought into the body. The second option to decrease the degradation time is to modify the corrosion rate itself. To increase the mechanical strength and decrease the degradation time, besides the modification of the microstructure by changing the composition, there is also the demand for alternative fabrication methods.
For this reason it is shown in this work, that magnetron sputtering in combination with a geometrical structuring by UV-lithography is a feasible and promising method as a new fabrication process for biodegradable implants. There are various reasons for using this method. First of all sputtered material exhibits a unique microstructure and in turn material properties. Furthermore, it is possible to deposit all types of alloys and allows even the combination with non-compound forming systems, that can not be produced with conventional casting methods. This offers a large number of possible design strategies for the material. Due to the structuring by UV-lithography, the geometrical forming of the devices is done in situ. Thus, there are no forming processing steps necessary such as laser cutting that would influence the microstructure and material properties. Besides structuring by UV-lithography allows the realization of very filigree structures and thus offers a large freedom of design.
In the work structured pure iron, iron-gold and binary FeMn alloys with different Mn contents are successfully fabricated by magnetron sputtering and characterized. For the characterization of the microstructure X-ray diffraction (XRD), transmission electron microscopy (TEM), scanning electron microscopy (SEM), energy dispersive X-ray spectroscopy (EDX) was applied. In addition, the mechanical properties were determined by uniaxial tensile tests. Electrochemical polarization and immersion test were performed in Hanks solution in order to determine the corrosion rates. Furthermore, vibrating sample magnetometry was used in order to characterize the material in terms of its magnetic properties.
It was found that in general the sputtered material exhibits a high mechanical strength compared to literature values for comparable materials. This is mainly attributed to the fine grained microstructure of sputtered material. A significant acceleration of the corrosion rates were reached by the addition of gold, due to the formation of micro galvanic elements. Against expectations

the corrosion rates of FeMn alloys were found to be slower than pure iron. However, the low corrosion rate is compensated by the superior strength up to 1242 MPa. Additionally it was shown that the Mn concentrations > 15 % are sufficient in order to stabilize the non- ferromagnetic ϵ and γ phase and in turn distinctly enhance the magnetic resonance imaging compatibility of the material.
The work proofed the concept of using magnetron sputtering in combination with UV-lithography as promising alternative fabrication method of filigree structured, biodegradable iron based implants. Due to the advantages, the method offers a great potential to tailor the material properties.

Seit dem vergangenen Jahrzehnt sind biodegradierbare metallische Materialien Gegenstand intensiver Forschung. Biodegradierbare Metalle sind für die Verwendung in temporären Implantaten von Interesse und kommen dann zum Einsatz, wenn ein Implantat seine Funktion nur während einer gewissen Heilungsperiode erfüllt und nicht eine bestimmte Körperfunktion für das gesamte Leben des Patienten ersetzen muss. Nach der Heilung stellt ein solches Implantat lediglich einen Fremdkörper da. Somit birgt es auch die Gefahr von Gesundheitsrisiken wie zum Beispiel Entzündungen, Gewebenekrosen und Thrombosen etc. Die bekanntesten biodegradierbaren Metalle sind magnesium- und eisen-basierte Materialien. Der Vorteil von eisenbasierten Materialien ist die hohe mechanische Festigkeit und die Zersetzung ohne signifikanter Wasserstoffentwicklung. Die eisenbasierten Materialien werden auf Grund des E-Moduls hauptsächlich für vaskuläre Implantate wie Stents empfohlen. Erste in vivo Studien haben jedoch gezeigt, dass die Auflösung solcher Stents zu langsam erfolgt. Darüber hinaus stellt die ferromagnetische Natur von Eisen ein Problem da, im Hinblick auf Magnet Resonanz Tomographie Untersuchungen. In einer solchen Untersuchung stellt ein implantiertes ferromagnetisches Material ein Gesundheitsrisiko für den Patienten da.
Daher wurde als Forschungsziel für derartige Materialien, die Beschleunigung der Auflösungszeit sowie die Beseitigung der ferromagnetischen Eigenschaften formuliert. Um eine beschleunigte Auflösung zu erreichen sind verschiedene Ansätze denkbar. Sofern die Geometrie eines Implantats nicht durch seine Funktion vorgegeben wird, bietet eine Modifikation des Designs bzw. der relativen Oberfläche eine Möglichkeit um die Auflösung zu beschleunigen. Natürlich hängen die Freiheiten bei der Gestaltung des Designs nicht zuletzt von den mechanischen Eigenschaften ab, da eine höhere Festigkeit die Realisierung filigranerer Strukturen erlaubt. Weiterhin sind feinere Strukturen ohnehin wünschenswert da somit weniger Fremdmaterial in den Körper eingebracht wird, welches sich zersetzen muss. Die zweite Möglichkeit die Auflösung zu beschleunigen, ist die Beeinflussung der Korrosionsrate selbst. Um eine erhöhte mechanische Festigkeit und beschleunigte Auflösung zu erreichen, sind neben der Modifizierung der Mikrostruktur und Materialzusammensetzung, auch die Erforschung alternativer Herstellungsmethoden von großer Wichtigkeit.
Aus diesem Grund wird in dieser Arbeit gezeigt, dass Magnetron-Kathodenzerstäubung (Sputtern) in Kombination mit UV-Lithografie, eine geeignete Methode zur Herstellung von Eisen basierten biodegradierbaren Implantaten darstellt. Die Nutzung dieser Art der Herstellung bietet viele Vorteile. Zunächst einmal besitzt gesputtertes Material eine einzigartige Mikrostruktur und somit auch Materialeigenschaften. Darüber hinaus können neben der Abscheidung aller Arten von Legierungen auch Systeme aus nicht mischbaren Komponenten hergestellt werden. Dies bietet eine große Freiheit bei der Herstellungsstrategie des Materials. Weiterhin erlaubt die Strukturierung mittels UV-Lithografie die in situ Formgebung während der Materialabscheidung. Hierdurch werden formgebende Schritte wie Laserschneiden, welche die Mikrostruktur bzw. die Materialeigenschaften beeinflussen können, obsolet. Die Strukturierung mittels UV-Lithografie bietet auch die Möglichkeit zur Herstellung sehr feiner Strukturen und bietet so eine große Freiheit im Design. In dieser Arbeit wurden strukturierte Filme aus Reineisen, Eisen-Gold sowie verschiedene binäre Eisen-Mangan Legierungen erfolgreich hergestellt und charakterisiert. Für die Mikrostrukturanalyse wurden Untersuchungen durch Röntgenbeugung, Transmissions- und Raster-Elektronenmikroskope sowie energiedispersive Röntgenspektroskopie genutzt. Weiterhin wurden die mechanischen Kennwerte im uniaxialen Zugversuch ermittelt. Die Korrosionsraten wurden durch elektrochemische Polarisationsmessungen und Immersionstest bestimmt. Drüber hinaus wurden die magnetischen Eigenschaften des Materials mittels Vibrationsmagnetometrie untersucht.
Es wurde gezeigt, dass im Vergleich zu Literaturwerten vergleichbarer Materialien, das gesputterte Material eine allgemein hohe Festigkeit besitzt. Dies ist hauptsächlich auf die charakteristische feinkörnige Mikrostruktur zurückzuführen. Weiterhin wurde eine signifikante Steigerung

der Korrosionsrate durch das Einbringen von Goldausscheidungen erreicht, da diese als mikrogalvanische Elemente fungieren. Entgegen den Erwartungen, führte das Hinzulegieren von Mn führte zu einer geringfügigen Abnahme der Korrosionsrate. Dies wird jedoch durch die sehr hohe Festigkeit von bis zu 1147 MPa kompensiert. Zusätzlich konnte gezeigt werden, dass Mn Konzentrationen >15 % ausreichen, um die nicht-ferromagnetischen ϵ und γ Phasen zu stabilisieren, was die Materialkompatibilität mit Magnet Resonanz Tomographie Untersuchungen deutlich verbessert.
Die Arbeit zeigt, dass es möglich ist Magnetronsputtern in Kombination mit UV-Lithografie als alternatives Herstellungsverfahren für feinstrukturierte Implantate zu nutzen. Durch die Vorteile dieser Herstellungstechnik erscheint diese als vielversprechend um die Materialeigenschaften gemäß den Anforderungen zu optimieren.

2 Motivation

The history of metallic bio materials used for medical implants reaches far back to the past. Already more than 2000 years ago gold was used in dentistry [Rat+12, p. 1]. In the 16th century a gold plate was used for the treatment of a cleft palate. In the 18th century the first use of gold, iron and bronze wires are reported. Big progress in the development was done in the 20th century. In 1929 Levert investigated the compatibility of different metals in the body. Furthermore first screws and plates made of steel were used for the fixation of bone fractures. This early used steels on one hand exhibited good mechanical properties in comparison with novel metal implants, however they were not able to compete in terms of biocompatibility and corrosion resistance. This problems were overcome with the invention of stainless CrNi steels and the development of CoCr and Ti alloys in the 20th century. With this innovations even more complex implants like artificial hips and joint prosthesis have been realized [ES08, p.183 ff]. These developments also enabled andvance in the treatment of cardiovascular diseases by catheterization that was first done by Forsmann in 1929 and resulted in the invention of cardiovascular stents in 1987 [RT95]. [Her12, p. 23]
In general it can be distinguished between two classes of implants, those who completely replace or support a body function for the whole life and those who serve its purpose just during a certain healing period. Examples for the first category are artificial joints, pacemaker or dental implants. To the second class belong bone screws, plates and wires are assigned. Even vascular stents do not have a significant positive influence after a certain healing period of 6-12 months. Quite contrary after remodeling of the vessel tissue a stent involves the danger of complications like late stent restenosis, inflammation or tissue necrosis [CK00] [Kim+96] [Peu+01]. Since every implant is a foreign body the risk of complications due to immune response is a general problem. To solve this problem there are two options. The first is to enhance the biocompatibility of an implant to such an extent, that complications can be excluded. The second option is the removal of the implant. While complications can never be excluded 100% the removal of implants that are not longer required is common practice. But even the removal of implants involves risks for the patient due to the followup surgery. Even worse are the problems that arises with the treatment of narrowed blood vessels of children. Since the the vessels growths also the stent needs to growth. This requires either an re dilatation, which is limited to the maximum possible stent diameter, or the removal of the stent. To prevent those risks an alternative option is to use implants that degrade by their own due to chemical or biological interactions with the environment. Another important application is the use of biodegradable suture material that makes an follow surgery for pulling the stitches obsolete. The history of those biodegradable materials probably started already with the discovery of elemental magnesium by Sir Humphery Davy in 1808. Still in the same century Edward Huse reported in 1878 on the degradable properties of Mg wires [Wit10]. In the recent years an increased interest in those biodegradable materials have led to an intense research in the field (chapter 3).
Since the beginnings biodegradable materials became a distinct field of research in material science. Since the 1960s, besides metals also polymers are studied for the use as biodegradable implants. Especially poly(lactides) and poly(glycoles) but also a number of other polymers are meanwhile used for biodegradable medical devices. An advantage of biodegradable polymers are the various options to tailor degradation behavior by influencing the molecule structure [MT00]. However a drawback of polymers is there limited mechanical strength, and in turn limited applications for load bearing implants. Hence, they are especially used as degradable

material for medical sutures. Polymers have also been used for other load bearing implants, however a larger strut sizes are required compared metallic implants. In turn also the field of application is narrowed, especially when it comes to small vessels or filigree bones. Thus, especially for vascular scaffolds and orthopedic fracture fixation the interest on biodegradable metals increased in the past decade. The most promising biodegradable metals are Mg and Fe. However also zinc have been proposed as a possible candidate. The selection is mainly determined by the toxicity of both the original material and the degradation products. Since all of the named elements are essential elements in the human metabolism they are prinicipally feasible for the intended use as biodegradable implants [HWS15]. Nevertheless in in terms of the toxicity it has to be considered what already Paracelsus proclaimed in 1538 [Par65, p. 510]:

> *All substances are poisons; there is none which is not a poison. The right dose differentiates a poison and a remedy* (translated, Paracelsus, 1538)

Therefore, the size of an implant and in turn the amount of material that is brought into the body plays an essential role for biodegradable implants. Furthermore the degradation speed determines the dose of degradation products that are released from the implant. Thus the properties strength and degradation speed are the key properties for biodegradable metals. Of course in terms of the material properties there are big differences between the suggested metals. The most importand differences between Mg and Fe are the strength, degradation speed and the degradation reaction itself. Mg exhibits an low strength and a much higher degradation speed in comparison to Fe. In general the research on Mg based material is focused on the deceleration of the degradation whereas it should be accelerated for Fe. In contradiction to Fe, Mg tends to the formation of gaseous H_2 during the degradation in physiological solutions [HWS15] [Wit+08].
These material properties also determine the field of applications, due to their distinct requirements. For orthopedic applications besides the strength, also the Young's Modulus E plays an important role. It should be as close as possible to the Young's modulus of bone. If it is too high a phenomenon called stress shielding is observed due to the transfer of stresses in the stiffer implant. As a result the bone can become less dens and weaker around an implant. Therefore, Mg alloys show the more promising properties compared to Fe, because its Young'ss Modulus modulus (44 GPa – 45 GPa) [Her12, p. 16] is more close to bone (10 GPa – 20 GPa) than the Young's modulus of Fe (190 GPa) [Her12, p. 16]. Also the formation of H_2 was found being less problematic in orthopaedic application [Wit10] [HWS15].
In contrast, the H_2 formation of Mg alloys is a clear disadvantage when it comes to cardiovascular applications due to the formaton of subcutaneous gas cavities. Those gas cavities can accumulate, damage the vessel and interfere the healing process [Wit10]. Additionally, the high strength and stiffens of Fe-based materials is beneficial for cardiovascular applications. High strength materials supply an higher radial force and therefore can resist the elastic recoil of larger vessels.
Further more, the higher strength allows the reduction of the strut size of a stent which allows the treatment of smaller vessels. This could even eneable the treatment of children with congenital heart disease [AL13]. In general thinner struts are a beneficial feature of cardiovascular implants because it was shown, that thinner struts reduces the risk for restenosis and in turn directly improve the treatment outcome [OC09]. In terms of biodegradable stents thinner struts mean that less material has to degrade which reduces the probability for degradation products to reach a toxic dose. Furthermore, a higher strength increases the freedom of design and in turn allow a tailoring of the degradation rate by adjusting the relative surface. Therefore, besides the toxicity a high strength is a general desired, and probably most important feature for biodegradable stent materials.
It is also necessarry to make a stent visible during and after supply. Therefore, in cardiovascular applications even the X-ray visibility is an important feature, which is distinctly higher for Fe than for Mg [OC09]. However, a disadvantage is the ferromagnetic behavior of pure Fe. A

ferromagnetic material can lead to complications in magnet resonance imaging (MRI) treatments that have become an indispensable diagnosis tool of the modern medicine. Possible complications reach from image artifacts up to health risks such as magnetic induced heating or even torques acting on the implant and thus can lead to injuries of the surrounding tissue. Therefore, research to tailor the magnetic properties by alloying with suitable elements is required. Due to the named advantages, Fe-based materials show a great potential for the use as biodegradable vascular implants and hence are the topic of this work [Her12, 13 ff.][HWS15].
The following chapter reviews the research effort that have been done in the field so far.
This work is part of the project "Biodegradierbare einenbasierte Schichten für medizinische Anwendungen " (ZA748/2-2) founded by the Deutsche Forschungsgemeinschaft (DFG).

3 Iron based biodegradable implants, state of the art

In this chapter a summary of the literature is given that was published in the field of biodegradable Fe based material. Since this work is written from a material science point of view, thus also this section is focused on material scientific aspects, never the less bio-medical aspects are also discussed briefly.

As above mentioned, Fe is an essential trace element in the human metabolism. An average adult requires approximately 20 mg Fe per day. Most of the Fe is required for the hemoglobin synthesis. Furthermore, it is a constituent of different proteins and essential for the survival and proliferation of the most cell types [HMA04] [Lie+01]. However, there is no active excretion pathway for Fe. Therefore, a continuous uptake of Fe, exceeding 1–2mg per day will lead to an Fe overload and Fe toxcicity. Such an overload causes organ damage in liver, heart, pancreas, thyroid, and the central nervous system [Koh+08].
The first biodegradable pure Fe stent (NOR-I, Devon Medical) was presented by Peuster et al. in 2001 and specified with a weight of 41 mg considering this and the desired degradation time of 6–12 months [Peu+01] the released Fe amount would be ≤ 0.2 mg per day and therefore far below the limit specified above. Peuster et al. proofed the innocuousness in their early study in vitro as well as in vivo. The stent was implanted in the descending aorta of 16 New Zealand white rabbits in 2001. They found a low thrombogenicity and mild inflammatory response without pronounced neointimal hyperplasia and a lack of local or systemic toxicity. However, the degradation of the stent was found to occur slower than estimated from the in vitro immersion tests. Even 12 months after implantation the stent showed only a slight evidence of corrosion as it can be seen in Fig. 3.0.1[Peu+01].

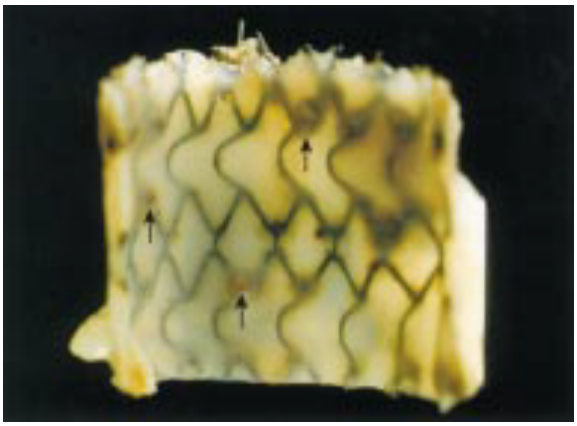

Figure 3.0.1: Rabbit aorta with degradable iron stent 12 months after implantation with numerous pinpoint, slightly raised plaques consisting of corroded stent material highlighted by arrows (with permission of BMJ Publishing Group Ltd. [Peu+01]).

Even the second study of Peuster et al. brought similar results. In this study they implanted pure Fe stents into the descending aorta of 29 minipigs shown in Fig. 3.0.2. After 12 months of implantation they found antithrombotic properties that was attributed to the release of positively

charged Fe ions. They proofed that the treatment did not result in an Fe overload or toxicity and even the accumulation of the corrosion products did not show toxic effects. Furthermore, they reported that in terms of crimping, X-ray visibility and deployment the stent behaved similar to the comeriaclly available stainless steel (SS 316 L) stents [Peu+06]. Thus, Peuster et al. concluded that Fe is a suitable material for degradable large-size stents. Even though they proclaimed that a low corrosion rate (CR) is desirable for degradable vascular stents to prevent embolization due to acute fragmentation of the device, they suggested that further material research should focus on possibilities to accelerate the degradation time. In order to reach this goal they suggested 3 different approaches [Peu+06]:

- Modifing the composition with suitable elements to accelerate the corrosion rate
- Increasing the relative stent surface by a reduction of the strut thickness in order to accalarate the degradation
- Surface modifications that accelarate the degradation

In Fig. 3.0.3 an scheme is given, showing the different approaches that was presented in literature. It can be distinguished between methods that modify the microstructure (grain size and texture) of pure Fe and approaches were the alloying elements or particles are brought into the Fe matrix in order to tailor the microstructure. Besides, also studies were published that aimed for the modification the materials surface, mostly with the purpose to accelerate the degradation rate. Therefore, alternative fabrication methods, alloys, composites and post processing techniques were investigated. It has to be considered that influencing the bulk properties is the more sustainable approach because it changes the material properties of the entire implant and not only in surface near regions that affect the properties just in the initial period of degradation. Thus, the majority of the presented studies focus on the modification of the bulk microstructure.

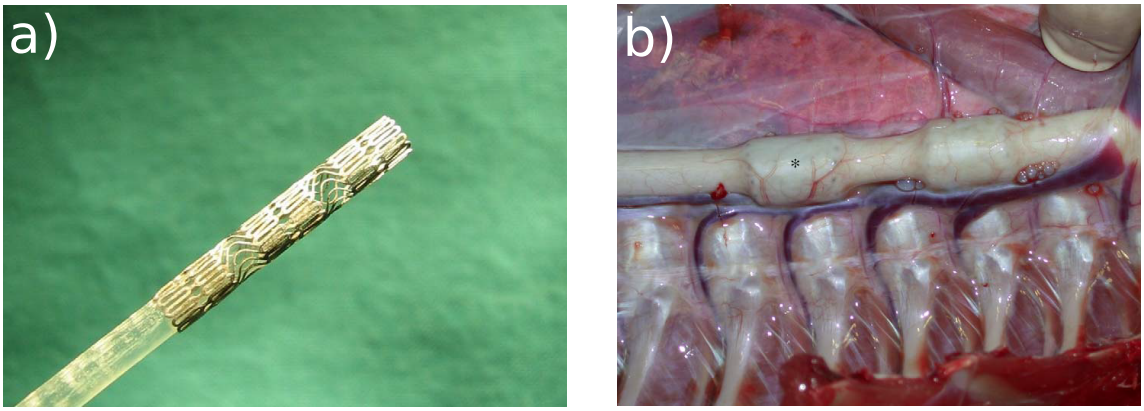

Figure 3.0.2: Image of a) pure Fe stent and b) descending aorta of a minipig with implanted Fe stent (with permission of Elsevier) [Peu+06]).

A compilation of the material properties that are desired for biodegradable vascular implants is provided in Tab. 3.0.1. The ideal biodegradable implant would keep its mechanical integrity until the healing period is completed and immediately disappear afterwards. However, the reality looks different as shown in Fig. 3.0.4.
For the mechanical properties a clear lower limit is defined. Generally it is considered that a high strength and ductility is beneficial for the intended application. The material properties should approach the values other materials that are currently used for vascular implants. The

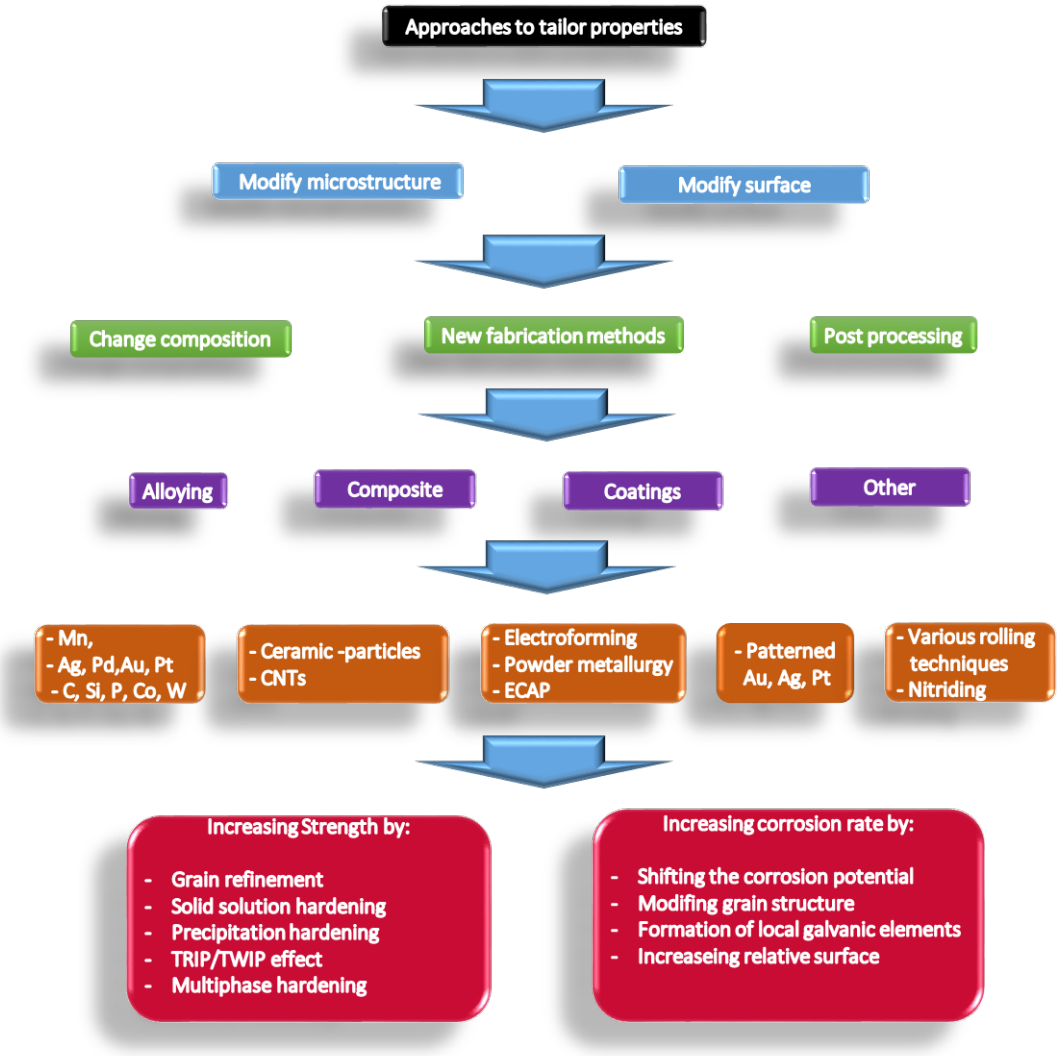

Figure 3.0.3: Scheme of the different approaches presented to improve the relevant material properties of Fe-based biodegradable material.

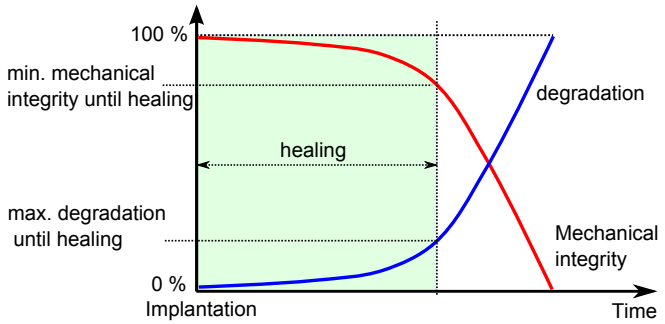

Figure 3.0.4: Schematic relationship between mechanical integrity and degradation progress of an degradable implant over time. The implant has to keep the minimal mechanical integrity required until the healing period is finished. Therefore, there is an maximum degradation progress that should not exceeded to prevent a premature device failure

Table 3.0.1: Desired material properties for degradable vascular implants in terms of strength, ductility, biodegradability

Propertie	Value/Comment
Mechanical integrity	6–12 months (mechanical integrity)[MM11]
Time for degradation	> 6–24 months (as fast as possible)[HDM10]
Yield strength (YS)	> 200 MPa [BDG13]
Ultimate tensile strength (UTS)	> 300 MPa [BDG13]
Fracture strain (A)	> 15–18% [BDG13]
Young's modulus (E)	High enough to retain the radial force necessary to prevent recoil but low enough to archive the a sufficient flexibility nesesarry for the deployment by catheter [HWS15]

Table 3.0.2: Examples for alloys used for vascular implants and their mechanical properties [HRP11]

Material	YS	UTS	A	E
FeCrNiMo (SS 316 L)	190 MPa	490 MPa	40 %	193 GPa
CoNiCrMo	241 MPa	793 MPa	50 %	232 GPa
Pure Ti	485 MPa	550 MPa	15 %	110 GPa

mechanical properties of such materials are presented in Tab. 3.0.2. However, no clear number is given for the degradation time or the CR.

In terms of the biodegradability most studies compare their results to self determined pure - Fe reference values or those reported in literature. However, the reported values and comparisons have to be assessed very critical. In literature a wide range of in vitro testing methods and conditions is found. Hence, it is not possible to make a direct assessment if the the biodegradable properties of a material meets the requirements or not. In vitro tests will never mimic the living system to 100 %. Nonetheless, those tests give an important hint how a material could or should behave in the body. Therefore these in vitro test are even important to make pre-clinical in vivo test in the animal model ethically acceptable.

In the following pages the studies published in the field of biodegradable Fe-based material and their major findings are reviewed and summarized, beginning with the most simplest pure-Fe system. Since there is a large number of comprehensive studies with broad sets of experimental parameters the results are described rather qualitatively. However, a summary of the values of the corrosion properties and mechanical properties are presented in detail in Tab. 3.0.5 and Tab. 3.0.4.

Pure Fe

Moravej et al. presented in multiple publications [Mor+10a][Mor+10b][MM11] electro forming as a feasible method for the fabrication of biodegradable pure Fe (E-Fe). They showed that the materiel fabricated by the methode exhibits a highly (110) textured fine grained structure of the as deposited (adp) material. With annealing the degree of texture decreased. The CR were decreased by annealing but were found to be still significantly higher than the cast pure Fe reference. The authors suggested that the decreasing CR is attributed to the lower degree of (110) texture for the annealed samples and reduced amount of defects that act as corrosion sites. Also the higher CR of the annealed samples was related to an higher defect density, compared to cast material. The defect-rich structure was shown to improve the strength of the material. By annealing an higher strength compared to the cast material was achieved accompanied with

a large ductility [Mor+10a]. Indeed the authors commented that the amount of impurities can affect the mechanical properties, however the influence of the rather high overall impurity concentrations (0.25 wt%) on the corrosion behavior is not discussed.

In a further work Moravej et al. showed that varying of the deposition conditions of Fe (E-Fe) influences texure and grain structure. This led to significant changes in the initial CR determined by electro chemical measurements. However, the long term CR determined by immersion tests was not affected [Mor+11]. In a studie regarding the in vitro cell viability it was shown that degradable cast-Fe and E-Fe do not significantly inhibit the metabolic activity of smooth muscle cells (SMC) similar to the SS 316 L standard. Additionally, an decreased proliferation rate of SMC was found and concluded to have beneficial effects in the control of neointimal proliferation when used as stent material [Mor+10b].
Obayi et al. investigated the influence of cross-rolling on the microstructural, mechanical and corrosion properties. They investigated the influence of different rolling techniques (uni directional rolling (UDR) and bidirectional rolling (BDR)) at different degrees of deformation, before and after annealing. It was shown that the deformation texture influences the crystallization behavior and grain size. Thus, a coarser average grain size (19.6 µm) were found for BDR samples compared to the UDR samples(15.2 µm), annealed at the same temperature. This differences in the grain size also effected the material properties because larger grains result in a lower strength. Furthermore, annealing at higher temperature decreases the general defect density and the strength, respectively. It was concluded that the texture of the different rolling techniques do not significantly effect the degradation behavior. However, it was inferred that the larger grain size and defect density of BDR and at higher temperatures annealed samples decreases the degradation rate due to enhanced grain boundary corrosion [Oba+15].
In another work of the same author the influence of the grain size of UDR rolled samples on the mechanical and corrosion properties was investigated. Similar to their previous work, a decreasing strength was found with increasing annealing temperatures and larger grains, respectively. The fracture strain (A) was found to be not significantly effected except for the samples annealed at 1000 °C where a detrimental decrease of the fracture strain was observed. In terms of the corrosion properties contradicting results to the previous study were reported. It was shown in both, electrochemical and immersion tests, that there is a distinct correlation between small grains and low corrosion rates. They explained the behavior with the theory of Ralston et al. [RBD10] which proclaims that a smaller grain size of a pure metal in a passivating environment will lead to a lower corrosion rate. The reason for this is that in a fine grained structure the volume of grain boundaries is higher. Since the diffusion in the grain boundaries is higher than in in the bulk, a passivation layer can be formed more easily, being deeper and more stable. A further suggestion made by the authors is that at higher temperatures (1000 °C) carbide precipitates along the grain boudaries act as active sites for corrosion and in turn accelerate the corrosion [Oba+16]. It has to be assessed critical why those carbide precipitates should form just at 1000 °C and not even at 800 °C. Furthermore the carbon content was reported rather low (0.006 wt%) compared to the overall impurities contents (0.18 wt%). Also it is not clear why the results of the degradation behavior are in contradiction to the previous study although the used material and processing techniques are identical.
The results of the prior study are in good agreement with studies of Nie et al. regarding the surface chemistry, mechanical properties, in vitro corrosion, cytotoxicity and hemocompatibility of nano– (NC) and micro–crystalline (MC) pure Fe, processed by equal channel angular pressing (ECAP). It was shown that NC–Fe corrodes distinctly lower compared to MC–Fe. It was proofed that also the O_2 concentration plays an important role and MC–Fe as well as NC-Fe corrodes much faster in O_2 rich solutions. It was concluded that the NC microstructure is more isotropic than the MC microstructure. Therefore, it allows the formation of stable oxide layers that slows down the corrosion rate and even makes the material less prone to inter granular grain boundary

corrosion and in turn make the corrosion more homogeneous. Due to the processing by ECAP even the tensile strength was significantly enhanced due to the increase of the defect density. Additionally, the studied material inhibited the growth of SMCs and improved the growth of endothelia cells (EC), this beneficial for the control of the neointima proliferation and reduces the thrombogenicity and risk for and restenosis. Also the rupture rate of blood cells (haemolysis) was found to be credible and below 5 % [Nie+10][NZ12]

FeX alloys
Liu et al. studied FeX with 3 % of different elements (Mn, Co, Al, W, Sn, B and S) and investigated the influence on the mechanical, in vitro corrosion and biological properties. It was shown that especially after cold rolling the alloying elements Mn, Co, Al, W, B and S lead to an increased strength and higher or at least comparable ductility compared to pure Fe. Sn as alloying element was found being not suitable due to a detrimental effect on the ductility. A decrease in the corrosion rate was found for all alloying elements except C and S that brought similar results compared to pure Fe. The lowest corrosion rate was found for the FeMn alloy. In terms of the cytotoxicity it was concluded that Co, W, C and S are suitable alloying elements. For the metallic elements that exhibit a better solubility higher concentrations were recommended in order to archive the desired results.
In a comparative study Cheng et al. investigated the feasibility of pure Fe, Mn, Mg, Zn and W as biodegradable implant materials. In terms of the mechanical properties they found that Fe shows the most promising properties. Whereas the degradation speed should lay in between those of Fe and Mg. For Fe, Mg and W no cytotoxic effects were observed. However, a much higher haemolysis rate was found for Mg and a significantly reduced cell viability for Mn. It was concluded that even though pure Mn is not suitable as biodegradable material, it is an ideal candidate as alloying element for Fe based material [Che+13].
$Fe_{81}Ga_{19}$, $(Fe_{81}Ga_{19})_{98}B_2$ and $(Fe_{81}Ga_{19})_{99.5}(TaC)_{0.5}$ alloys were characterized by Wang et al.It was shown that the FeGa alloys corroded faster than pure Fe due to increased pitting corrosion [Wan+17c]. Vojtech et al. reported that FeC and FeF alloys on one hand exhibits a high strength, on the other hand no significant improvement of the degradation properties were reported [VKČ15].

FeMn alloys
In general the FeMn system offers different possibilities to tailor the microstructure and material properties. First of all there are three different crystal modifications possible and each has special properties. In Fig. 3.0.5 a non equilibrium phase diagram ist shown, presenting the relative phase fractions for binary FeMn alloys acording to [Sch67] [Mar+01] [Mar+05] [LJC97]. Whereas at lower Mn concentrations the α' – martensite is the stable phase at room temperature (RT), at higher Mn concentrations a hexagonal (hcp) ε–martensite phase and face centered cubic (fcc) γ–austenite phase is present.

At concentrations approx. 29-35 wt% Mn the γ–phase becomes the predominant phase. Interestingly, the switch between the austenite phase and the martensite modifications can be induced not only thermally but also mechanically. This is the premise for two effects namely the transformation induced plasticity (TRIP) and twinning induced plasticity (TWIP). The two effects are discussed more detailed in subsection 5.2.3. At this point it should just be stated that they are similar in their principle and result in a high strength and ductility [Bou+11]. Additionally the next argument of Mn as alloying element is its normal potential. In general it is assumed that a lower normal potential (U_0) results in a higher corrosion rate. In Tab. 3.0.3 U_0 values for some pure metals are summarized. It is obvious, that Mn has a distinct lower normal potential than Fe and should degrade faster. Even when used as an alloying element, Mn will decrease the normal potential of the alloy. Finally the last reason are the magnetic properties of FeMn. It

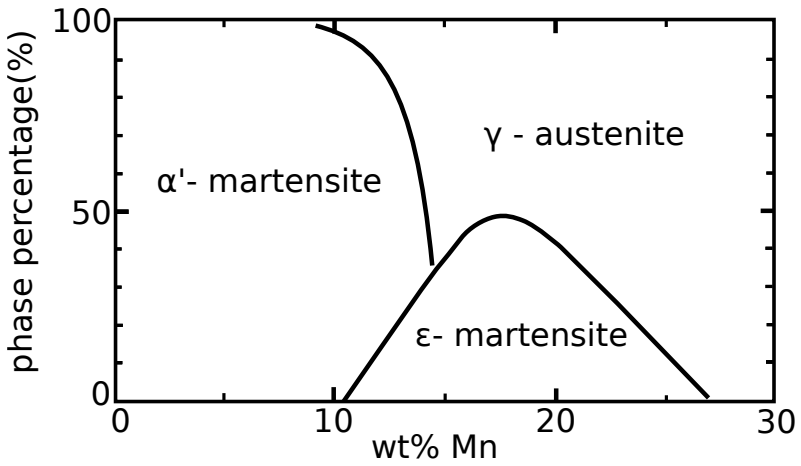

Figure 3.0.5: Relative phase fractions for binary FeMn alloys (with permission, according to [Sch67][Mar+01][Mar+05][LJC97])

was already stated that one problem of Fe as biodegradable implant material is its ferromagnetic nature, because it becomes a problem in MRI investigations and can lead to image artifacts and health risks. Therefore the magnetizability and susceptibility should be as low as possible. The role of the magnetic susceptibility in MRI is nicely reviewed by Schenck [Sch96]. He defines MRI compatibility of first kind as followed:

Table 3.0.3: Literature values of normal potentials U_0 [Lid10, pp. 8–20]

Element	U_0 (V)
Fe	-0.44
Mn	-1.18
Au	1.69
Pd	0.91
Pt	1.11
Ag	0.79

$$10^{-5} < |\chi - \chi_{water}| < 10^{-2} \tag{3.0.1}$$

Were χ stands for the magnetic susceptibility and $\chi_{water} = -9.05 \cdot 10^{-6}$.

As a consequence, non–ferromagnetic behavior is desired. It is known that most of the austenitic stainless steels are non–ferromagnetic [LSL09]. Therefore, in terms of the magnetic properties of implant materials there is a great interest to stabilize an austenitic structure at RT, by alloying with suitable elements. Some of the most common austenite formers are Mn and Ni. Since Ni is classified as potentially cancerogenic to humans [McG+00] it is inappropriate as alloying element. Besides, the FeMn γ–phase that show antiferromagnetic behavior, and also the ε–phase was found to be paramagnetic [SON86][CSG95]. In turn regarding the magnetic properties especially the composition range with Mn concentrations 10-30% are of interest because in these composition range a phase composition of ε – martensite and γ–austenite is expected (Fig. 3.0.5).
An additional argument for Mn as alloying element, is its role as essential trace element in humans and all mammals. The average daily intake ranges from 2 to 9 mg/d. However, it has to be considered that there are also worries about toxic effects of Mn after excess intake. The

intravenous daily dose should not exceed 500 µg/d [SS10]. [CZ04] Consulting the above discussed example: a stent like the pure Fe NOR-I stent with 41 mg and a hypothetical Mn concentration of 30 wt% that continuously degrade over 6–12 months, would lead to a daily release of approx. 67 µg/d which is far below the above specified limit.

Summarized, Mn is a very promising alloying element for biodegradable Fe–based material in terms of mechanical, corrosion, magnetic and biological properties. In order to exploit the full potential the Mn concentration should be chosen as low as possible and as high as necessary. In 2008 Hermawan et al. presented for the first time binary FeMn alloys for biodegradable applications [Her+08] [HDM08]. It was shown that FeMn alloys with different Mn concentrations (20, 25, 30 and 35 wt %) can be fabricated via powder sintering and cold rolling. All tested materials showed a higher strength compared to pure Fe decreasing with the Mn content. Since the FeMn20/25 samples showed a multiphase ε/γ structure the increased strength was attributed to the strengthening effect of the phase boundaries. Furthermore, they showed for the FeMn20/25 that an strain induced $\gamma \rightarrow \varepsilon$ (TRIP effect subsection 5.2.3) occurs which also contributes to the high strength. Even the degradation were observed to be faster than in pure Fe but decreasing with higher Mn content, due to the more homogeneous phase structure of the FeMn20/25 samples. The influence of the impurities and porosity however is not discussed. All investigated alloys showed non ferromagnetic behavior [HDM08]. Since the FeMn30/35 alloy showed over all the largest potential for the use as biodegradable implant they investigated in a follow up study the FeMn35 alloy more detailed.

It was found that FeMn35 fabricated by powder sintering and cold rolling exhibits an exclusively austenitic γ structure and was found to have antiferromagnetic properties. The saturation magnetization and susceptibility was even lower compared to the SS 316 L gold standard. Also promising results in terms of the mechanical properties were found. The values approached those of the SS 316 L. Furthermore the initial degradation of the material was found to be much faster than pure Fe. Even though the corrosion rate decreased strongly after the different sintering steps it was still higher compared to pure Fe [Her+08]. However, it seems to be the case that a large part of the influence can be attributed to the high porosity and inclusions of initially over 17 %. Even for the most dense material after the third processing step showed still 0.3 % porosity and 2 % of MnO particles were reported.

Based on these first promising results a number of studies have been published investigating the influence of different Mn concentrations in the range of 20 to 35 %. Most of them studied the influence of different processing routes or alternative fabrication methods. Majorly it was concluded that FeMn alloys exhibits an higher strength and degrades faster than pure Fe based on electrochemical tests [Cho+13][Hei+15b][Sin+15][Hei+15a][Cap+16]. Heiden et al. pointed out that the corrosion rates in the electrochemical test are overestimated because the degradation propagated significantly slower in immersion test. Capek et al. even reported that the degradation, in immersion test in two different corrosion media, of FeMn30 occurs much slower than of pure Fe [Hei+15b][Cap+16]. In vitro cell tests with MC3T3 osteoblast and L929 fibroblast cells showed a good or at least acceptable cytocompatibility [Cap+16][Cho+13]. In order to keep the Mn content as low as possible Drynda et al. investigated binary FeMn alloy with lower Mn concentrations (0.5, 2.7, 6.9 wt %). The results of the tensile tests showed an higher strength compared to pure Fe increasing with the Mn content due to solid solution hardening. However the ductility of the material significantly decreased. In general the mechanical properties could not keep up with those of the high Mn content alloys. In vitro immersion tests and in vivo test in the mouse model showed that the corrosion of all tested FeMn alloys propagate slower compared to pure Fe [Dry+15].

Besides, various Mn concentrations also additional alloying elements like Si, C and Pd have been studied. The elements Si and C are known to enhance the TWIP/TRIP (subsection 5.2.3) effect due to an reduction of the stacking fault energy (SFE) [Bou+11] [Bou+11] and furthermore

enhance the mechanical strength due to solid solution hardening. Besides there are solved as impurities and can act as active sites for corrosion. The idea for the addition of Pd on the other hand is to form Pd rich precipitates that contributes to the strength due to precipitation hardening on the other hand Pd is a very noble material (Tab. 3.0.3). Thus Pd-rich precipitates and the matrix form a microgalvanic cell that accelerate the overall corrosion (subsection 5.1.1). This concept was first presented by Schinhammer and Moszner et al. on a FeMn10Pd1 alloy. They proofed that the addition of 1 wt% Pd and a suitable thermal treatment lead to the formation of intermetallic coherent Pd rich precipitates. As a consequence the strength and corrosion rate were increased due to the above named mechanisms. However the reported alloy did not meet the required ductility specified in Tab. 3.0.1 [Sch+10a] [Mos+11]. Therefore, in further works Schinhammer et al. studied a FeMn21C0.7Pd1 alloy. Due to the reduced SFE achieved by the higher Mn content and C addition resulting in the TWIP effect, the investigated material showed very high strength compared the above named FeMn35 alloys and even a high ductility. It was further stated, that the Pd precipitates impede the recrystallization due to the Zener effect [CH96, 870 ff.]. This allows the optimization of the thermomechanical treatments and in turn helps to tailor the microstructure and material properties [Sch+12a]. Additionally an significantly increased corrosion rate was found for the FeMn21C0.7Pd1 incomparsion to the same alloy without Pd. The authors explained this by the formation of micro galvanic corrosion. It was also found that the size of the precipitates have no influence on the corrosion which enables an optimization of the precipitates size with respect to the mechanical properties [Sch+13b]. Studies regarding the cytocompatibility of the recently discussed alloy reveald an acceptable cytocompatibility. However, it was found that the viability and metabolic activity slightly decreased for the Pd containing alloy. The effect was attributed to the faster degradation of the Pd containing alloy and an increased Mn ion concentration in the medium [Sch+13a].
On one hand the results show the feasibility of FeMn alloys in terms of the biocompatibility. On the other hand it shows that a faster corrosion is not necessarily better in terms of the biocompatibility. Therefore, it highlights once more the importance of the enhancement of the mechanical properties and design aspects that allows a reduction of the material amount brought into the body.

Investigations on other TWIP steel (FeMn30C1 and FeMn30C1S) alloys were presented by Hufenbach et al. The austenitic alloys prepared by casting and fast solidification showed a high strength and good ductility. The highest strength was found for the S containing samples due to the formation of MnS precipitates. The strength of both tested alloys exceeded even the values for FeMn30 and SS 316 L. Electochemical corrosion measurements showed an increased corrosion rate of FeMn30C1S/FeMn30C1 relative to a FeC1 reference [Huf+17].

In corrosion studies of the same FeMn30C1 alloys in chloride containing solutions Gebert et al. showed that even though the corrosion potential is shifted to more negative values, indicating a stronger tendency to corrosion, but no significant increase was observed relative to pure Fe. Investigations of the corrosion products suggested that the passivating Fe and Mn oxides significantly increases their thickness even after one hour of immersion. Furthermore, it was presented that the dissolved Fe^{2+} and Mn^{2+} ions have the tendency to form solid $Fe(OH)_2/Fe(OH)_3$, $Mn(OH)_2$ hydroxides. Depending on the electrolyte composition also phosphate and carbonate salts were found. It was suggested that protective layers of these hydroxides and salts superimpose the active dissolution and decrease the corrosion rate. However, the authors also proofed that even though the corrosion rate was not as high as anticipated, it is still significantly higher than for SS 316 L and the material still keep its degradable nature [Geb+17]. The results showed also the importance for in vivo tests and the definition of standardized testing conditions for biodegradable materials.

Liu et al. presented investigations on a Fe30Mn6Si alloy. It was reported that the alloy has

an increased strength compared to pure Fe and FeMn30. However the values are rather small relative to other values reported for FeMn alloys. Additionally a shape recovery rate of 53.7 % was reported after an plastic elongation of 2.7 %. The effect was attributed to a shape memory effect (SME), which however is not clearly discussed. For the degradation behavior the electrochemical test brought contradicting results in comparison to the immersion test. Whereas the electrochemical test showed the highest corrosion rates for the FeMn alloys, in the immersion test the values were significantly lower than those of pure Fe.

Research on FeMn(23-30)Si5 steels were performed by Drevet et al. and showed that the corrosion rate is increasing with the Mn content. Furthermore, they reported the addition of 5 % Si accelarete the corrosion rate relative to a FeMn30 alloy. For the alloys a decrease of the Young's modulus down to 118 MPa were reported, increasing Mn content. This is close to Ti implants or bone and makes the alloy even interesting for orthopedic applications. However, the materal showed a very low yield strength far below the required values for vascular implants (Tab. 3.0.1)[Dre+18].

The implementation of Ag rich precipitates into an FeMn30 alloy was investigated by Liu et al. The compressive yield strength was found to be rather low but enhanced by the precipitates. However the Ag precipitates clearly accelerated the corrosion rate and ion release, due to micro galvanic corrosion, for both Fe and Mn. Additionally a low magnetic susceptibility was found [Liu+18].

In general it is obvious that the results of degradation test are sometimes contradicting between different studies and also between electrochemical and immersion test. An explanation for these qualitative discrepancy can be found in studies by Mouzou et al. It was found that a CO_2 rich electrolyte or in general high concentrations of HCO_3^- ions favors the formation of carbonate layers on the corroding surface. These layers were found to be mainly composed of $MnCO_3$ and hinder the degradation[Mou+16a]. These results were also supported studies regarding the influence of the different electrolyte compositions. It was proofed that higher concentrations of HCO_3^- ions caused by additions of $NaHCO_3$ (which is an important buffer salt in blood) lead to an enhanced formation of $MnCO_3$ layers. Furthermore H_2PO_4 ions also hinder the degradation due to the formation of passivating phosphate layers, whereas increased amounts of Cl^- ions promotes the corrosion reaction [Mou+16b]. Therefore, the slower corrosion rate of the immersion tests, reported in many studies can be attributed to the formation of those protection layers. Because there are no standardized test conditions, it also explains how different studies can come to contradicting results when comparing similar alloys.

Surface treatment

To enhance the material properties also various surface modification techniques have been reported. However, these approaches rather aim for the modification of the initial degradation properties or biocompatibility in the initial healing period. Because the surface treatments can also affect the mechanical properties it has to be critically assessed if the resulting anisotropic properties are suitable as implant material.

An nitrided Fe stent was investigated by Feng et al. An enhanced mechanical strength, radial strength and stiffness was found. The corrosion rate for both electrochemical in vitro and in vivo tests (pig model) showed an significantly accelerated corrosion compared to pure Fe. Even though no thrombosis or local tissue necrosis was found, a slight luminal loss resulting from intimal hyperplasia was found. The authors stated that nevertheless further improvements regarding stent design and degradation time are required [Fen+13]. Daud et al. showed that hydroxyapatite (HA) coated Fe degrades slower than uncoated but enhances the cytocompatibility [Moh+14].Fe surfaces, micro patterned with Au and Pt discs were presented by Cheng and Huang et al. It was shown that the patterning lead to an uniform accelerated initial corrosion [CHZ15] [HZ16].

The effects of surface modification of pure Fe by Ag, Ta and Zn ion implantation was explored by Huang and Wang et al. It was shown that the implanted ions reach a depth of approx. 40 – 80 nm and significantly accelerate the corrosion rate. In terms of the cytocompatibility an enhancement was observed for the Ta and Zn implanted material, whereas a slight decrease of the cell viability was detected for the material with Ag ions [HCZ16][Wan+17b][Wan+17a].

Fe-X composites
Also a number of studies explored different types of Fe-X composites. The general idea of those composites is to implement particles or phases with an different (mostly higher) corrosion potential relative to the matrix. This is leading to microgalvanic corrosion and increases the anodic dissolution of the matrix. Furthermore those dispersed particles increase the strength of the material.
Huang et al. fabricated Fe-Ag, Fe-Au and FePd composites by plasma spark sintering (PSS). The results showed an increased strength and corrosion rate. Furthermore only a slight cytotoxicity to L-929 and ECV304 cells, decreased viability of smooth muscle cells and a tolerable hemolysis rate were found [HCZ14][Hua+16].
Cheng et al. implemented W, Fe_2O_3 particles and carbon nano tubes into pure Fe by (PSS). They showed that the materials exhibit an higher strength and corrosion rate compared to pure Fe. No cytotoxicity was found for L-929 fibroblast and ECV304 cells endothelial and only mild cytotoxicity for smooth muscle cells [CZ13a] [CZ13b].
Fe composites with different types of bioceramics (hydroxyapatite (HA), tricalcium phosphate (TCP) and biphasic calcium phosphate (BCP)). A slightly decreased strength but enhanced degradation and biocompatibility was found. However, these type of rather porous materials are rather suitable for orthopaedic applications [Ulu+14][Ori+14][Rei+14].

Summarizing remarks
Several studies have proofed, by in vitro cell tests and in vivo studies in various animal models, the biological applicability of pure Fe and a number of Fe based alloys. It is obvious that degradation tests are indispensable to proof the different concepts, aiming for an increased corrosion rate. However, the comparison between the results of different studies has to be assessed very critically due to a lack of standardized test conditions. Additionally, even the best in vitro test will never be able to perfectly mimic the living system. Hence, a definitive assessment of the feasibility of a certain material regarding its degradation properties has to be made in vivo. The biggest advance compared to other biodegradable material classes are the outstanding mechanical properties that can be achieved by the various fabrication methods, post processing and alloying. Particularly, FeMn alloys convince with their great combination of strength, ductility and non ferromagnetic behavior.
This great strength increases the design flexibility and in turn allows an adjustment of the degradation time by varying the surface to volume ratio. Considering a stent strut, with a square or circular shaped cross section, of two different hypothetical materials A and B. Both materials are assumed to have a similar corrosion rate of 0.1 mm/a, which is typical for Fe. For alloy A, a cross section of 10 000 µm^2 is assumed to be sufficient to withstand the load acting on an implant. If alloy B exhibits a strength that is by a factor of two higher, the necessary cross section is reduced by a factor of two to 5000 µm^2. The surface to volume ratio is in turn increased by $\approx$ 30 %. Under the assumption that the degradation occurs homogeneously from all sides, this increased relative surface would in turn also decrease the degradation time by $\approx$ 30 %. Furthermore a lower strut cross section reduces the amount of foreign material that has to be brought into the body. These properties of Fe based materials offer a great potential for biodegradable vascular implants.

Table 3.0.4: Literature values of the mechanical properties for Fe-based biodegradable materials

Comp.	Method annealing (°C)	YS (MPa)	UTS (MPa)	A (%)	Ref.
pure-Fe	E-Fe,adp.[a]	360	423	8.3	[Mor+10a]
pure-Fe	E-FeM,[a] 550	270	292	18.4	
pure-Fe	E-Fe, 600 °C	130	169	32.3	
pure-Fe	Cast-Fe, 550	140	205	25.5	
pure-Fe	As recieved	170	270	49.3	[Oba+15]
pure-Fe	UDR[a]75 %	593	600	3.5	
pure-Fe	BDR[a]75 %	507	517	4.0	
pure-Fe	UDR,[a] 550	246	283	34.8	
pure-Fe	BDR,[a] 550	229	274	40.2	
pure-Fe	UDR,[a] 900	108	248	48.3	
pure-Fe	BDR,[a] 900	97	232	51.7	
pure-Fe	UDR[a]85 %550	236	287	46.1	[Oba+16]
pure-Fe	UDR[a]75 %800	104	238	47.0	
pure-Fe	UDR[a]85 %1000	93	173	17.2	
pure-Fe	ECAP 0x[a]	—	262	—	[Nie+10]
pure-Fe	ECAP 2x[a]	—	313	—	
pure-Fe	ECAP 4x[a]	—	381	—	
pure-Fe	ECAP 8x[a]	—	470	—	
pure-Fe	Fe	150	210	—	[Che+13]
FeMn20	sintering	421	702	7.5	[HDM08]
FeMn25	sintering	361	723	4.8	
FeMn30	sintering	239	518	19.0	
FeMn35	sintering	234	428	32.0	
FeC [1]	cast, forged	—	160	—	[VKČ15]
FeF [1]	cast, forged	—	310	—	
FeMn30C [1]	cast, forged	—	210	—	
FeMn30F [1]	cast, forged	—	530	—	
pure-Fe	as recieved	250	300	37.5	[Sch+10a]
pure-Fe	cast,1100	700	900	9.5	
FeMn10	cast,1100	—	—	—	
FeMn10	cast,500	800	1400	14.0	
FeMn10	cast,700	650	1300	14.0	
FeMn10Pd1	cast,1100	950	1500	2.0	
FeMn10Pd1	cast,500	900	1550	7.0	
FeMn10Pd1	cast,700	850	1450	11.0	
pure-Fe	as recieved	230	300	37	[Sch+12a]
FeMn21C0.7	cast,1150	345	980	62	
FeMn21C0.7Pd1	cast,1150	360	970	64	
FeMn21C0.7Pd1	cast,1150, cw12% [a]	690	1120	38	
FeMn21C0.7Pd1	cast,1150 cw23 % [a]	1095	1320	29	
FeMn21C0.7Pd1	cast,1150,cw12%, 700 [a]	505	1020	53	
FeMn21C0.7Pd	cast,1150,cw 23 %, 700 [a]	725	1255	38	
pure-Fe [1]	As-Cast	216	225	11	[LZ11]
pure-Fe [1]	Rolled	370	440	5.2	
FeMn3 [1]	As-Cast	228	345	21	
FeMn3 [1]	Rolled	410	670	5	

Alloy	Method annealing	YS (MPa)	UTS (MPa)	A (%)	Ref.
FeCo3 [1]	As-Cast	108	220	26	
FeCo3 [1]	Rolled	450	640	5.2	
FeAl3 [1]	As-Cast	145	193	12	
FeAl3 [1]	Rolled	395	525	5.5	
FeW3 [1]	As-Cast	170	264	23	
FeW3 [1]	rolled	455	694	6.2	
FeB3 [1]	As-Cast	144	366	14	
FeB3 [1]	Rolled	453	765	12	
FeSn [1]	As-Cast	6	6	0.5	
Fec3 [1]	Rolled	430	625	7.4	
FeS0.5 [1]	Rolled	431	855	8.4	
FeMn30	Injec. mold.	106	115	0.7	[Cho+13]
Pure Fe	Hot forged	299	372	57	[Cap+16]
FeMn30	Hot forged	242	632	94	
FeMn35	sintered	235	550	31	[Her+08]
FeMn35	sintered	—	50.7	1.1	[ZC15]
pure-Fe [c,1]	cast	150	610	—	[CZ13a]
FeW2 [c,1]	PSS[a]	180	810	—	
FeW5[c,1]	PSS [a]	250	980	—	
Fe-(CNT)1[a,c,1]	PSS [a]	230	1260	—	
Fe-(CNT)0.5[a,c,1]	PSS[a]	290	1200	—	
pure-Fe [c,1]	PSS [a]	150	605	—	[CZ13b]
Fe-(Fe_2O_3)2 [c,1]	PSS [a]	165	1080	—	
Fe-(Fe_2O_3)5 [c,1]	PSS[a]	310	1040	—	
Fe-(Fe_2O_3)10 [c,1]	PSS[a]	225	1000	—	
Fe-(Fe_2O_3)50 [c,1]	PSS [a]	20	20	—	
pure iron[c,1]	PSS [a]	140	805	—	[Hua+16]
Fe–2Ag [c,1]	PSS [a]	220	1220	—	
Fe–5Ag [c,1]	PSS [a]	390	1620	—	
Fe–10Ag [c,1]	PSS [a]	205	1140	—	
Fe–2Au [c,1]	PSS [a]	350	1390	—	
Fe–5Au [c,1]	PSS [a]	240	1310	—	
Fe–10Au[c,1]	PSS [a]	350	1420	—	
pure Fe [c]	PSS [a]	148	—	—	[HCZ14]
Fe–Pd35 [c]	PSS [a]	445	754	—	
Fe–Pt35 [c]	PSS [a]	503	785	—	
pure-Fe	sintered	354	752	—	[Ulu+14]
Fe-(HA)5[a,c,1]	sintered	325	717	—	
Fe-(BCP)5[a,c,1]	sintered	312	708	—	
Fe-(TCP)5[a,c,1]	sintered	312	696	—	
pure-Fe	Stent	236	342	—	[Fen+13]
Nitrided Fe	Stent	561	614	—	
Fe [c]	arc melt.	320	—	50	[Liu+18]
FeMn30Ag[c]	arc melt.	94	—	42	
FeMn29Ag1[c]	arc melt.	130	—	38	
FeMn23Si5	arc melt.	198	—	—	[Dre+18]
FeMn26Si5	arc melt.	211	—	—	
FeMn30Si5	arc melt.	171	—	—	

Alloy	Method annealing	YS (MPa)	UTS (MPa)	A (%)	Ref.
FeMn30C1	cast	323	689	26	[Huf+17]
FeMn30C1S	cast	343	772	30	
Fe [c]	cast	73	—	—	[Čap+17]
FePd2 [c]	cast	279	—	—	
Fe [c]	PSS [a]	765	—	—	
FePd2 [c]	PSS [a]	845	—	—	
Fe [c]	porous	10	12	—	
FePd2 [c]	porous	14	20	—	
Pure Fe [c]	PSS	148	—	—	[HCZ14]
FePd0.3 [c]	PSS	445	754	—	
FePd2 [c]	PSS	503	785	—	
pure-Fe	cast	207	313	37.6	[Dry+15]
FeMn0.5	cast	295	353	28.1	
FeMn2.7	cast	370	495	31.3	
FeMn6.9	cast	814	1041	11.5	

[a] Abreviations: E-Fe = Electroformed; adp = as deposited;; UD = uni-directional; BD = bi-directional; ECAP= equal channel angular pressing; CNT = carbon nano-tube; LSM = Large strain machining; PSS = Plasma spark sintering; HA = hydroxyapatite; TCP = tricalcium phosphate; BCP = biphasic calcium phosphate; PCL = poly(ε-caprolactone); MEVVA = metal vapor vacuum arc ion source

[1] Approximate value from diagram.

[c] compression test

Table 3.0.5: Literature values of the corrosion properties for Fe-based biodegradable materials: corrosion rates CR, weight loss WL and measurement conditions (determined from electrochemical and weight loss measurements

Comp.	Method, annealing (°C)	CR (mg/cm^{2}d) * (mm/a) **	WL (mg/cm^{2}d)* (mm/a)**	Condition Sol,Temp,pH –,(°C),–	Ref.
pure-Fe	E-Fe,adp.[a]	0.85 **	0.400**	HBSS [1], 37, 7.4	[Mor+10a]
pure-Fe	E-FeM[a], 550	0.51**	0.250**		
pure-Fe	Cast-Fe, 550	0.16 **	0.140 **		
pure-Fe	E-FeM[a], adp.	0.40 **	—	HBSS[1], 37, 7.4	[Mor+10b]
pure-Fe	E-FeM[a], 550	0.25 *	—		[Mor+10b]
pure-Fe	Cast-Fe, 550	0.14 *	—		[Mor+10b]
pure-Fe	UDR[a], 550	0.242 **	0.144 **	HBSS [1],	[Oba+15]
pure-Fe	BDR[a], 550	0.243 **	0.136 **	37, 7.4	
pure-Fe	UDR[a], 900	0.223 **	0.126 **		
pure-Fe	BDR[a], 900	0.209 **	0.125 **		
pure-Fe	UDR[a]85 %550	0.172 **	0.120 **	HBSS[1],	[Oba+16]
pure-Fe	UDR[a]75 %800	0.215 **	0.127 **	37, 7.4	
pure-Fe	UDR[a]85 %1000	0.244 **	0.146 **		
pure-Fe	MC[a]Fe	0.127 **	0.274 *	PS $^1O_2$ rich	[NZ12]
pure-Fe	ECAP NC-Fe[a]	0.100 **	0.215 *	PS $^1O_2$ rich	
pure-Fe	MC-Fe[a]	0.117 **	0.253 *	PS $^1O_2$	
pure-Fe	ECAP NC-Fe[a]	0.095 **	0.205 *	PS $^1O_2$	
pure-Fe	MC-Fe[a]	0.039 **	0.019 *	PS $^1O_2$ free	
pure-Fe	Fe	—	0.489 *	SBF 37, 7.4	[Zhu+09]
pure-Fe	Fe	0.105 **	—	HBSS,37	[Che+13]
FeMn20	sintering	1.3 **	—	HBSS [1],	[HDM08]
FeMn25	sintering	1.1 **	—	37, 7.4	
FeMn30	sintering	0.7 **	—		
FeMn35	sintering	0.7 **	—		
pure-Fe	As-Cast	0.105 **	0.403 *	HBSS, 37, 7.4	[LZ11]
pure-Fe	Rolled	0.103 **	0.313 *		
FeMn3	As-Cast	0.105 **	0.095 *		
FeMn3	Rolled	0.087 **	0.067 *		
FeCo3	As-Cast	0.128 **	0.136 *		
FeCo3	Rolled	0.142 **	0.195 *		
FeAl3	As-Cast	0.112 **	0.154 *		
FeAl3	Rolled	0.111 **	0.105 *		
FeW3	As-Cast	0.151 **	0.112 *		
FeW3	rolled	0.148 **	0.082 *		
FeB3	As-Cast	0.175 **	0.103 *		
FeB3	Rolled	0.121 **	0.111 *		
Fec3	Rolled	0.187 **	0.345 *		
FeS0.5	Rolled	0.145 **	0.253 *		
FeMn30	Injec. mold.	0.730 **	—	HBSS [2], 37, 7.4	[Cho+13]
Pure-Fe	Cast	0.050 **	—	Osteogenic media	[Hei+15b]
FeMn33	Cast	0.348 **	—		
FeMn33	LSM[a]	0.835	—		
Pure Fe	Hot forged	0.041 **	0.082 **	SBF	[Cap+16]

Comp.	Method, annealing (°C)	CR mg/cm^{2}d * (mm/a)**	WL mg/cm^{2}d* mm/a**	Condition Sol,Temp,pH –,(°C),–	Ref.
FeMn30	Hot forged	0.899 **	0.019 **	SBF	
Pure Fe	Hot forged	—	0.060 **	DMEM	
FeMn30	Hot forged	—	0.035 **	DMEM	
FeMn35	sintered	0.440 **	—	HBSS [1], 37, 7.4	[Her+08]
FeMn35	sintered	2.340 **	—	5 % NaCl	[ZC15]
FeMn35	sintered	1.990 **	—	SBF	
FeMn20	casting	0.943 **	—	Osteogenic media	[Hei+15a]
FeMn20	cold rolling	0.539 **	—	SBF [3], 37, 7.4	
FeMn35	sintered	0.510 **	—		[Sin+15]
FeMn21C0.7Pd1	cw[a], 900	—	0.21 **	SBF [4]37, 7.4	[Sch+13b]
pure-Fe	cast	0.008 **	0.052 *	HBSS [5], 37, 7.4	[CZ13a]
FeW2	PSS[a]	0.075 **	0.056 *		
FeW5	PSS [a]	0.138 **	0.066 *		
Fe-(CNT)1[a]	PSS [a]	0.099 **	0.102 *		
Fe-(CNT)0.5[a]	PSS[a]	0.017 **	0.084 *		
Fe-(Fe_2O_3)2	PSS [a]	0.083 *	0.059 *	HBSS [5],37, 7.4	[CZ13b]
Fe-(Fe_2O_3)5	PSS[a]	0.113 **	0.066 *		
Fe-(Fe_2O_3)10	PSS [a]	0.005 **	0.027 *		
Fe-(Fe_2O_3)50	PSS [a]	0.027 **	0.028 *		
pure iron	PSS [a]	0.043**	0.14 *	HBSS [5],37, 7.4	[Hua+16]
Fe–2Ag	PSS [a]	0.119**	0.17 *	HBSS [5],37, 7.4	
Fe–5Ag	PSS [a]	0.140**	0.21 *	HBSS [5],37, 7.4	
Fe–10Ag	PSS [a]	0.174**	0.19 *	HBSS [5],37, 7.4	
Fe–2Au	PSS [a]	0.173**	0.17 *	HBSS [5],37, 7.4	
Fe–5Au	PSS [a]	0.130**	0.23 *	HBSS [5],37, 7.4	
Fe–10Au	PSS [a]	0.098**	0.17 *	HBSS [5],37, 7.4	
pure Fe	PSS [a]	—	0.06 *	HBSS [5],37, 7.4	[HCZ14]
Fe–Pd35	PSS [a]	—	0.13 *	HBSS [5],37, 7.4	
Fe–Pt35	PSS [a]	—	0.18 *	HBSS [5],37, 7.4	
Pure Fe	foam	—	0.001 *	HBSS, 37, 7.4	[Ori+14]
Fe-(CNT)[a]	foam	—	0.0009 *		
Fe-Mg	foam	—	0.002 *		
Pure Fe	sintered	0.021 *	0.038 *	SBF,37	[Ulu+14]
Fe-(HA)5[a]	sintered	0.199 *	0.031 *		
Fe-(BCP)5[a]	sintered	0.192 *	0.026 *		
Fe-(TCP)5[a1]	sintered	0.181 *	0.024 *		
Pure Fe	sintered	—	0.153 **	0.9 % NaCl,37	[Rei+14]
Fe-(TCP)40[a]	sintered	—	0.196 **		
Pure Fe	coating	0.031 **	—	MEM [3]37	[Moh+14]
Fe-(HA/PCL)[a]	coating	0.002 **	—		
Fe-(HA)[1]	coating	0.003 **	—		
Pure Fe	Stent	0.127 **	—	PBS [a]37, 7.4	[Fen+13]
Nitrided Fe	Stent	0.225 **	—		
pure-Fe		0.027 *	0.048 *	HBSS, 37, 7.4	[HCZ16]
Fe Ag implanted	MEVVA[1]	0.046 *	0.055 *		
Pure Fe	uncoated	0.025 **	0.091*	HBSS [5], 37, 7.4	[CHZ15]
Fe-Au 50µm^2	patterned	0.147**	0.113 *		

Comp.	Method, annealing (°C)	CR mg/cm^{2}d * (mm/a)**	WL mg/cm^{2}d* mm/a**	Condition Sol,Temp,pH –,(°C),–	Ref.
Fe-Au 200µm^2	discs	0.108 **	0.118 *		
Fe-Au full		0.124 **	0.141 *		
Pure Fe	uncoated	0.112 **	0.148 *	HBSS [5], 37, 7.4	[HZ16]
Fe-Au 16µm^2	patterned	0.222 **	0.383 *		
Fe-Au 100µm^2	discs	0.205 **	0.345 *		
Fe	arc melt.	0.007 **	—	HBSS, 37	[Liu+18]
FeMn30Ag	arc melt.	0.007 **	—		
FeMn29Ag1	arc melt.	0.012 **	—		
Fe	arc melt.	0.12 **	0.10 **	HBSS [6], 37, 7.4	[Dre+18]
FeMn30	arc melt.	0.26 **	0.24 **		
FeMn23Si5	arc melt.	0.48 **	0.44 **		
FeMn26Si5	arc melt.	0.59 **	0.56 **		
FeMn30Si5	arc melt.	0.80 **	0.76 **		
Fe	arc melt.	0.13 **	—	SBF,37	[Wan+17c]
FeGa19	arc melt.	0.48 **	—		
FeGa19B2	arc melt.	0.63 **	—		
FeGa19-(TaC)0.5	arc melt.	0.33 **	—		
FeC1	cast	≈0.012 **	—	SBF [1],37	[Huf+17]
FeMn30C1	cast	0.022 **	—		
FeMn30C1S	cast	0.024 **	—		
Fe	cast	0.052 **	—	SBF [7],37, 7.4	[Čap+17]
FePd2	cast	0.025 **	—		
Fe	PSS	0.040 **	—		
FePd2	PSS	0.115 **	—		
Fe	porous	0.658 **	—		
FePd2	porous	1.162 **	—		

[a] Abreviations: E-Fe = Electroformed; adp = as deposited; HBSS Hanks buffered salt solution; UD = unidirectional; BD = bi-directional; ECAP= equal channel angular pressing; PS= physical saline; SBF = simulated body fluid; CNT = carbon nano-tube; LSM = Large strain machining; PSS = Plasma spark sintering;cw = cold worked; HA = hydroxyapatite; TCP = tricalcium phosphate; BCP = biphasic calcium phosphate; PCL = poly(ε-caprolactone); MEM = minimum essential medium solution; MEVVA = metal vapor vacuum arc ion source

[1] Modified with Sodium bicarbonate, Hepes sodium salt and Hepes acid

[2] Modified with Sodium bicarbonate

[3] Modified with Hepes buffer

[4] Modified and CO_2 inlet

[5] Modified with ethylene diamine tetra-acetic acid (EDTA)[CL02]

[6] Modified Sodium bicarbonate and calcium chloride

[7] Modified with Tris-HCl and NaN_3

4 Goal of the work

The main research goals formulated by Peuster et al. [Peu+01] [Peu+06] are the enhancement of the mechanical properties and an acceleration of the degradation time.Therefore, besides studying suitable alloys and material compositions, also alternative fabrication methods and processing routes have to be investigated.

The aim of the this work was to explore magnetron sputtering as an alternative fabrication method for biodegradable, Fe-based devices. The technique is majorly known from microsystems technology and in combination with UV-lithography used for the fabrication of integrated circuits (IC) and microelectronic mechanical systems (MEMS). Zamponi et al. proofed that the method is feasible for the fabrication of freestanding, structured, stent-like NiTi devices [Zam+08][LZQ09] [LZQ13] [Sie+14]. For the fabrication of biodegradable Mg devices the method was adopted by Schlüter and Haffner et al. [Sch+10b][Sch+12b] [Sch+14] [Haf+15].
The advantage of the method is its versatility. First of all it is suitable for the deposition of all kinds of alloys by using alloyed sputter targets. Additionally, even the deposition of non compound forming systems is possible by co-sputtering or multilayer deposition followed by a homogenization. This allows the implementation of noble precipitates that accelerate the corrosion rate (subsection 5.1.1) and increase the strength. Another feature is the high purity of the deposited films. Since the deposition occurs out of the thermodynamic equilibrium state, it is also possible to stabilize meta stable phases and achieve small grain sizes compared to other methods (see subsection 5.3.2). Due to this unique microstructure, sputtered films are expected to exhibit a higher strength compared to materials with identical composition fabricated by other methods.
In addition the deposition on structured substrates transfers the geometrical shape of the devices during the deposition. Thus no post processing like drilling or cutting is necessary, which would influences the microstructure and material properties.
Also the small feature sizes which are a key feature of UV-lithography enable a large degree in freedom in design. Haffner et al. showed that it is possible to fabricate Mg devices with lateral feature sizes of 5 µm and a film thickness of 250 µm [Haf+15].
The versatility of fabrication method offers a great potential to challenge the research goal formulated by Peuster et al. [Peu+01], by applying or combining different approaches in order to accelerate the CR and enhance the mechanical strength.

The work presents the fabrication of this in situ structured, freestanding foils of pure Fe, binary FeMn alloys with different stoichiometries and the non compound forming Fe-Au system by magnetron sputter deposition. The selection of the compositions was done in order to achieve:

- A strength as high as possible but at least $\geq 300\,\mathrm{MPa}$
- High ductility at least $\geq 15\,\%$
- Higher corrosion rate compared to pure Fe
- Non ferromagnetic behavior
- Mn content low as possible but as high as necessary

The relevant material properties (microstructure, in vitro corrosion behavior, mechanical and magnetic properties) are evaluated by the respective methods. The experimental parts, results

and discussions are presented in the form of five published articles (chapter 6). Some aspects regarding the fabrication process and some less familiar concepts, that are not detailed discussed in the articles are briefly introduced in the next chapter 5.

5 Fundamentals

5.1 Corrosion

5.1.1 The different types of corrosion

It can be distinguished between several different corrosion types displayed in Fig. 5.1.1. The corrosion mechanisms relevant for this work are briefly introduced in the following. For the other corrosion types it is referred to the cited literature [Dav00, 5 ff.] [Jon96, 9 ff.].

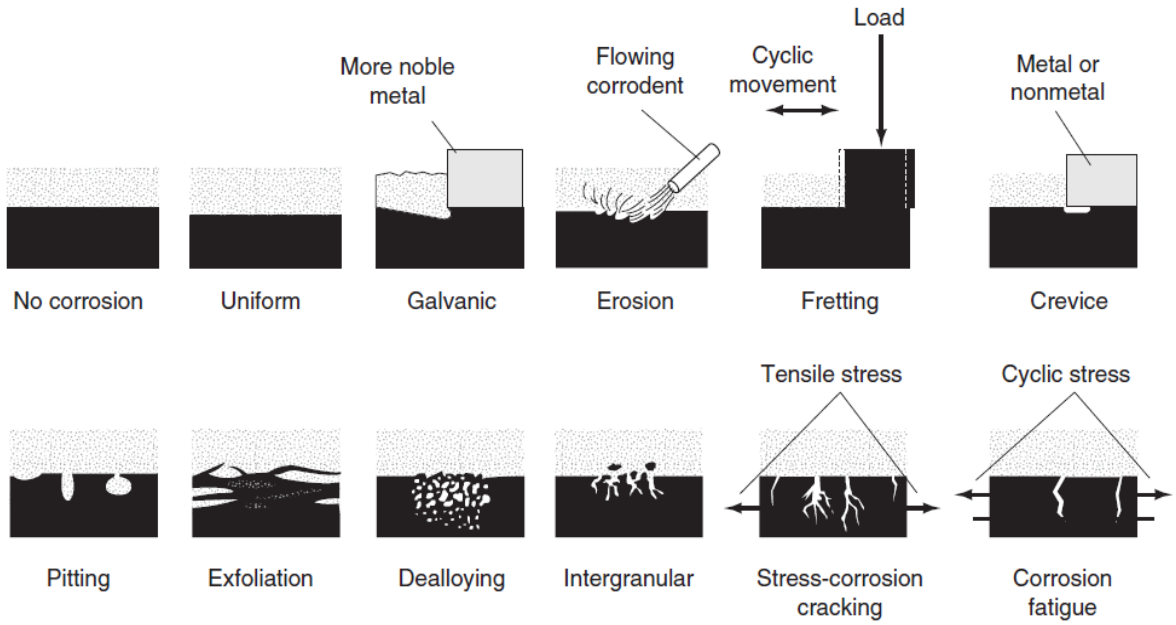

Figure 5.1.1: The different types of corrosion (with permission of ASM International [Dav00, p. 5]).

Uniform corrosion
This type is the most common and often desired form of corrosion because of its predictability. The metal surface atoms interact with ions of an electrolyte. The surface acts at the same time as anode and as cathode. The generalized reaction equation is:

$$\mathrm{M} + \mathrm{nOx}^{+} \rightarrow \mathrm{M}^{\mathrm{n}+} + \mathrm{Red} \tag{5.1.1}$$

This means a metal atom (M) on the surface transfers n electrons to an oxidized species in the electrolyte (Ox) in the electrolyte. The species is than reduced (Red) and the metal atom goes into solution as positively charged metal ion ($\mathrm{M}^{\mathrm{n}+}$). The spot were the anodic and cathodic reaction takes place changes all the time and leads to an homogeneous material removal. The anodic reaction is in general the metal dissolution [Jon96, p. 42]:

$$\mathrm{M} \rightarrow \mathrm{M}^{\mathrm{n}+} + \mathrm{ne}^{-} \tag{5.1.2}$$

Typical anodic reactions are the cathodic hydrogen evolution,

$$2H^+ + 2e^- \rightarrow H_2 \tag{5.1.3}$$

in neutral and alkaline solutions the water decomposition [Jon96, p. 50]

$$2H_2O + 2e^- \rightarrow H_2 + 2OH^- \tag{5.1.4}$$

and oxygen reduction.

$$O_2 + 4H^+ + 4e^- \rightarrow 2H_2O \tag{5.1.5}$$

The specific reaction for Fe based alloys in pseudo physical solutions are discussed below in (subsection 5.1.2

Galvanic corrosion
The intentional generation of galvanic corrosion is one of the strategies to accelerate the corrosion rate of biodegradable Fe based material. It occurs always if two different noble metals or phases stand in direct and conductive contact. The difference in the corrosion potentials U_0 leads to a spatial separation of the anodic and cathodic reaction. While the cathodic reaction happens at the more noble regions, the anodic metal dissolution occurs at the less noble spots. Thus, there is an preferred dissolution of the less noble phase displayed in Fig. 5.1.2. The reason is that the two metals or phases polarize each other when they are in direct contact. Electrons flow from the less noble to the noble metal or phase. Therefore, the anodic metal dissolution occurs preferred at the less noble phase and the cathodic reaction at the more noble phase. Due to the enhanced ability of the noble phase for cathodic reductions also the cathodic half-cell reaction current increases. In turn also the anodic current increases as required by the mixed potential theory [Jon96, 86 ff.] (the sum of the anodic and cathodic half cell currents have to be zero in the equilibrium). As a consequence the mixed corrosion potential of the galvanic couple (U_{gc}) and corrosion current (I_{gc}) are shifted to higher values. This relationship is shown for two different galvanic couples (gc) in Fig. 5.1.3. In the diagram the potential difference of gc1 is lower than for gc2. The qualitative behavior would be the same if instead of an increased potential difference, the area of the cathode material is increased. Because the anodic metal dissolution is direct proportional to the corrosion current density the following general predictions can be done for galvanic corrosion. If the anode area is kept constant or deceases the anodic metal dissolution and corrosion rate is as higher as:

- Higher the potential difference of the corrosion potential between the coupled metals or phases.
- Larger the surface area of the cathodic material [Jon96, 168 ff.].

Pitting corrosion
This type of localized corrosion is common for passivating metals especially in Cl^--rich electrolytes. Thus, it is also relevant for Fe based alloys in pseudo-physiological solutions.
The mechanism is explained for pure Fe in the following. The first step is the initiation step. The hydrated FeO passive film (FeOOH) reacts with Cl ions.

$$FeOOH + Cl^- \rightarrow FeOCl + OH^- \tag{5.1.6}$$

This leads to an FeOCl salt percipitation on the surface. These salts catalyze the release of Fe^{3+} ions by dissolution of the FeOOH passive film.

$$FeOCl + H_2O \rightarrow Fe^{3+} + Cl^- + 2OH^- \tag{5.1.7}$$

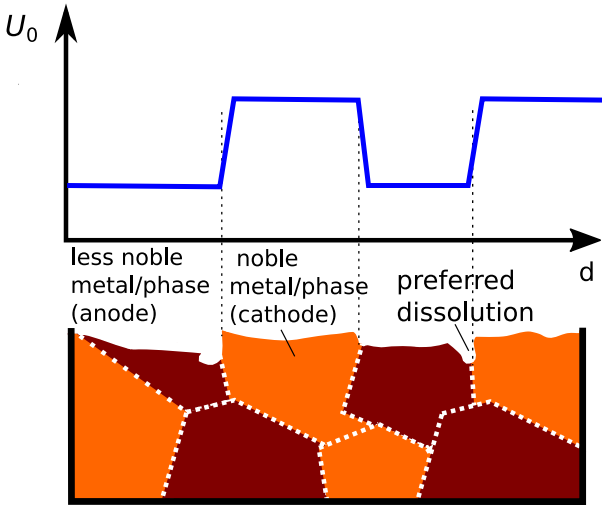

Figure 5.1.2: Schematic depiction of the preferred anodic metal dissolution depending on U_0 at different positions d on a multiphase metal surface.

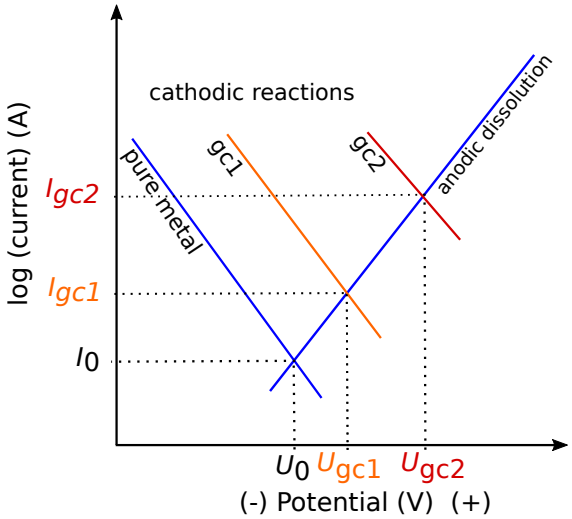

Figure 5.1.3: Schematic I(U) curves for a metal and different galvanic couples (gc) with more nobel metals or phases (according to [Jon96, p. 175]).

Once the passive film is weak enough or a pit is formed a local anodic Fe dissolution follows. This happens preferred at defects and lead to an localized accelerated corrosion. Because the released Fe^{3+} ions tend to the formation of porous $Fe(OH)_3$ caps over a generated pit. This results in the second step of pitting corrosion, the propagation. A schematic depiction of this is given in Fig. 5.1.4. The porous $Fe(OH)_3$ cap impedes the migration of O_2 and Fe^{2+} but is permeable to Cl^- ions. These conditions lead to hydrolysis and in turn an acidification of the electrolyte within the pit.

$$Fe^{2+} + H_2O + 2Cl^- \rightarrow Fe(OH)_2 + 2Cl^- + 2HCl \tag{5.1.8}$$

The result is an autocatalytic acceleration of the local degradation rate. If the galvanic corrosion occurs randomly and uniformly distributed over the entire surface also the overall degradation rate is increased [Jon96, 199 ff.]

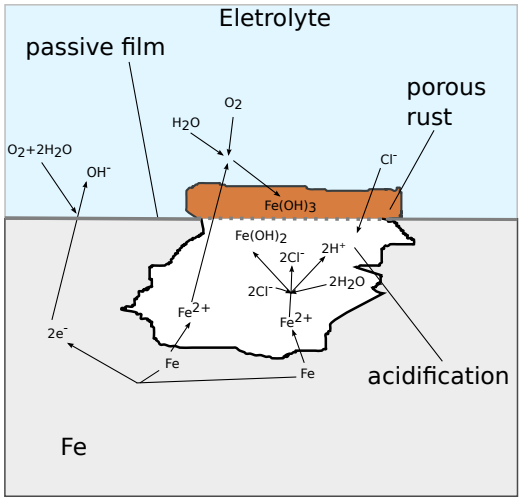

Figure 5.1.4: Schematic depiction of the propagation of pitting corrosion (according to [Jon96, p. 214]).

5.1.2 Corrosion of Fe and FeMn in pseudo physiological solution

Pseudo physiological solutions are used for different purposes. In terms of biodegradable candidate materials there are usually used for in vitro corrosion and cell tests. This allows the assessment how a material could behave in vivo. The ionic composition and pH value should therefore be close to real body fluids like blood. Usually the pH value is approx 7.4 whereas there are different ionic composition for the different solutions, as presented in Tab. 5.1.1.
Even though these differences are significant, it is obvious that they are main component is dissolved NaCl salt. Thus, in general the corrosion mechanisms are similar to the corrosion of Fe based material in neutral to slightly alkaline solutions such as seawater. In this sub section the typical reactions of Fe and FeMn alloy are discussed.
In aerated solutions the dissolution of Fe is independent of the pH value within a large range (aprox. 6–9) because the reaction rate is determined by the pH independent cathodic oxygen reduction (Eq. 5.1.5) [Tos05].
The anodic dissolution of both Fe and Mn follows the relation

$$Fe \rightarrow Fe^{2+} + 2e^- \tag{5.1.9}$$

$$Mn \rightarrow Mn^{2+} + 2e^- \tag{5.1.10}$$

Table 5.1.1: Ionic compositions ($mg\,L^{-1}$) of different pseudo physiological solutions [Mou+16b] [Cap+16]

Ions	Hanks' solution modified	Phosphate buffered salt solution	Simulated body fluid (SBF)	Human blood plasma
Cl^-	3542	4947	3858	3360–3390
Na^+	2795	3519	3251	3000–3400
Ca^{2+}	35	—	100	84–110
Mg^{2+}	14	—	24.3	15–30
HCO_3^-	1654	—	1647	1100–2400
$HPO_4^{2-}/H_2PO_4^-$	48	920	—	270–450
SO_4^{2-}	78	—	96	5–15
K^+	172	162	195	130–210
D − Glucose	714	—	—	600–1200
Albumin	—	1000	—	2800–5600

Whereas the Mn^{2+} ion solubility is quite high the Fe^{2+} ions tend to the further reaction to hydrated FeO ($Fe(OH)_2$).

$$Fe + 2OH^- \rightarrow FeO \cdot H_2O \tag{5.1.11}$$

$$Fe^{2+} + 2OH^- \rightarrow Fe(OH)_2 \tag{5.1.12}$$

Because $Fe(OH)_2$ is not stable it is further oxidized to Fe(III)hydroxide which is also the reason for the strong tendency of pitting corrosion [CZ13a].

$$4Fe(OH)_2 + O_2 + 2H_2O \rightarrow 4Fe(OH)_3 \tag{5.1.13}$$

5.2 Mechanical properties

5.2.1 Hardening

In order to tailor the mechanical properties of metallic materials there are several different possibilities discussed in the following. At first it has to be understood how plastic deformation works in a metal. Usually plastic deformation occurs by the slip of atomic planes, not randomly but on specific crystallographic planes in a certain direction, the slip systems. Those slip systems thus depends on the crystal structure and happens on the closed packed planes. The critical shear-stress τ, that is necessary to initiate the slip, depends according to Eq. 5.2.1 on the applied stress σ, the angles between load direction and the slip plane λ and between load direction and slip direction χ [HW06, p. 120]:

$$\tau = \sigma \cos(\lambda) \sin(\chi_0) \tag{5.2.1}$$

Therefore, a higher symmetry supports plastic deformation because a higher amount of slip systems increases the probability that a slip system is activated. This explains why a fcc metal with twelve slip systems is usually more ductile than hcp metal with only six slip systems. It becomes also clear that the orientation and the texture in poly crystals can play a role. Besides the glide of dislocations there is also the possibility for the formation of deformation twins. This requires conditions were the dislocation glide is blocked or the twin formation is energetically

favorable (see subsection 5.2.3)[Got07, 227 ff.] [HW06, 119 ff.].
In order to tailor the strength and ductility of a metal several different mechanisms and treatments are utilized. All of them hinders the movement of dislocations by different mechanisms, discussed in the following.

Grain refinement
Since a grain boundary is an insurmountable obstacle, an dislocation pile up occurs at the grain boundaries. These dislocations hinder each other and increase the stress in a grain. In turn also the shear stress necessary for further deformation is increased $\Delta\tau$ and proportional to the shear modulus G, burgers vector b and the square root of the dislocation density $\sqrt{N}$ [HW06, p. 142].

$$\Delta\tau \propto G \cdot b \cdot \sqrt{N} \tag{5.2.2}$$

Because small grains promote a high dislocation density also the yield stress $\Delta\sigma$ is enheanced if the grain size d decreases. This relation ship is expressed in the well known Hall-Petch relation (Eq. 5.2.3) and proofed for many metallic material [HW06, 142 ff.] [Hal51b] [Hal51a].

$$\Delta\sigma = \sigma_0 + \frac{k_y}{\sqrt{d}} \tag{5.2.3}$$

Were k_y is an material dependent proportionality constant and σ_0 the yield stress for the deformation of a single crystal.

Solid solution hardening
An important hardening mechanism is the solid solution hardening. Here, specific impurity atoms are brought into the material. These impurities are incorporated in the matrix as either interstitial or substitutional atoms in the lattice. These atoms disturb the lattice and lead to interactions with dislocations and hinder their movement. It is distinguished between paraelastic and diaelastic interactions.

Paraelastic interaction
The local volume change in the lattice generated by incorporated atoms, leads to elastic distortions. These induced stress interferes with the dislocation movement. The strength of this paraelastic interaction force F_P (Eq. 5.2.4) depends on the change in the lattice parameter a (in a cubic lattice) and the concentration of impurity atoms c_B expressed by the dimension less δ (Eq. 5.2.5)[Got07, 267 ff.].

$$F_P \approx Gb^2 \mid \delta \mid \tag{5.2.4}$$

$$F_P \propto \delta = \frac{\mathrm{dln}(a)}{\mathrm{d}c_B} \tag{5.2.5}$$

Diaelastic interaction
Similar to the influence of the lattice extension also the change of the shear modulus G causes a force F_D (Eq. 5.2.7), hindering the dislocation movement. This force depends on the atomic concentration change of the impurity atoms c_B and is expressed by the dimension less η (Eq. 5.2.6) [Got07, 267 ff.].

$$F_D \approx \frac{1}{20} Gb^2 \mid \eta \mid \tag{5.2.6}$$

$$F_D \propto \eta = \frac{\mathrm{dln}(G)}{dc_B} \tag{5.2.7}$$

The total interaction force F_{max} is sum of the diaelastic and paraelastic component.

$$F_{max} = F_P + F_D \tag{5.2.8}$$

The repulsive force acting on moving dislocation increases the critical shear stress τ depending on the b and the mean free dislocation length also known as Friedel length l_F[Got07, p. 268].

$$\Delta\tau = \frac{F_{max}}{bl_F} \tag{5.2.9}$$

with

$$l_F = \sqrt[3]{\frac{6E_d}{\Delta\tau c_F b}} \tag{5.2.10}$$

Were E_d is the dislocation energy (Eq. 5.2.21) and c_F the particle density $c_F = f/r^2$.

Precipitation/dispersion hardening
This type of hardening occurs if the matrix contains solid dispersed non metallic particles for example oxides or carbides. Or if a second phase is precipitated in an alloy due to a suitable heat treatment. Usually this particles or precipitates are randomly and uniformly distributed within the matrix. It is obvious that they will hinder the movement of a passing dislocation. It is distinguished between coherent, partially coherent and incoherent precipitates. In case of incoherent precipitates and also dispersed particles, the only option for a dislocation to pass the obstacle is to run around. This is described by the Orowan mechanism schematically shown in Fig. 5.2.1. To pass the obstacles the dislocation have to bow around them. At some point the anti parallel parts join up and form a dislocation ring. This bowing of the dislocation requires energy and hence hinders the dislocation movement. Additionally the dislocation ring left behind generates an stress field and further increases the critical shear stress τ for the movement of following dislocations.

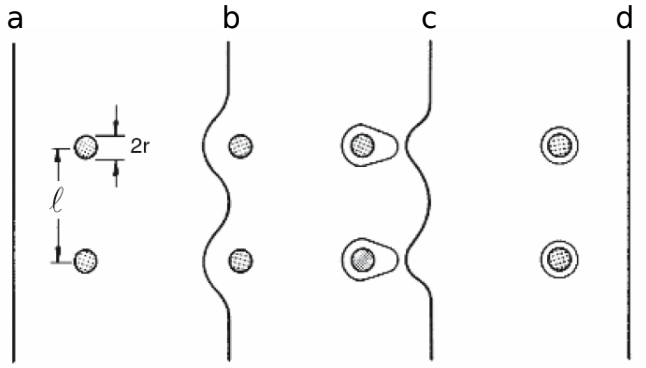

Figure 5.2.1: Schematic sketch of the Orowan mechanism in different states. a) moving dislocation arrives two obstacles; b) dislocation start to bow around the obstacles; c) when the anti parallel parts of the bowed dislocation join up they form a dislocation ring around the obstacles; d) dislocation after passing the obstacles. Here, l is the distance between two obstacles and r the radius of the particles (with permission of Springer Science and Bus Media B V [Got07, 272 ff.]).

The critical stress, necessary for the dislocation to overcome the obstacle is given by [Got07, p. 273]:

$$\tau = \frac{Gb}{l - 2r} \tag{5.2.11}$$

were according to Fig. 5.2.1 l is the distance between to obstacles and r the radius, respectively. The distance l mainly depends on degree of dispersion f, which is the number of particles per volume unit.

$$l = \frac{r}{\sqrt{f}} \tag{5.2.12}$$

Assuming that $r << l$ with Eq. 5.2.11 and Eq. 5.2.12 the orowan stress τ_{os} of the hardened alloy.

$$\tau_{os} = \frac{Gb\sqrt{f}}{r} \tag{5.2.13}$$

So the hardening effect is most effective, if the particles are small and finely dispersed [Got07, 271 ff.]
In case of coherent precipitates the dislocations can either overcome the obstacle by the described Orowan mechanism or by cutting through the precipitate. This cutting shears off the precipitate by a burgers vector $\overrightarrow{b}$ and in turn increases the phase boundary area. The increased phase boundary energy γ_{p} is the reason for an repulsive force F_c acting on the dislocation given by:

$$F_c = \gamma_{\mathrm{p}} \cdot r \tag{5.2.14}$$

Besides, also the paraelastic (Eq. 5.2.5) and diaelastic (Eq. 5.2.7) contribution due the changed shear modulus and lattice parameter change has to be considered. The overall repulsive force is the sum of all partial forces F_{max} and has to be compensated by an increased shear stress $\Delta\tau$. Because the paraelastic contribution scales with r it is simplified assumed that:

$$F_{max} \cong \Delta\tau b l_F \cong \gamma r \tag{5.2.15}$$

were l_F the Friedel length (Eq. 5.2.16) is the mean free dislocation length defined as:
Thus it becomes clear that the shear stress for cutting increases with $\sqrt{r}$ as followed:

$$\Delta\tau b \cong \sqrt[3]{\gamma}\sqrt{f} \cdot \frac{\sqrt{fr}}{6E_d} \tag{5.2.16}$$

The shear stress necessary for the Orowan mechanism however decreases with $\frac{1}{r}$ (Eq. 5.2.11). Of course the dislocation will take the path of least resistance. Hence, there is a critical particle size r_0 as shown in figure Fig. 5.2.2 which were the hardening effect has its maximum. At particle sizes smaller r_0 it is favorable to cut through the precipitate whereas with increasing size the Orowan mechanism becomes favorable and τ decreases [Got07, 270 ff.].

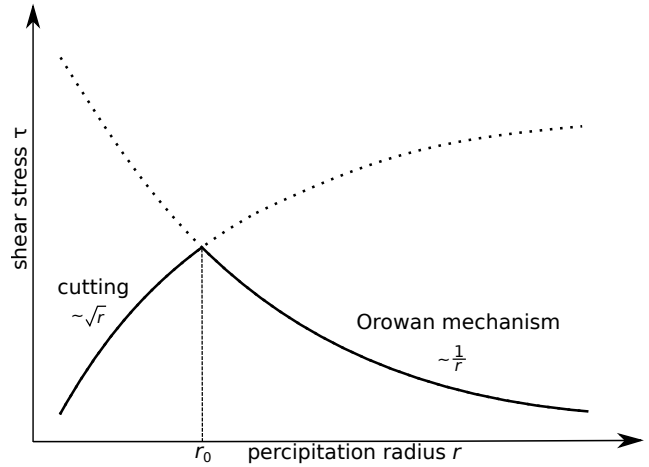

Figure 5.2.2: Schematic behavior of the shear stress depending on the precipitates radius r (With permission of Springer Science and Bus Media B V according to [Got07, p. 278]).

5.2.2 Annealing

In order to adjust the microstructure and material properties different types of heat treatments are used. All annealing treatments have in common that they are activated by a thermal induced change of atom positions in the crystal. The diffusion depends mainly on the number of vacancies, the type of atoms, lattice type and concentration gradients and is described by the Ficks' laws [Got07, p. 154].

$$j_{Di} = -D_i \cdot \vec{\nabla} C = -D_i \cdot grad(c_i) \tag{5.2.17}$$

Fick's first law describes that the diffusion current j_{Di} of an species i depends on the gradient of the concentration of the species c_i, were D_i is the material specific diffusion constant[Got07, p. 162]:

$$D_i = D_{0i} \cdot exp(-\frac{Q_i}{k_b T}) \tag{5.2.18}$$

Here, D_{0i} is a material constant, Q_i the activation energy for a position change, k_b the Boltzman constant and T the temperature.
The second law considers the time dependence of the concentration change in all space directions (x, y, z)[Got07, p. 156].

$$\frac{\partial c_i}{\partial t} = - \nabla j_i = D \triangle c_i = D \left(\frac{\partial^2 c_i}{\partial x^2} + \frac{\partial^2 c_i}{\partial y^2} + \frac{\partial^2 c_i}{\partial z^2} \right) \tag{5.2.19}$$

It should be stated that the activation energy Q for a position change depends strongly on the type of atom but also if the diffusion occurs in the bulk, or along interfaces or surfaces [Got07, 155 ff.] [HW06, 148 ff.].

$$Q_{surface} < Q_{interface} < Q_{bulk} \tag{5.2.20}$$

The previous discussed hardening mechanisms usually requires a suitable heat treatment for the deliberately control of diffusion. The aim can be homogenization, phase transformations, adjusting the grain size or the formation of precipitates. The most important quantity is here the temperature that is directly linked to the diffusion rate. Besides, also the cooling rate is important. By quenching it is for example possible to adjust the precipitate size, stabilize metastable phases or "freeze" impurity atoms in the lattice in order to increase the solid solution hardening. Even though the increased hardness is mostly desired, it usually also increases the internal stress in the material at cost of the ductility. Therefore, often special annealing treatments are necessary to reach a defect recovery and reduce those tensions which optimizes the strength and ductility. In general it can be distinguished between defect recovery and recrystallization. The driving force is in both cases the minimization of the energy stored in the lattice.
In the case of recovery, the annealing temperatures are below the recrystallization temperature T_{rec} but high enough to enhance the atom mobility which allows the recovery of vacancy agglomerates, lattice distortions due to impurity atoms or dislocations. The recovery thus decreases the energy due to elastic distortions in case of an dislocation for example [HW06, 154 ff.]:

$$E_d = \frac{1}{2} G b^2 \tag{5.2.21}$$

At higher annealing temperatures (T_{rec}) recrystallization occurs. As a rule of thumb it holds $T_{rec} \approx 0.5 \cdot T_{melt}$ [HW06, p. 154]. Recrystallization is usually desired in order to get rid of a strong texture or to adjust the grain size that directly influences the strength. The recristallization process is especially promoted in materials that exhibits a very high defect density like for example in cold worked material or even sputtered material. The reason is, that more defects mean more stored energy in the crystal and in turn an increased driving force due to energy minimization. It can be distinguished between primary, secondary and ternary recrystallization. Primary recrystallization is the restructuring of the entire microstructure by the nucleation of new grains. The new nuclei are formed preferred at defects especially along grain boundaries. With time the nuclei grow at expense of the deformed or defect rich grains. Because the newly formed grains exhibits a markedly decreased defect density, the energy or more precise the free enthalpy G_f is decreased. This change of the enthalpy per unit volume can be understood as pressure p acting on a grain boundary and is the driving force for the grain boundary movement [Got07, p. 308].

$$p = -\frac{\partial G_f}{\partial V} \tag{5.2.22}$$

Because the main contribution to the enthalphy reduction is given by the dislocation energy E_V (Eq. 5.2.21) depending on the dislocation density ρ_d, it can be written:

$$p \simeq \rho E_V \tag{5.2.23}$$

After the entire microstructure has reformed the new grains grow continuously. This means the mean grain size $\overline{d}$ increases but not the deviation. However especially at higher temperatures also non continuous grain growth is observed, which means that some already larger grains grow at the expense of smaller ones this manifests in an increase of $\overline{d}$ accompanied with an increase of the deviation. The difference can also be seen in a grain size distribution diagram shown in Fig. 5.2.3. In the case of noncontinuous grain growth called secondary recrystallization, a

characteristic bimodal distribution function is observed.

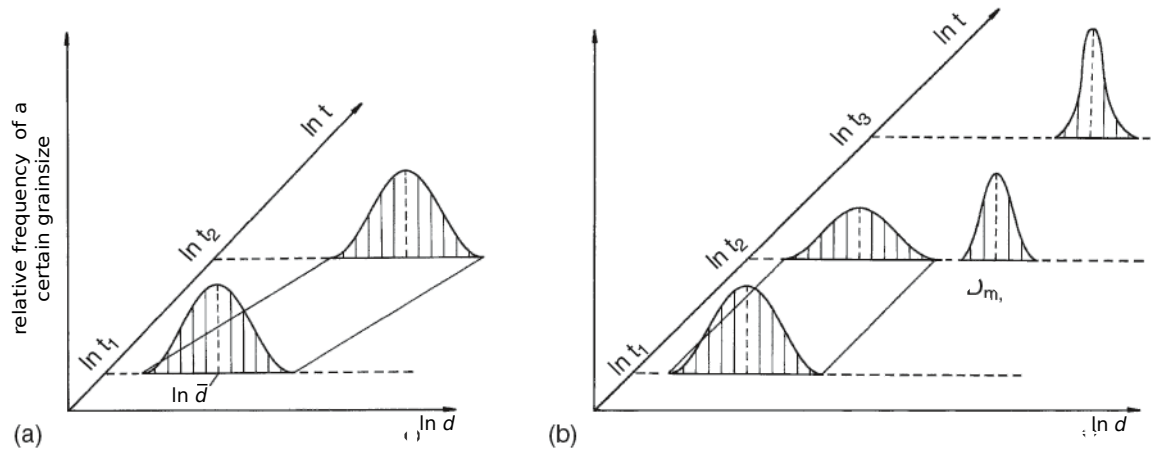

Figure 5.2.3: Frequency distribution of the grain size for a) primary and b) secondary crystallization (with permission of Springer Science and Bus Media B V according to [Got07, p. 307])

The driving force is in both cases the minimization of energy due to a reduction of grain boundary energy. If simplified, cubic grains with an edge length d are considered, with Eq. 5.2.22 and the grain boundary energy γ_g it follows for the driving force [Got07, p. 310]:

$$p = \frac{dG_F}{dV} = \frac{3d^2\gamma}{d^3} = \frac{3\gamma}{d} \tag{5.2.24}$$

It has to be stated that the driving force in case of secondary recrystallization is much smaller than for the primary. This explains why it occurs much slower or at higher temperatures, respectively [Got07, 307 ff.].

5.2.3 TWIP and TRIP effect

When hardening a metallic material it is mostly a trade-off between strength and ductility. However, in the recent decades a new type of steel gained attention since they combine a high strength with a high ductility. They can be considered as a kind of improved Headfield-steel or dual-phase-steel.
Whereas the twinning induced plasticity TWIN and the transformation induced plasticity TRIP effect are similar in their influence on the mechanical properties and their driving force there are some important differences discussed in the following. The basic requirement for both effects is the existence of a parent austenitic (fcc) γ-phase stabilized at room temperature. Typical alloying elements for a γ-phase stabilization are Mn and Ni. The driving force for the effects are in both cases a low stacking fault energy (SFE). When the SFE is low enough, under a load it becomes energetically favorable to generate a stacking fault. So the plastic deformation by dislocation slip is suppressed. If the SFE is $< 20\,\mathrm{mJ\,m^{-2}}$, it comes to a strain-induced $\gamma \rightarrow \epsilon$ non-diffusive phase transformation (TRIP). These transformation occurs due to the glide of an a/6[11$\bar{2}$] partial dislocation creating stacking faults on every second parallel (111) plane, which generates a change in the stacking sequence [Neu13][LEC14].
As the SFE increases $>(20\,\mathrm{mJ\,m^{-2}})$ the phase transformation is suppressed and the same, a/6 <112> partial dislocation glide occurs collaborative on successive parallel (111) planes, and lead to twin formation within the γ matrix [Bou+11][LEC14].

The mechanisms of the two effects are schematically shown in Fig. 5.2.4.

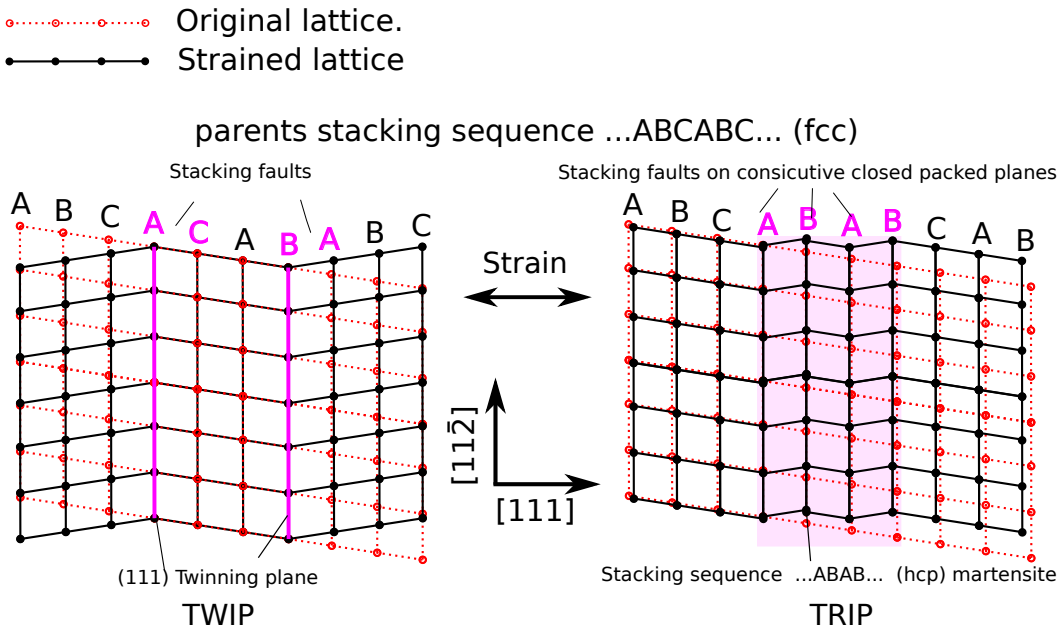

Figure 5.2.4: Scematic drawing of the TRIP and TWIP effect. In both cases strain induces displacement of a/6 in [11$\bar{2}$] direction on (111) planes. In case of the TWIP effect its a collaborative on successive parallel (111) planes. A generation of the same stacking fault on consecutive parallel (111) planes generates a change in the stacking sequence from ...ABCABC... to ...ABAB... and in turn a strain induced phase transformation, the TRIP effect.(modified according to[Liu+13])

Both the TRIP and the TWIP effect results in the combination of a high strength and ductility of the material. In case of the TRIP effect the local transformation of austenite to martensite lead to a local hardening at this spot mainly due to two reasons. The first reason is that the martensite itself is less ductile compared to the austenite. The second reason is that the phase boundaries, of martensite grains forming in the austenite matrix, are effective obstacles for the dislocation movement (Fig. 5.2.5). So the effect is similar to a grain refinement. Due to this local hardening the deformation occurs gradually in undeformed regions. This prevents an early necking and a allows high uniform deformation. Similar is also the behavior of TWIP steels. The difference is that the austenite is more stable and a strain induced martensite transformation is suppressed. Nevertheless the SFE of those alloys is still low so that twins are generated within the austenite matrix. These twins decreases the mean free path for dislocation movements and act as obstacles for the dislocation glide. This continious decrease of the dislocation mean free path and resulting strain hardening is also called dynamic Hall-Petch relation [Fon15, p. 372].
The dependency of the deformation mechanism from the SFE is schematically shown in Fig. 5.2.6. Because the Mn and C content also influences the SFE there is also a strong dependency of the deformation mechanism, depending on the concentrations of those elements.
As depicted in Fig. 5.2.8 besides Mn and C also Si, Al, Cr and Cu are important elements known to influence the deformation mechanisms TRIP/TWIP steels. Thus, in terms of biodegradable TRIP/TWIP steel especially Si and C are interesting elements for tailoring the mechanical properties [LEC14] [Grä+00][Fon15].
As shown in Fig. 5.2.7 low Mn contents favors the martensitic transformation (TRIP) whereas higher Mn and or C contents favors the deformation by twinning [Bou+11]. There is still no consensus in of the role and exact values for the different deformation mechanisms. It was also reported that the C content is of relevance, even when the SFE is constant [Fon15, 371 ff.]. Fur-

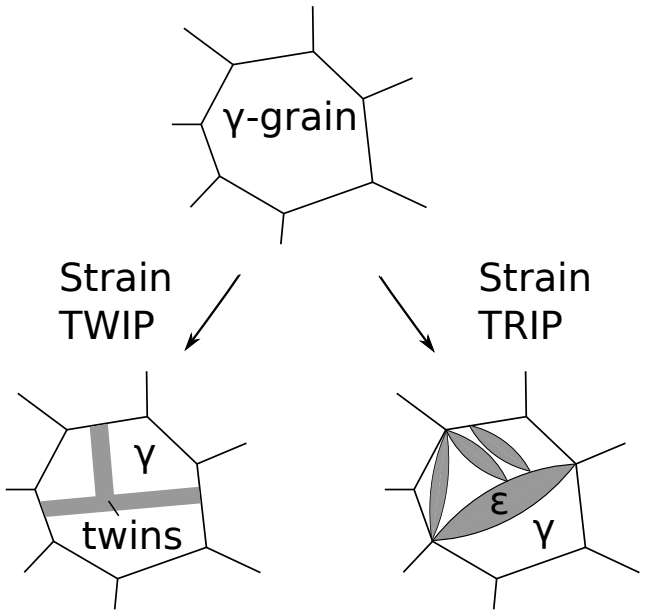

Figure 5.2.5: Schematic drawing of the generation of strain induced martensite (TRIP) or twins (TWIP) within the austenite matrix (with permission Springer Science and Bus Media B V, modified according to [Fon15, p. 371]).

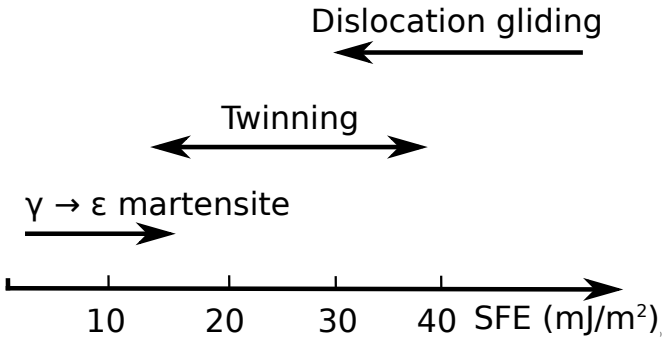

Figure 5.2.6: Dependency of the dominating deformation mechanism from the stacking fault energy (SFE) (with permission Springer Science and Bus Media B V, modified according to [Fon15, p. 373]).

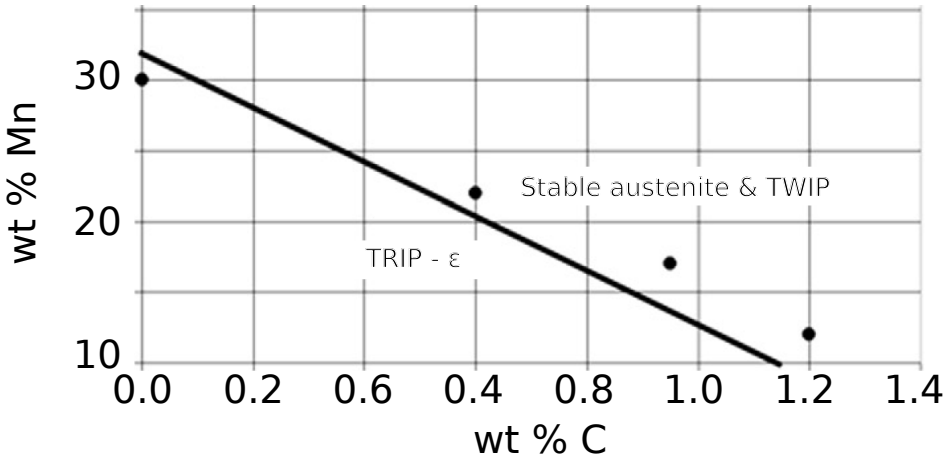

Figure 5.2.7: Deformation mechanism depending on Mn an C content (with permission of Elsevier, according to Schuhmann [Bou+11]).

thermore it was also stated that there is not a sharp bounder between the mechanisms and they can also coexist [DIN+06]. Thus, strain induced phase transformation, twinning and dislocation glide compete with each other. The influence of many factors composition, austenite stability annealing parameters and microstructure influences the mechanisms and material properties of FeMn steels in complex ways, going beyond the scope of this work [Fon15, 185 ff.] [HH06, 223 ff.].

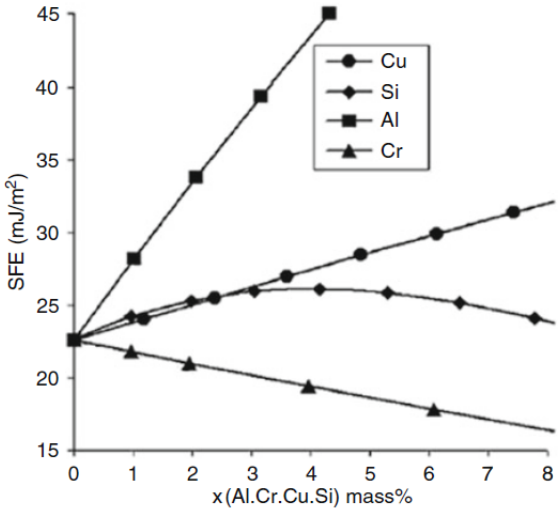

Figure 5.2.8: Influence of different alloying elements on the SFE of FeMn alloys (with permission of Springer Science and Bus Media B V, modified according to [Fon15, p. 385])

5.3 Fabrication of freestanding, Fe based devices via Magnetron sputtering

In this section the process flow of the fabrication process is explained and also some important insights that were found due to the work experience, regarding the fabrication of sputtered Fe-based devices are discussed.

5.3.1 Substrate structuring

In order to fabricate structured foils, the deposition was done on pre–structured substrates. Two different processes have been used, galvanically structured (GAL-S) substrates and structuring by reactive ion deep etching (RIE-S).
In Fig. 5.3.1 the process flow for the RIE-S is shown. At first (1) an image reversal photoresist is distributed via spin coating over the wafer. Afterwards the wafer is masked with a chromium photo mask (3). By further baking steps and a flood exposure (4-5) the resist becomes inert towards the developer. After the developing (6) the geometrical shape of the samples are free of resist. Next the wafer is coated with Al (7) followed by the stripping of the resist. Now the geometrical shape of the samples is present in form of an Al hard mask that serves at the same time as the sacrificial layer (8). Now the actual structuring of the wafer follows, done by reactive ion deep etching (9). Because the ablation rate is much higher for Si than for Al, at the unmasked regions a sink is formed. In order to make the process quasi anisotropic the etching is done in sequences with passivization steps in between, that prevent an strong attack of the side walls (See also [Mad02, 104 ff.]). After several cycles the etch depth is $\approx 80\,\mu m$ (9). Important is that the depth is higher than the desired film thickness to prevent a coalescence. After the

film deposition (10) the films are released from the substrate by selective chemical wet etching of the Al sacrificial layer, using a solution containing 20 % KOH.

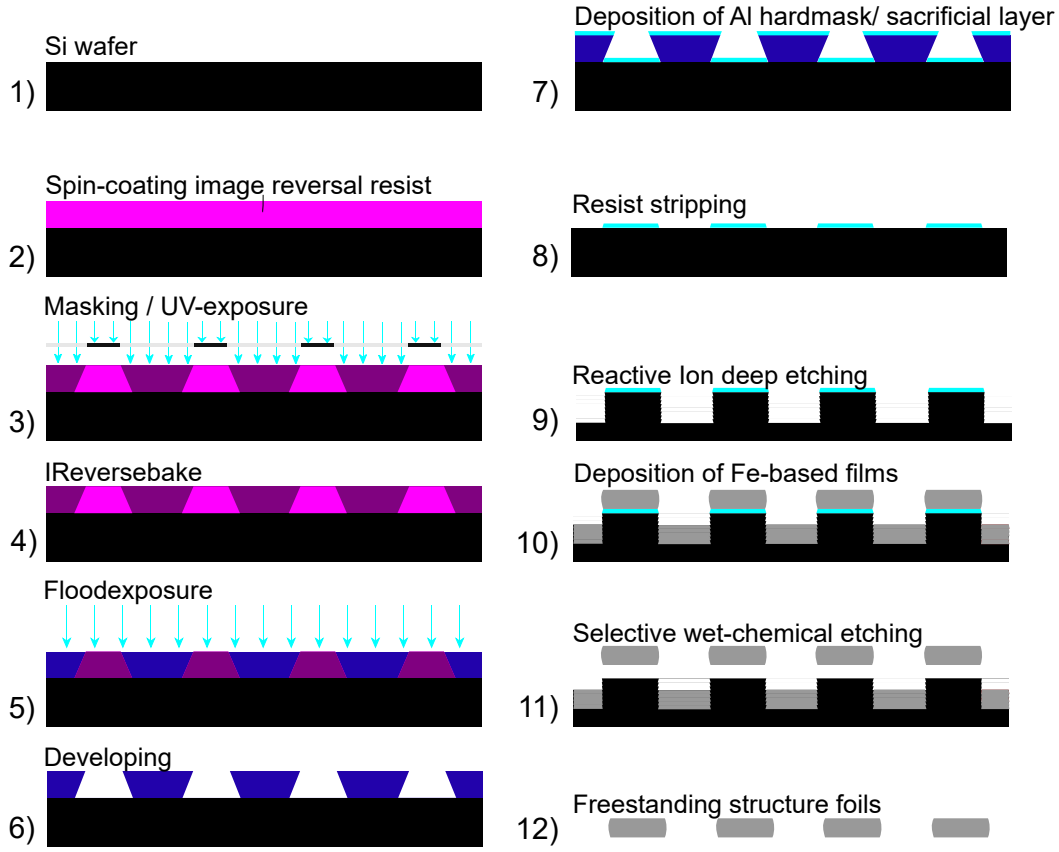

Figure 5.3.1: Scheme of the process flow for the substrate structuring by reactive ion deep etching.

In Fig. 5.3.2 a scheme for the GAL-S process is presented.
At first the wafer is coated with an $\approx 400\,\mathrm{nm}$ thick Cu layer (1) that serves as sacrificial layer and as conducting starting layer for the galvanic Cu deposition. The next step is the spin coating of the wafer with a positive photo resist (2). Afterwards the wafer is than masked and exposed to UV-light. After developing the resist is a $\approx 7\,\mu\mathrm{m}$ thick positive form of the sample geometry (4). Afterward the Cu is deposited galvanically with the same thickness like the resist (5). After stripping of the residual resist (6) the Cu is an negative mold of the samples. In the next step the Fe-based films are deposited (7). Finally the films are released by selective wet etching in a solution $70H_2O : 28NH_4(30\%) : 2H_2O_2(30\%)$.

Both methods are suitable for the fabrication of sputtered freestanding Fe-based devices with complex geometry and small feature sizes as shown in Fig. 5.3.3. The reason for applying different structuring methods are the substrate materials. Whereas for the fabrication of Fe and Fe-Au foils Si is suitable it was found that the deposition of FeMn on Si wafers is not possible. The reason are the different expansion coefficients α presented in Tab. 5.3.1. The problem is that when the deposition is done at elevated temperatures, the stress induced by the mismatch of the thermal expansion coefficients becomes too high so that the films are destroyed during the fabrication process. As a consequence alternative substrates were studied. As suitable substrate materials Al, Cu, Mg, stainless steel and quartz was found. However, the metallic substrate materials interfered with the selective wet etching reaction due to the galvanic coupling. Hence, in this work for the FeMn films quartz substrate was used. It has to be stated that quartz exhibits an anisotropic expansion coefficient. Thus, also the crystalline orientation have to be

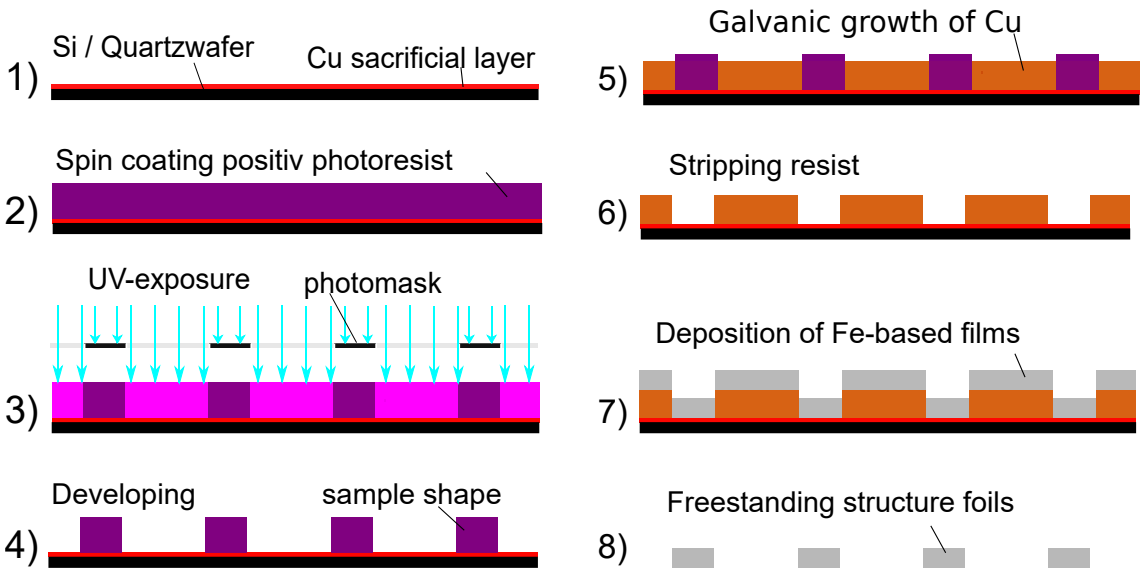

Figure 5.3.2: Scheme of the process flow for the substrate structuring by galvanic Cu deposition.

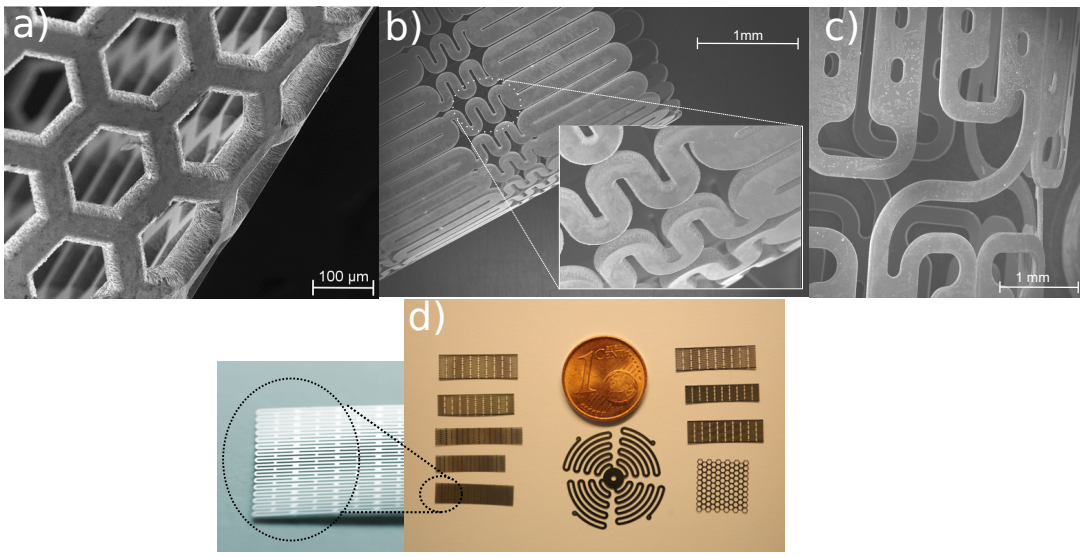

Figure 5.3.3: SEM images and photographs of different scaffolds and stent like freestanding Fe structures. The foils have a thickness of 60-80 µm and a minimal feature size of 20 µm.

considered. Since, perpendicular to the Z-axis α is isotropic and shows the best matching to the FeMn films, Z-cut wafers were used.

Table 5.3.1: Thermal expansion coefficients α of different materials

Material	α ($10^{-6}K^{-1}$)	Ref.
α–Fe	11.8	[Lid10]
α–Mn	21.7	[Lid10]
γ–FeMn30	≈18	[YYM81]
$\alpha - SiO_2 \parallel Z$	7.4	[KTN02]
$\alpha - SiO_2 \perp Z$	13.7	[KTN02]
$\alpha - Si$	2.6	[Lid10]
Al	23.1	[Lid10]
Cu	16.5	[Lid10]
Mg	24.8	[Lid10]
Stainless steel	16	[Kuc07]

5.3.2 Film growth

The sputter deposition is a complex process and a number of process parameters have to be considered in order to get the desired film properties. The most important properties are the process gas flow and pressure, power and substrate temperature. For thick films, that shall be released from the substrate a certain film stability is indispensable. These stability is directly linked to the microstructure of the growing film. The relationship between the process parameters pressure and the microstructure is well studied and presented in the structure-zone model Fig. 5.3.4 developed by Thornton et al. [Tho74] [Tho77b] [Tho77a] [Tho86]. It describes the change of the evolving microstructure with the change of pressure and substrate temperature T_s relative to the melting point T_{melt}. In the zone 1 the growth is determined by the low surface diffusion that prevents the growth of a dense structure. In this regime needle like grains are observed that exhibit an high defect density. The low surface diffusion and shadowing effects prevent the formation of dense grain boundaries and lead also to a certain porosity. Thus especially mechanical properties are quite poor.
As the substrate temperature is increasing the more dense (zone T) structure is formed. Here fibrous grains are present. However, due to the limited diffusion, shadowing can lead to less dense grain boundaries compared to bulk material. Hence, even though the strength can be very high. Those films usually exhibits a very limited ductility. If the substrate temperature increases further the increasing ad atom mobility is able to form more and more dense grain boundaries and result in the zone 2, the development of columnar grains with a small lateral grain size. Due to the important influence of shadowing effects also the substrate roughness plays is relevant for the evolving structue. As smoother the substrate as higher is the probability for the evolution of a zone T or even zone 2 growth [Tho77a] [Tho86]. It was reported that the mechanical properties of those zone 2 films are similar to mechanical worked films due to the fine grained structure and the high density of stacking faults dislocations and vacancies [Bun77]. At elevated temperatures the zone 3 regime can be observed. In this region the growth is determined by bulk diffusion and enables in situ recrystallization. Thus, the microstructure and as a consequence the mechanical properties, becomes more and more similar to those of cast material.

From this considerations it becomes clear, why for the fabrication of the samples in this work high substrate temperatures were necessary. The experience drawn from the experiments have shown that substrate temperatures of 250 –400 °C are necessary to achieve a sufficient film

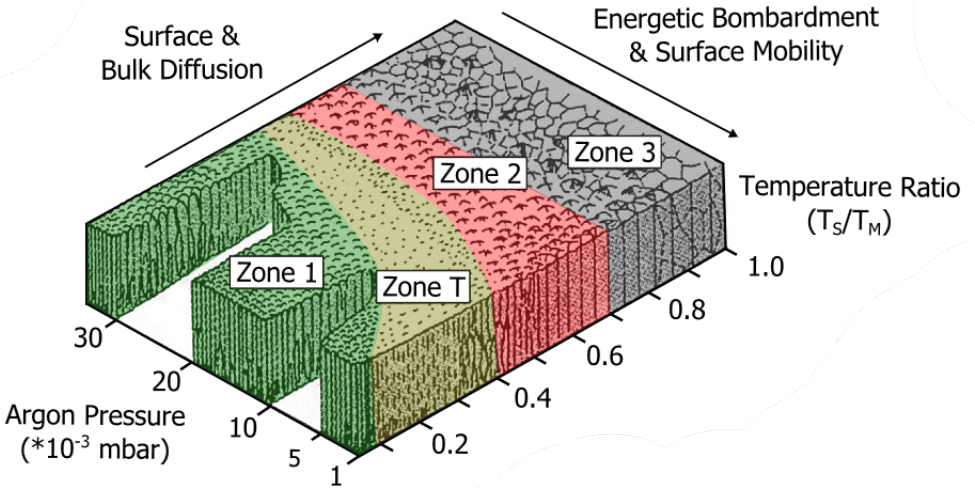

Figure 5.3.4: Modified structure zone model (with permssion of AIP Publishing, modified according to Thornton [Tho86] from [Yar17]).

stability necessary to keep the mechanical integrity during releasing the foils by the selective etching. The resulting T_s/T_{melt} ratio is $\approx$ 0.3–0.7 and fits to the high temperature end of the zone T, were a sufficient dense structure and stability can be expected. Additionally the elevated temperatures are beneficial in order to reduce the internal film stress.
Due to apparatus reasons a active substrate heating is not always possible. Therefore, an indirect way was chosen and the required heat input was ensured by using a high power. This increased power W increases one hand the sputter rate r_s since $W \propto r_s$ and on the other hand the energy of the ions in the sputtering chamber. As a consequence more energy is dissipated in form of heat in the substrate. The higher sputter rate as a result of the required high power is a beneficial side effect because the fabrication time is reduced, which is especially important for the fabrication of rather thick films. On the other hand, due to the high temperatures of the substrate, the possibility of substrate structuring using polymers is very limited.

6 Publications

6.1 Magnetron Sputtering a New Fabrication Method of Iron Based Biodegradable Implant Materials

Own contributions presented in this article:
- Sample preparation
- Measurements
- Evaluation of the data
- Writing of the manuscript

The motivation of this study was to proof that magnetron sputtering is a feasible method to fabricate freestanding structured pure-Fe films and their characterization in terms of the relevant material properties, for the intended use as biodegradable material.

Hindawi Publishing Corporation
Advances in Materials Science and Engineering
Volume 2015, Article ID 294686, 9 pages
http://dx.doi.org/10.1155/2015/294686

Research Article

Magnetron Sputtering a New Fabrication Method of Iron Based Biodegradable Implant Materials

Till Jurgeleit, Eckhard Quandt, and Christiane Zamponi

Chair for Inorganic Functional Materials, Institute for Materials Science, Faculty of Engineering, University of Kiel, Kaiserstrasse 2, 24143 Kiel, Germany

Correspondence should be addressed to Till Jurgeleit; tiju@tf.uni-kiel.de

Received 17 September 2015; Revised 3 December 2015; Accepted 6 December 2015

Academic Editor: Jörg M. K. Wiezorek

Copyright © 2015 Till Jurgeleit et al. This is an open access article distributed under the Creative Commons Attribution License, which permits unrestricted use, distribution, and reproduction in any medium, provided the original work is properly cited.

It was shown in the previous decade that pure-iron has a large potential as a biodegradable medical implant material. It is necessary to tailor the material properties according to the intended use of the device. It is of great interest to investigate not only the influence of processing on the material properties but also alternative fabrication methods. In this work for the first time magnetron sputtering in combination with UV lithography was used to fabricate free standing, patterned pure-iron thick films. For the intended use as biodegradable implant material free standing thick films were characterized in terms of microstructure, degradation performance, and mechanical properties before and after various heat treatments. The influence of microstructural changes on the degradation behavior was determined by linear polarization measurements. The mechanical properties were characterized by tensile tests. Microstructure, surface, and composition were investigated by scanning transmission electron microscopy (STEM), energy dispersive X-ray spectroscopy (EDX), and X-ray diffraction (XRD) measurements. The foils exhibited a preferential orientation in ⟨110⟩ direction and a fine grained structure. Furthermore they showed a higher strength compared to cast iron and corrosion rates in the range of 0.1 mm/year. Their mechanical properties were tuned by grain coarsening resulting in a slight increase of the degradation rate.

1. Introduction

The usage of metallic materials as medical implants such as stents, meshes, nails, plates, and screws nowadays is a common treatment. Implants often serve their purpose only during a healing period of 3–12 months [1, 2]; afterwards the presence of the implants involves the danger of complications such as stent restenosis and chronic inflammation reactions [3]. The best way to prevent such complications is the usage of degradable implants; therefore metal based, biodegradable materials are subject to intense research in recent years [1, 3–6]. The most prominent examples of biodegradable metals are magnesium and iron as well as some of their alloys [3]. Both metals are essential elements in the human metabolism. The degradation of pure-magnesium was reported to occur fast and with a significant amount of hydrogen evolution [7–10] while pure-iron degrades rather slow and without hydrogen evolution. Iron additionally exhibits a higher mechanical strength compared to pure-magnesium [1, 10, 11]. In vivo studies by Peuster et al. [1, 12] with New Zealand rabbits and mini pigs showed that it is possible to implant degradable pure-iron stents in the descending aorta. No significant obstructions of the vessel caused by inflammation, neointimal proliferation, or thrombotic events were observed in the study. Neither local or systemic toxicity nor an enrichment of corrosion products in the organs was found; however they found the corrosion rate of pure-iron to be too slow.

In the previous decade several attempts were presented [4, 11, 13–22] with the aim to tailor the degradation performance and the mechanical properties of iron by influencing the grain structure or changing the material composition. In this work a new method to produce patterned and free standing pure-iron foils by magnetron sputtering in combination with UV-lithography is presented. The method is most commonly used in the thin film technology. The fabrication of bulk, free standing NiTi thin films via sputtering was demonstrated

by Zamponi et al. [23, 24]. Lima de Miranda et al. [25, 26] showed that by using 3D lithography or micro laser welding 3D structures like tubular stents can also be produced by magnetron sputtering. A similar method for the fabrication of biodegradable, free standing, structured Mg-alloy foils by magnetron sputtering was presented by Schlüter et al. [27–29]. In order to modify corrosion behavior and mechanical properties, the sputter technology offers not only the opportunity of depositing pure-iron and alloys but also the fabrication of iron multilayer composites with noncompound forming elements [30].

Depending on the application sputtering allows a very precise control of the layer thickness from submicron scale up to 100 μm or even more, by varying the process parameters. Another important feature for the fabrication of implants is the freedom of design which is possible by the lithographic patterning and allows resolutions in the μm range.

For the intended use as biodegradable implant material the free standing foils were characterized with respect to corrosion behavior, mechanical properties, and microstructure. Furthermore the influence of ex situ heat treatments on the material properties was investigated.

2. Materials and Methods

2.1. Specimen Fabrication and Preparation. All films were deposited using a vonArdenne CS730 cluster sputtering machine with a base pressure in the 10^{-8} mbar range.

In the first step a 0.5 μm thick Cu sacrificial layer was sputtered on a 4″, 500 μm thick (100) oriented Si-wafer. The wafer was structured via UV-lithography followed by galvanic Cu-deposition in order to produce dog-bone shaped foils [18, 19]. Afterwards iron was deposited on these structured substrates. Due to the ferromagnetic nature of α-iron RF-sputtering was used to allow depositions at lower working gas pressures. A magnetically calibrated 8″ disk made of 99.9% pure cast iron was used as target material. To determine the temperature during the deposition, temperature indicators were used. The sputter parameters are listed in Table 1.

After the deposition of the iron, selective wet etching of the sacrificial layer was performed, using a solution containing DI-water, NH_3, and H_2O_2 in order to release the foils from the substrate. Finally the free standing, structured foils were cleaned in an ultrasonic bath with isopropanol and DI-water. In order to alter the microstructure the samples were annealed at 400°C, 600°C, and 800°C for two hours; additionally samples at 600°C were annealed for different times of 20 min, 1 h, and 2 h. The sputtered free standing Fe-foils (s-Fe) were annealed under reducing atmosphere (95% Ar and 5% H_2 VARIGON H5) in order to prevent oxidation.

2.2. Investigations of Microstructure. To determine the crystallinity and texture of the specimens XRD measurements were performed with a Seifert XRD-300 PTS X-ray diffractometer, employing monochromatic Cu-K_α radiation. The θ-2θ-absolute scans were performed in the range of 35° to 90° with 0.05° step width and 2 sec dwell time per step. Scanning transmission electron microscopy (STEM) was used to obtain further information about the microstructures; serving this purpose cross sections of the foils were prepared by focused ion beam (FIB) using a Helios NanoLab 600 (FEI). STEM images were captured using bright field (BF) and high angular annular dark field (HAADF) detectors. The determination of the average grain size was done by evaluating SEM surface images with a line intersection method [31]. Scanning electron microscopy on an Ultra Plus device by Zeiss was used to investigate the surface and fracture areas of the samples.

2.3. Mechanical Properties. Tensile tests were performed for mechanical characterization. Therefore "dog-bone" shaped samples (Figure 1) with 0.5 mm strut width and 7 mm strut length were produced as explained previously. The thickness was homogenous for all samples and varied depending on the batch between 28 μm and 32 μm.

The uniaxial tensile tests were performed with a testing machine of the type BETA 5-5/6 × 10 (Messphysik) using a special sample holder for thin samples. A straining rate of 0.4%/min was applied; the fracture criterion was set to 60% force reduction relative to the maximum applied force. For each heat treatment four samples were measured.

2.4. Corrosion Measurements. A VersaSTAT 3-300 potentiostat connected to a three-electrode cell was used for the electrochemical corrosion tests. Quadratic foils with an edge length of 15 mm and 10 μm thickness were used for the corrosion measurements. Since the foils exhibit mirror finish (R_a = 14 nm ± 3 nm) after deposition no additional conditioning or polishing steps were required. The samples were mounted on a sample holder acting as the working electrode (WE) with an exposed area of 0.916 cm^2. As counter electrode (CE) a Pt mesh as well as wire was used. An Ag/AgCl electrode in a 3-molar KCl solution acted as reference electrode (RE). Hank's balanced salt solution (HBSS) (H1387 Sigma Aldrich), modified with sodium bicarbonate (0.35 g/L), was used as electrolyte. The temperature was held constant at 37°C. Furthermore a regulated CO_2 inlet was used to keep the pH value at 7.4 ± 0.05. A schematic sketch of the setup is given in Figure 2.

After determining the corrosion potential U_c in an 4000 s long open circuit (OC) measurement, the measurement of the $I(U)$ curves was performed; for this the WE was polarized from −400 mV to +400 mV around U_c with a potential shift rate of 1 mV/s. The Tafel extrapolation method was employed to calculate the corrosion rate (CR) from the $I(U)$ curves [32, 33]. Using the exposed electrode area the current was converted into the current density. By fitting the linear regimes of the logarithmically plotted $j(U)$ curve followed by extrapolation to U_c, the corrosion current density j_c was determined. The corrosion rate was calculated using (1) which is based on Faraday's law [32, 33]:

$$\mathrm{CR} = \frac{j_c M}{n \rho F}. \quad (1)$$

Here M is the molar mass of the corroding species, ρ is the density, n is the number of transferred elementary charges per reaction step, and F is Faraday constant. Under the

Table 1: Sputtering parameters.

Element	Power (W)	Pressure (mbar)	Ar gas flow (sccm)	Sputter rate (nm/s)
Cu	1000 (DC)	$2.3 \cdot 10^{-3}$	25	4.1
Fe	600 (RF)	$2.3 \cdot 10^{-3}$	35	0.6

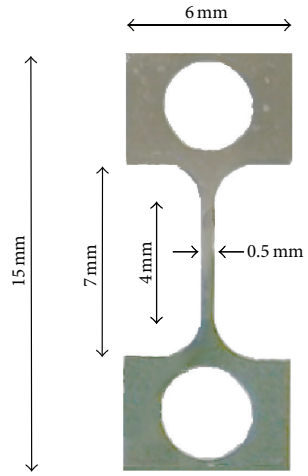

Figure 1: Dimensions of a "dog-bone" sample for tensile tests. The thickness of the different samples varied depending on batch between 28 μm and 32 μm.

assumption based on studies by Zhu et al. [34] on the degradation kinetics of pure-iron in physiological fluids, iron is anodic dissolved as follows: $Fe - 2e^- \rightarrow Fe^{2+}$, so that $n = 2$. With $M = 0.056$ kg/mol, $\rho = 7874$ kg/m^3, and a conversion factor of 31536, the CR can be calculated in terms of mm/year. For each annealing temperature four samples were measured.

3. Results and Discussions

3.1. Characterization of Microstructure. The XRD measurements (Figure 3) and the STEM investigations (Figure 4) of the as-deposited s-Fe showed a fine grained structure with columnar growth and strongly preferred orientation in the ⟨110⟩ direction. Since the samples were measured on a Si-substrate, additionally the Cu (111) reflection from the sacrificial layer and Si (400) reflection from the substrate are visible. Only the α-Fe (110) reflection is present after all heat treatments independent of the temperature. The s-Fe shows no sign of film stress, since a relaxation of film stress during annealing would lead to a shift in the XRD peak position. The evaluation of the average grain size is shown in Figure 5. The obtained results are in good agreement with STEM images (Figure 4). A similar microstructure is observed for the as-deposited sample and those annealed at 400°C. After annealing at 600°C and two hours the samples show an inhomogeneous grain growth, whereas some grains grow up to diameters of 2.5 μm; other grains retain the initial size (0.5 μm). After annealing for two hours at 800°C on the one hand large grains up to 15 μm and on the other hand small grains in the range of 0.5 μm to 1 μm were observed.

Thornton and Hoffman [35–39] established the structure zone model which explains the dependence of the deposition conditions on the microstructure of sputtered films. The ratio of substrate temperature to melting temperature T_{sub}/T_{melt} as well as the working gas pressure during the deposition has a strong influence on the film growth. Considering the measured substrate temperatures (≈400°C), the ratio $T_{sub}/T_{melt} \approx 0.37$ results in small columnar defect rich grains (Figure 4, as-deposited). As expected annealing at 400°C shows no influence on the microstructure since the temperature is too low for a recrystallization ($T_{sub}/T_{melt} \approx 0.4$–$0.5$) or defect recovery. At 600°C ($T_{sub}/T_{melt} = 0.48$) the recrystallization starts. By increasing the annealing temperature to 800°C the recrystallization can propagate much faster, due to an enhanced generation of thermal vacancies and the increased self-diffusion. Since all samples before and after annealing show the columnar ⟨110⟩ oriented grains, a secondary recrystallization mechanism is assumed, where large grains grow at the expense of smaller ones by shifting their grain boundaries in order to minimize the grain boundary and dislocation energy. In a review paper by Thompson [40] dealing with the recrystallization in thin films, it is stated that recrystallization processes in nonbulk samples, where the smallest sample dimension is much larger compared to the grain size, surface, and interface energies play an important role. Particularly if the columnar grains extend over the entire sample thickness usually primary grain growth stops and secondary recrystallization processes occur. Thus the observed recrystallization behavior is explained by the grain structure and small sample dimensions of the sputtered iron foils.

3.2. Mechanical Properties. Some exemplary stress-strain curves of s-Fe after annealing with different annealing temperatures and annealing times are given in Figure 6. Mean values and standard deviation of the measured samples, as well as some literature values for biodegradable metals, are listed in Table 2. In general with increasing annealing temperature or time a decrease of strength and an increase of the ductility can be observed. The fracture area of an as-deposited tensile test sample is shown in Figure 7(a). A ductile fracture behavior with a clear necking can be observed. The samples annealed at 600°C and various times (Figure 6) show that the biggest change in the mechanical properties occurs between one- and two-hour heating time, giving an impression about the recrystallization speed. The obtained values are correlated to the annealing temperature and yield strength in Figure 7. According to the Thornton model [35–38] and the substrate temperature, the as-deposited structure is in the low temperature end of the transition zone where a large amount of defects

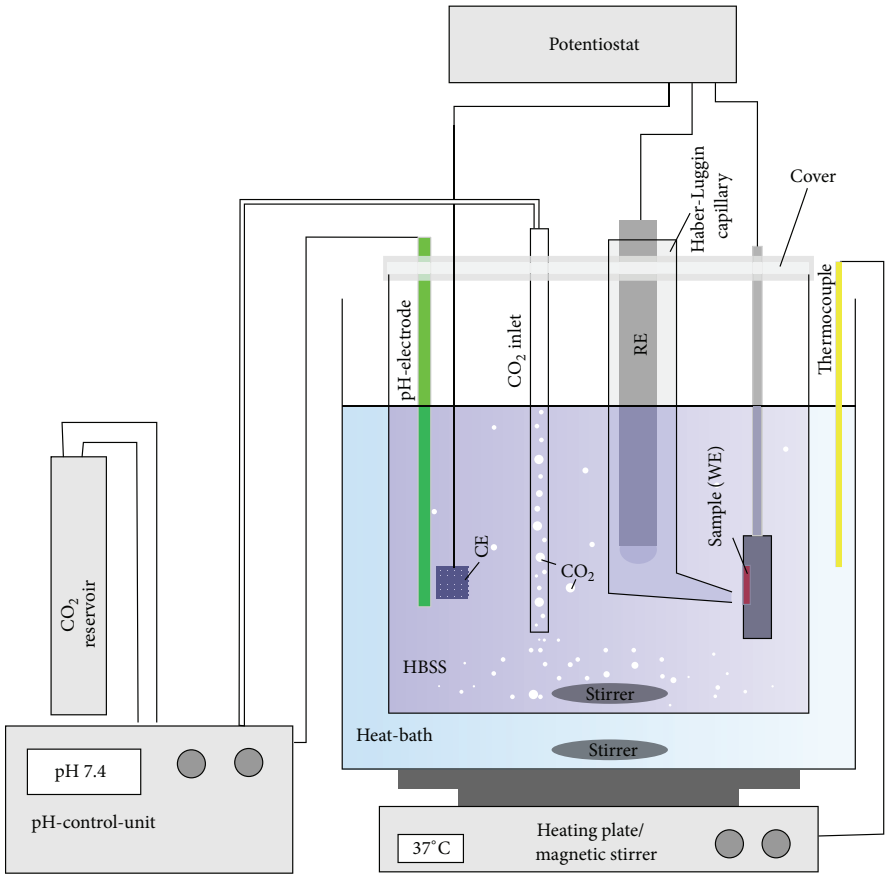

FIGURE 2: Schematic sketch of the corrosion measurement. A standard three-electrode setup is placed in the corrosion cell filled with Hank's buffered salt solution. The temperature is held at 37°C by a heating bath. By measuring the pH-value CO_2 inlet regulation the pH value of the solution is constantly kept at 7.4.

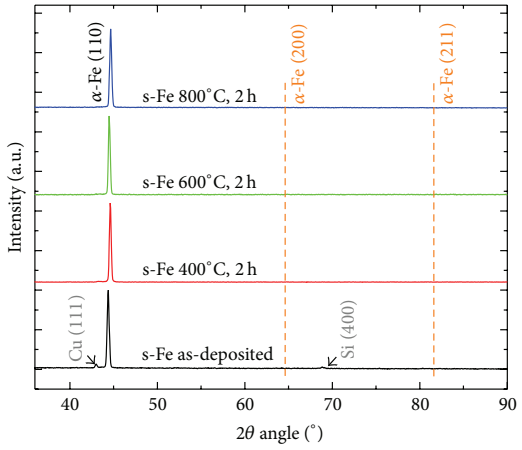

FIGURE 3: XRD θ-2θ scan of as-deposited and annealed s-Fe foils. Due to the preferred (110) orientation before and after annealing, only the corresponding reflection is visible. No peak shift due to stress relaxation is noticeable. Also the possible α-Fe (200) reflection and α-Fe (211) reflection are indicated by vertical dash lines.

like dislocations, vacancies, and stacking faults is present. The reason for this is particles of high kinetic energy which hit the surface and thus enhance the formation of defects. Due to the substrate temperature during the deposition there is not enough activation energy for significant bulk diffusion which would lead to in situ annealing during the deposition. So the high initial strength is explained by the large amount of defects. Since the defects act as obstacles for dislocation movement and plastic deformation, respectively, the high defect density results in high internal stresses during the deformation which leads to an early fracture.

The presented results are in good agreement with studies on the mechanical properties of sputtered films reviewed by Bunshah [41]. In the review paper it was concluded that metals, sputtered in temperature regions corresponding to the transition zone, show a high strength and a low ductility comparable to those of mechanical worked material (see also Table 2, UD*-Fe). Due to the increased grain growth at high temperatures a decrease of the strength is observed. This behavior is explained by the grain coarsening in agreement with the well-known Hall-Petch relation [42].

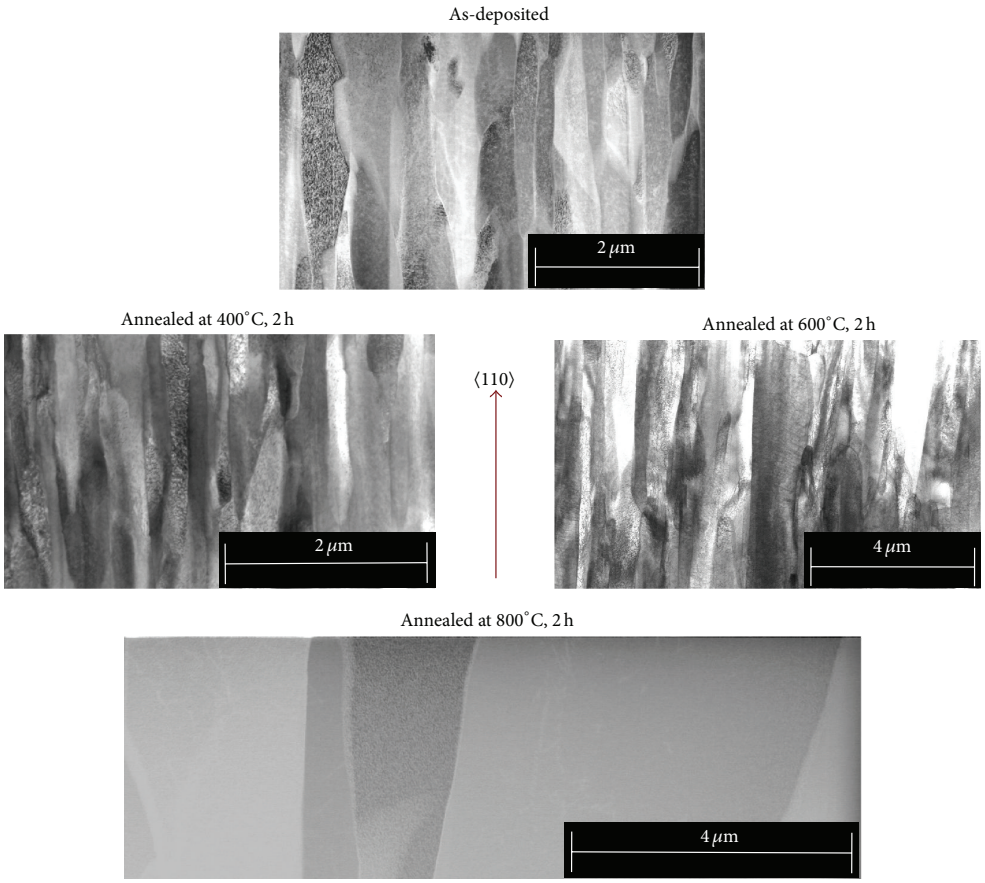

Figure 4: STEM images of s-Fe annealed at different temperatures for two hours.

Table 2: Measured mechanical properties of s-Fe after different annealing treatments and published literature values.

Sample	Yield strength (MPa)	Ultimate tensile strength (MPa)	Strain at fracture (%)
s-Fe as-deposited	606 ± 33	634 ± 33	1.4 ± 0.1
s-Fe annealed at 400°C, 2 h	604 ± 19	616 ± 9	1.6 ± 0.4
s-Fe annealed at 600°C, 20 min	612 ± 20	638 ± 10	1.3 ± 0.2
s-Fe annealed at 600°C, 1 h	568 ± 23	584 ± 33	2.0 ± 0.5
s-Fe annealed at 600°C, 2 h	381 ± 29	413 ± 9	13 ± 3.6
s-Fe annealed at 800°C, 2 h	267 ± 7	343 ± 4.7	20 ± 2.6
E[#]-Fe annealed at 550°C [14]	270 ± 6	292 ± 14	18.4 ± 4
E[#]-Fe annealed at 600°C [14]	130 ± 7	169 ± 9	32.3 ± 5
Cast iron annealed at 550°C [14]	140 ± 10	205 ± 6	25.5 ± —
Fe35Mn [15]	234 ± 7	428 ± 7	32.0 ± 0.8
Armco Fe annealed [19]	170 ± —	270 ± —	49.3 ± —
Fe(X) alloys as cast [18]	100–220	200–360	10–25
Fe(X) alloys as rolled [18]	360–450	430–850	5–9
UD[*]-Fe [20]	593 ± 2	600 ± 8	3.5 ± 2
UD[*]-Fe annealed [20]	246 ± 3	283 ± 5	34.8 ± 8
WE43 Mg alloy [8]	198 ± —	277 ± —	17 ± —
316L SS [3]	190 ± —	490 ± —	40 ± —

[#]Electroformed.
[*]Unidirectional rolled.

Table 3: Results of linear polarization corrosion measurements of s-Fe samples compared literature values.

Sample	Corrosion rate CR (mm/year)	Corrosion potential U_c (V)
s-Fe as-deposited	0.06 ± 0.02	−0.487 ± 0.052
s-Fe annealed at 400°C, 2 h	0.07 ± 0.01	−0.579 ± 0.015
s-Fe annealed at 600°C, 2 h	0.08 ± 0.04	−0.659 ± 0.016
s-Fe annealed at 800°C, 2 h	0.10 ± 0.01	−0.663 ± 0.081
E#-Fe as-deposited [14]	0.85 ± 0.05	−0.824 ± 0.018
E#-Fe annealed [14]	0.51 ± 0.06	−0.776 ± 0.020
Cast-iron annealed [14]	0.16 ± 0.04	−0.732 ± 0.016
Fe35Mn [15]	0.4 ± 0.1	N/A
Pure Fe [18]	0.10 ± —	−0.748 ± —
Fe(X) alloys as rolled [18]	0.10–0.18	−0.680–(−0.728)
Armco Fe annealed [19]	0.21 ± 0.04	−0.735 ± 11
UD*-Fe annealed [20]	0.24 ± 0.02	−0.724 ± 4
Pure-Fe [10]	0.10 ± —	−0.748 ± —

#Electroformed.
*Unidirectional rolled.

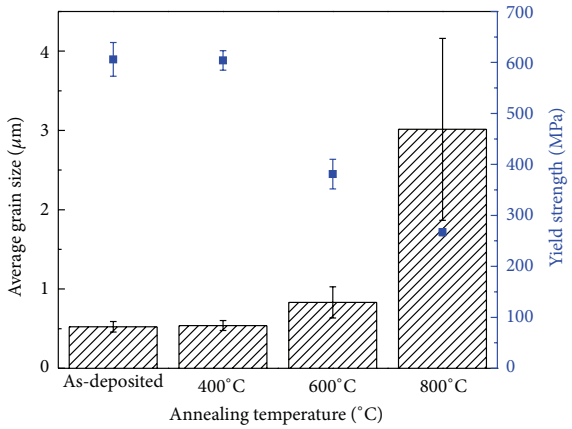

Figure 5: Graphical correlation between grain size, annealing temperature, and the yield strength of s-Fe annealed for two hours.

Due to the discussed recrystallization behavior the grain growth is nonhomogeneous; thus the very small grains which coexist with the larger ones act as obstacles for plastic deformation and therefore counteract the decrease of the strength explaining the comparably high residual strength after annealing. Increasing the annealing temperature and time strongly enhances the ductility of the material at the expense of its strength. This is mainly due to the recovery of defects which in turn reduces internal stresses necessary for dislocation movement. Due to patterning process the edges show a higher roughness compared to the surface (Figure 7(b)), which can act as a nucleus for crack initiation. Therefore the strain at fracture could be further increased by improving the quality of the edges by chemical polishing or electropolishing, respectively.

A graphical summary of the results and comparison to literature values for biodegradable materials are given in Figure 8. Compared to the WE43 Mg alloy and pure-iron values from the literature [8, 14, 18–20] the presented annealed s-Fe shows a higher strength. The values are approaching those of the 316L SS alloy which acts as gold standard [3] for vascular stents and other iron based biodegradable Fe alloys [15, 18]. With regard to possible applications it has to be considered the best compromise between strength and ductility to tailor the mechanical properties by appropriate heat treatments.

3.3. Corrosion Measurements. Some exemplary linear polarization curves for s-Fe annealed at different temperatures are shown in Figure 9. With increasing grain size, a shift of the corrosion potential to more negative values can be observed. This is associated with a slight increase of the corrosion rate. The calculated mean values and standard deviations are summarized in Table 3. The results of this study are in good agreement with those found by Cheng and Liu [10, 18]. It is well known [13, 19–21, 43] that changes in the grain size affect the corrosion rate of iron. For biodegradable Mg-alloys it was shown [42, 43] that grain refinement leads to an improved corrosion resistance. Also Obayi et al. [19, 20] qualitatively observed the same behavior for pure-iron. Studies by Ralston et al. [44] and Nie et al. [21, 22] on the degradation kinetics of nanocrystalline (NC) and microcrystalline (MC) pure-iron concluded that, in metals which tend to the formation of passive oxide layers such as iron, an increase of the grain boundary density promotes the formation of a passivation layer. However

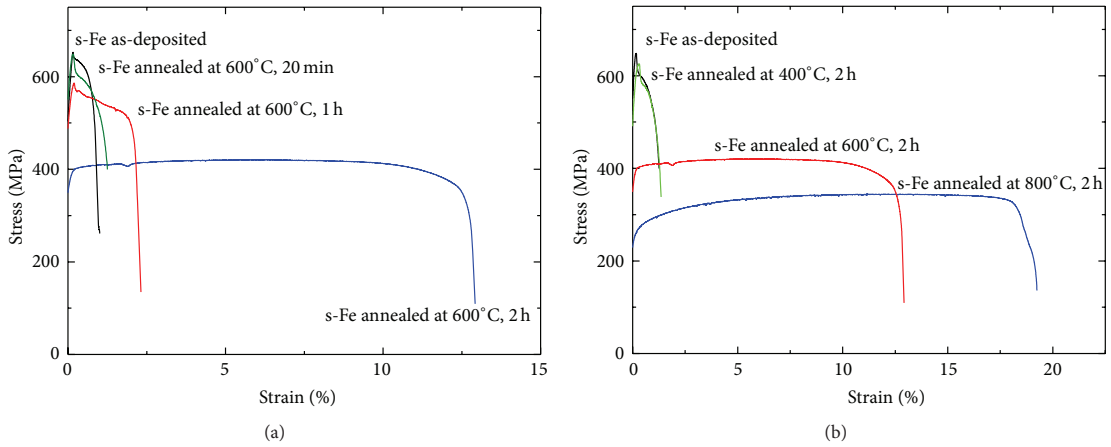

FIGURE 6: Exemplary stress strain curves of s-Fe annealed at 600°C for different dwell times (a) and at different temperatures for two hours (b).

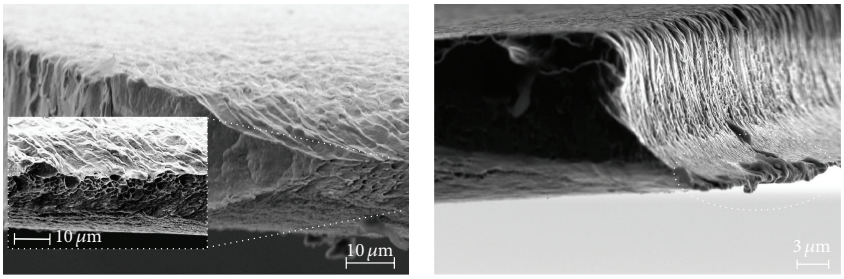

FIGURE 7: SEM image of fracture area (a), with significant necking. SEM image of the rough edge surface of an as-deposited dog-bone sample (b). The highlighted "feet" arises due to shadowing effects of the galvanic deposited Cu during sputtering on the substrate side.

studies by Moravej et al. [14] with electroformed iron (E-Fe) showed a decrease in the CR with increasing grain size; this behavior was related to the large amount of defects which are acting as active sites for corrosion. Since in general the sputtered microstructure shows similar characteristics, also a similar corrosion behavior could be expected. However the used target material in this study has a higher purity compared to those reported for the E-Fe. Therefore the high corrosion rates reported in the study could be related to the impurities acting as active sites for corrosion. The comparably low corrosion rate in this study can be explained by the high purity and fine-grained microstructure which promotes the formation of a passive layer. The slight increase of the corrosion rate with increasing grain size is assumed being attributed to a thinner and less stable passive oxide on larger grains [21, 22, 44]. However counteracting to this effect there is a decrease in the defect density which might be the reason for the rather weak influence of the grain coarsening on the corrosion rate.

4. Conclusion

It is shown that it is possible to produce free standing, patterned, pure-iron foils via magnetron sputtering. The foils show improved mechanical strength compared to cast Fe. It is possible to adjust the mechanical properties by a postdeposition annealing process. The samples show a comparable low degradation rate which is slightly increased by annealing and grain coarsening. Due to the higher mechanical strength thinner structures suffice to resist a load in a potential device, so that less material has to degrade. Moreover the presented method offers a large freedom of design which allows the fabrication of filigree structures. In combination with the high strength suitable designs can increase the surface to volume ratio and thus offer the potential to relativize the rather low corrosion rate.

Additionally there are a number of possibilities to accelerate the rate further by the deposition of more complex iron based systems. One possibility is the usage of prealloyed

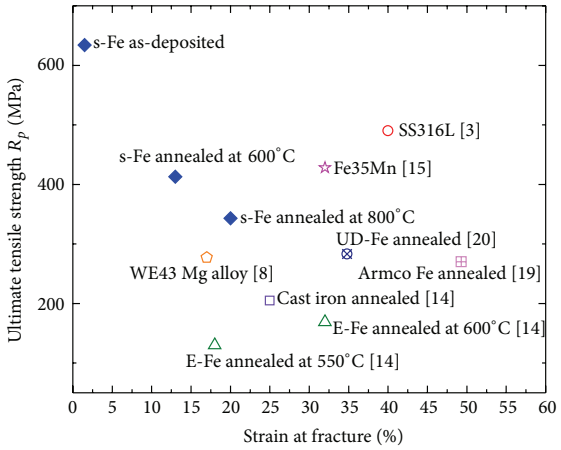

FIGURE 8: Overview of the mechanical properties found in this study for different annealed samples (as-deposited, 600°C, 2 h, and 800°C, 2 h) compared to literature values for biodegradable materials.

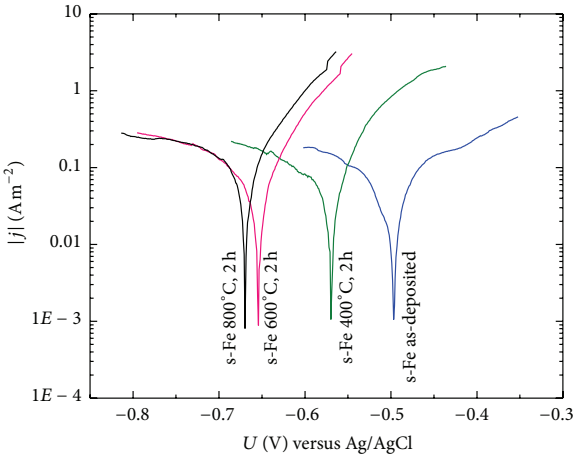

FIGURE 9: Exemplary Tafel-curves of s-Fe annealed at different temperatures for two hours. With increasing annealing temperatures a shift of U_c to more negative values and slight increase of j_c is observed.

sputter-targets with suitable elements. Another approach is the fabrication of multilayer composites with solvable or even nonsolvable elements. In combination with appropriate postdeposition heat treatments it is possible to fabricate in this manner tailored microstructures and material properties, respectively.

Investigation in terms of foil thickness and patterning resolution limits are subject of current research. Furthermore it has to be proven that the mentioned 3D lithography or microlaser welding [25, 26] can be applied for iron based sputtered material to allow the production of three dimensional devices like stents. Since the in vitro characterization can just compare different materials in terms of their properties, in further studies in vitro cell tests have to be performed to assess how the material could behave in vivo.

The magnetron sputtering technique in combination with UV-lithography allows the fabrication of in situ patterned devices. Thus magnetron sputter technology offers a large potential to further improve the mechanical properties and corrosion behavior. Finally the presented method is a promising candidate in the fabrication technology of iron based, biodegradable devices with filigree designs.

Conflict of Interests

The authors declare that there is no conflict of interests regarding the publication of this paper.

Acknowledgments

Funding via DFG is gratefully acknowledged. The authors further acknowledge Jan Johansen and Bastian Hirsch for supporting this work in the tensile tests.

References

[1] M. Peuster, C. Hesse, T. Schloo, C. Fink, P. Beerbaum, and C. von Schnakenburg, "Long-term biocompatibility of a corrodible peripheral iron stent in the porcine descending aorta," *Biomaterials*, vol. 27, no. 28, pp. 4955–4962, 2006.

[2] P. K. Bowen, J. Drelich, and J. Goldman, "Zinc exhibits ideal physiological corrosion behavior for bioabsorbable stents," *Advanced Materials*, vol. 25, no. 18, pp. 2577–2582, 2013.

[3] H. Hermawan, *Biodegradable Metals: From Concept to Applications*, Biodegradable Metals for Cardiovascular Applications, Springer, Heidelberg, Germany, 2012.

[4] H. Hermawan, H. Alamdari, D. Mantovani, and D. Dubé, "Iron-manganese: new class of metallic degradable biomaterials prepared by powder metallurgy," *Powder Metallurgy*, vol. 51, no. 1, pp. 38–45, 2008.

[5] A. Colombo and E. Karvouni, "Biodegradable stents: 'fulfilling the mission and stepping away'," *Circulation*, vol. 102, no. 4, pp. 371–373, 2000.

[6] E. Wintermantel and S. Ha, *Medizintechnik mit Biokompatiblen Werkstoffen und Verfahren*, Resorbierbare Implantate, Springer, Heidelberg, Germany, 2007.

[7] M. P. Staiger, A. M. Pietak, J. Huadmai, and G. Dias, "Magnesium and its alloys as orthopedic biomaterials: a review," *Biomaterials*, vol. 27, no. 9, pp. 1728–1734, 2006.

[8] F. Witte, N. Hort, C. Vogt et al., "Degradable biomaterials based on magnesium corrosion," *Current Opinion in Solid State and Materials Science*, vol. 12, no. 5-6, pp. 63–72, 2008.

[9] F. Witte, "The history of biodegradable magnesium implants: a review," *Acta Biomaterialia*, vol. 6, no. 5, pp. 1680–1692, 2010.

[10] J. Cheng, B. Liu, Y. H. Wu, and Y. F. Zheng, "Comparative in vitro study on pure metals (Fe, Mn, Mg, Zn and W) as biodegradable metals," *Journal of Materials Science & Technology*, vol. 29, no. 7, pp. 619–627, 2013.

[11] Y. F. Zheng, X. N. Gu, and F. Witte, "Biodegradable metals," *Materials Science and Engineering R: Reports*, vol. 77, pp. 1–34, 2014.

[12] M. Peuster, P. Wohlsein, M. Brügmann et al., "A novel approach to temporary stenting: degradable cardiovascular

stents produced from corrodible metal—results 6-18 months after implantation into New Zealand white rabbits," *Heart*, vol. 86, no. 5, pp. 563–569, 2001.

[13] K. D. Ralston and N. Birbilis, "Effect of grain size on corrosion: a review," *Corrosion*, vol. 66, no. 7, 2010.

[14] M. Moravej, F. Prima, M. Fiset, and D. Mantovani, "Electroformed iron as new biomaterial for degradable stents: development process and structure-properties relationship," *Acta Biomaterialia*, vol. 6, no. 5, pp. 1726–1735, 2010.

[15] H. Hermawan, D. Dubé, and D. Mantovani, "Degradable metallic biomaterials: design and development of Fe–Mn alloys for stents," *Journal of Biomedical Materials Research Part A*, vol. 93, no. 1, pp. 1–11, 2010.

[16] F. Witte, V. Kaese, H. Haferkamp et al., "In vivo corrosion of four magnesium alloys and the associated bone response," *Biomaterials*, vol. 26, no. 17, pp. 3557–3563, 2005.

[17] M. Schinhammer, P. Steiger, F. Moszner, J. F. Löffler, and P. J. Uggowitzer, "Degradation performance of biodegradable FeMnC(Pd) alloys," *Materials Science and Engineering C*, vol. 33, no. 4, pp. 1882–1893, 2013.

[18] B. Liu and Y. F. Zheng, "Effects of alloying elements (Mn, Co, Al, W, Sn, B, C and S) on biodegradability and in vitro biocompatibility of pure iron," *Acta Biomaterialia*, vol. 7, no. 3, pp. 1407–1420, 2011.

[19] C. S. Obayi, R. Tolouei, A. Mostavan et al., "Effect of grain sizes on mechanical properties and biodegradation behavior of pure iron for cardiovascular stent application," *Biomatter*, 2014.

[20] C. S. Obayi, R. Tolouei, C. Paternoster et al., "Influence of cross-rolling on the micro-texture and biodegradation of pure iron as biodegradable material for medical implants," *Acta Biomaterialia*, vol. 17, pp. 68–77, 2015.

[21] F. L. Nie, Y. F. Zheng, S. C. Wei, C. Hu, and G. Yang, "*In vitro* corrosion, cytotoxicity and hemocompatibility of bulk nanocrystalline pure iron," *Biomedical Materials*, vol. 5, no. 6, Article ID 065015, 2010.

[22] F. L. Nie and Y. F. Zheng, "Surface chemistry of bulk nanocrystalline pure iron and electrochemistry study in gas-flow physiological saline," *Journal of Biomedical Materials Research Part B: Applied Biomaterials*, vol. 100, no. 5, pp. 1404–1410, 2012.

[23] C. Zamponi, H. Rumpf, C. Schmutz, and E. Quandt, "Structuring of sputtered superelastic NiTi thin films by photolithography and etching," *Materials Science and Engineering A*, vol. 481-482, pp. 623–625, 2008.

[24] R. Lima de Miranda, C. Zamponi, and E. Quandt, "Micropatterned freestanding superelastic TiNi films," *Advanced Engineering Materials*, vol. 15, no. 1-2, pp. 66–69, 2013.

[25] R. Lima de Miranda, C. Zamponi, and E. Quandt, "Fabrication of TiNi thin film stents," *Smart Materials and Structures*, vol. 18, no. 10, Article ID 104010, 2009.

[26] G. Siekmeyer, A. Schüßler, R. Lima de Miranda, and E. Quandt, "Comparison of the fatigue performance of commercially produced nitinol samples versus sputter-deposited nitinol," *Journal of Materials Engineering and Performance*, vol. 23, no. 7, pp. 2437–2445, 2014.

[27] K. Schlüter, Z. Shi, C. Zamponi, F. Cao, E. Quandt, and A. Atrens, "Corrosion performance and mechanical properties of sputter-deposited MgY and MgGd alloys," *Corrosion Science*, vol. 78, pp. 43–54, 2014.

[28] K. Schlüter, C. Zamponi, N. Hort, K. U. Kainer, and E. Quandt, "Polycrystalline and amorphous MgZnCa thin films," *Corrosion Science*, vol. 63, pp. 234–238, 2012.

[29] K. Schlüter, C. Zamponi, A. Piorra, and E. Quandt, "Comparison of the corrosion behaviour of bulk and thin film magnesium alloys," *Corrosion Science*, vol. 52, no. 12, pp. 3973–3977, 2010.

[30] C. Zamponi, U. Schürmann, T. Jurgeleit, L. Kienle, and E. Quandt, "Microstructures of magnetron sputtered Fe Au thin films," *International Journal of Materials Research*, vol. 106, no. 2, pp. 103–107, 2015.

[31] ASTM E-112, "Metal test methods and analytical procedures," in *Annual Book of ASTM Standards*, vol. 03.01, section 3, ASTM International, West Conshohocken, Pa, USA, 2007.

[32] M. Stern and A. L. Geary, "Electrochemical polarization: I . a theoretical analysis of the shape of polarization curves," *Journal of the Electrochemical Society*, vol. 104, no. 1, pp. 56–63, 1957.

[33] D. A. Jones, "Electrochemical kinetics of corrosion: polarization methods to measure corrosion rate," in *Principles and Prevention of Corrosion*, pp. 75–162, Pearson-Prentice Hall International, London, UK, 2005.

[34] S. Zhu, N. Huang, L. Xu et al., "Biocompatibility of pure iron: *in vitro* assessment of degradation kinetics and cytotoxicity on endothelial cells," *Materials Science and Engineering C*, vol. 29, no. 5, pp. 1589–1592, 2009.

[35] J. A. Thornton and D. W. Hoffman, "Internal stresses in titanium, nickel, molybdenum, and tantalum films deposited by cylindrical magnetron sputtering," *Journal of Vacuum Science & Technology*, vol. 14, no. 1, pp. 164–168, 1976.

[36] J. A. Thornton, "Influence of apparatus geometry and deposition conditions on the structure and topography of thick sputtered coatings," *Journal of Vacuum Science & Technology*, vol. 11, no. 4, pp. 666–670, 1974.

[37] J. A. Thornton, "High rate thick film growth," *Annual Review of Materials Science*, vol. 7, pp. 239–260, 1977.

[38] J. A. Thornton, "The microstructure of sputter deposited coatings," *Journal of Vacuum Science & Technology A*, vol. 4, no. 6, pp. 3059–3065, 1986.

[39] J. A. Thornton and D. W. Hoffman, "Stress-related effects in thin films," *Thin Solid Films*, vol. 171, no. 1, pp. 5–31, 1989.

[40] C. V. Thompson, "Grain growth in thin films," *Annual Review of Materials Science*, vol. 20, no. 1, pp. 245–268, 1990.

[41] R. F. Bunshah, "3.1 mechanical properties of PVD films," *Vacuum*, vol. 27, no. 4, pp. 353–362, 1977.

[42] R. W. Cahn and P. Haasen, "Recovery and recrystallization," in *Physical Metallurgy*, vol. 2, chapter 17, 4.2., p. 1589, Elsevier Science B.V., Amsterdam, The Netherlands, 4th edition, 1996.

[43] L. Jinlong and L. Hongyun, "The effects of cold rolling temperature on corrosion resistance of pure iron," *Applied Surface Science*, vol. 317, pp. 125–130, 2014.

[44] K. D. Ralston, N. Birbilis, and C. H. J. Davies, "Revealing the relationship between grain size and corrosion rate of metals," *Scripta Materialia*, vol. 63, no. 12, pp. 1201–1204, 2010.

6.2 Microstructures of magnetron sputtered Fe Au thin films

Own contributions presented in this article:
- Partially sample preparation
- Participation at the discussion of the results

The goal of this study was to proof that by the multilayer deposition of Fe and Au followed by annealing it is possible to implement Au precipitates in the Fe matrix.

From the journal: International Journal of Materials Research, vol.2, 2015, pages 103-107, authors: Zamponi, Christiane; Schürmann, Ulrich; Jurgeleit, Till; Kienle, Lorenz; Quandt, Eckhard. With permission of Carl Hanser Verlag GmbH & Co.KG, München.

International Journal of
MATERIALS RESEARCH

Zeitschrift für METALLKUNDE

Original Contributions

International Journal of Materials Research downloaded from www.hanser-elibrary.com by Hanser Verlag (Office) on February 25, 2015
For personal use only.

Christiane Zamponi, Ulrich Schürmann, Till Jurgeleit, Lorenz Kienle, Eckhard Quandt
Faculty of Engineering, Institute for Material Science, Christian-Albrechts-Universität, Kiel, Germany

Microstructures of magnetron sputtered Fe–Au thin films

Freestanding films of highly pure iron and gold multilayers were fabricated and characterized for their intended use as biodegradable implant materials. These samples were deposited using magnetron sputtering on unheated substrates. This technology allows the combination of various non-compounding materials. After annealing for 2 h at 685 °C and 850 °C, respectively to homogenize the multilayer, the microstructures were investigated using X-ray diffraction, energy dispersive X-ray spectroscopy and scanning transmission electron microscopy. Due to the annealing, the multilayered microstructure converts into a new multiphase system consisting of an iron matrix and two different kinds of gold morphologies: segregations along grain boundaries and nanosized core–shell like precipitates.

Keywords: Magnetron sputtering; Thin films; Iron–gold; Nanosized core–shell

1. Introduction

Biodegradable materials have been the subject of intense scientific research in recent years, in particular for their application as temporary medical implant materials, e. g. as coronary stents [1 – 4]. The motivation is to provide such a stent as a temporary opening to a narrowed arterial vessel until the vessel remodels, and to dissolve the no longer needed stent progressively thereafter [5 – 7]. The two most important metallic materials in this respect are magnesium and iron [8, 9]. Magnesium and its alloys are considered to be promising candidates for such applications and have already been successfully tested in vivo and in clinical studies [6]. In physiological media they exhibit appropriate or even rapid degradation rates accompanied by the evolution of considerable amounts of hydrogen, leading to potential premature device failure [7]. In contrast bio-corrosion of iron proceeds too slowly [10, 11], however the mechanical properties of iron are similar to commonly used stenting materials such as stainless steel. Nevertheless, preliminary in-vivo studies have already shown the potential of iron for degradable medical applications: stents made of pure iron implanted into porcine aorta did not induce any local or systemic toxicity [6]. Due to the very low degradation rate of pure iron in physiological media, such implants are considered to reveal reactions similar to those found in permanent applications [12]. For this reason there is a need to find an alloy with a higher degradation rate.

However, by alloying additional elements, corrosion as well as mechanical properties can be tuned [13 – 15]. In order to increase the degradation rate of Fe-based materials, Hermawan et al. [13, 16, 17] developed an FeMn alloy containing 35 wt.% Mn (Fe-35Mn) which exhibits an increased degradation rate with respect to pure iron [13]. Nevertheless, compared to magnesium alloys, the degradation rate of Fe-35Mn is still at least one order of magnitude lower and thus is still considered to be too slow for many temporary implant applications. To influence the corrosion Schinhammer et al. alloyed nobler metals such as Pd to FeMn with the intention of forming local galvanic elements [14].

In this paper a composite of pure iron and gold, fabricated by magnetron sputtering is investigated by means of X-ray diffraction (XRD), energy dispersive X-ray spectroscopy (EDX) and scanning transmission electron microscopy (STEM).

International Journal of Materials Research downloaded from www.hanser-elibrary.com by Hanser Verlag (Office) on February 25, 2015
For personal use only.

The iron–gold system is known as non-compounding and the solubility of gold in α-iron (body centered cubic (bcc)) is very low but gold is able to solve up to 74 at.% iron [18]. The magnetron sputtering technique allows the fabrication of a system with gold particles in an iron matrix.

2. Experimental procedure

Fe–Au thin films were deposited by RF and DC magnetron sputtering using a VonArdenne CS730 S sputtering system and unheated thermally oxidized silicon substrates with lateral dimensions of 15 mm × 15 mm and a thickness of 0.6 mm. As a sacrificial layer, 500 nm of Cu was deposited. The Fe–Au films were deposited using a multilayer approach with pure element Fe (3N5) and Au (4 N) targets (200 mm diameter) and a base pressure of 1×10^{-7} mbar. All investigated films contained 10 bilayers of Fe and Au with a total thickness of approximately 7 µm. The sputtering parameters used are summarized in Table 1.

The release of the Fe–Au films from the substrate occurs by selective wet etching of the Cu layer using a basic solution based on ammonia solution ($NH_3 + H_2O$), hydrogen peroxide (H_2O_2) and deionized water (H_2O). After removing the sacrificial Cu layer, the freestanding thin films were annealed for 2 h at 685 °C or 2 h at 850 °C in a vacuum furnace. At these temperatures the bcc α-Fe is stable and the eutectic point at 870 °C is not exceeded. After 2 h at the respective annealing temperature the furnace was removed from the vacuum chamber, which results in a cooling rate of approximately 7 K min^{-1}.

The microstructure of the samples was determined by X-ray diffraction with a Seifert XRD 3000 PTS using monochromatic Cu-K_α (θ–2θ scan, step width = 0.05°, step time = 3 s) at RT and a FEI Tecnai F30 STwin TEM (300 kV, field emission gun (FEG) cathode, spherical aberration coefficient $C_s = 1.2$ mm) to determine the lattice parameters of the iron and gold phases. In addition, the chemical composition of the investigated specimens was analyzed by EDX using an Inca Oxford silicon drift detector attached to an FEI Dualbeam Helios Nanolab. Furthermore, cross-sections of the films were prepared by focused ion beam (FEI Dualbeam Helios Nanolab) sectioning and milling. High angle annular dark field (HAADF)-STEM and EDX elemental mapping (Si/Li detector, EDAX) were performed in the TEM on these cross-sections to obtain detailed information about the microstructure via *Z*-contrast imaging and to investigate the Fe and Au distribution, respectively.

3. Results and discussion

Before the annealing step the bilayers of pure Au (10 nm, cf. bright horizontal lines in Fig. 1a) and pure Fe (700 nm) are visible. The iron layers show a columnar growth perpendicular to the bilayers, cf. broad irregularly shaped stripes in Fig. 1a. The Au layers did not hinder the growth of the Fe columnar grains. Borchers et al. [19] investigated magnetron sputtered Fe (2 nm)/Au (10 nm) multilayers (70) on Si <110> substrate by cross-sectional transmission electron microscopy and they showed that the multilayers exhibit bcc iron growth with a Nishiyama–Wassermann orientation relationship between the Fe and Au layers. Amran and Rabkin [20] deposited an Au–Fe bilayer on (0001) sapphire substrates and they found several orientation relationships between the bcc Fe and the face centered cubic (fcc) Au (Nishiyama–Wassermann, Kurdjumov–Sachs and Greninger–Troiano) depending on the deposition sequence. To achieve such orientation relationships the orientation and lattice distance of the substrates is important. In the present investigation, an amorphous SiO_2 surface with a sacrificial Cu layer on top is used as a substrate and the columnar growth of the Fe has no sign of epitaxial orientation.

During annealing two processes take place, depending on the temperature. The formation of thermal vacancies allows the self- and the impurity diffusion as well as the formation of interstitial Fe atoms in the Au-rich phase. The solubility of Fe in Au starts below 200 °C whereas the solubility of Au in Fe starts at a temperature of 400 °C [18]. Furthermore, recrystallization and grain growth occurs.

After the heat treatment at 685 °C for 2 h the layer-like microstructure starts to disappear but the columnar growth of the Fe layers is still present (Fig. 1b). After 2 h at 850 °C the microstructure of the films has completely changed. The columnar microstructure of the Fe layers has transformed into isometric grains with sizes ranging from 2 µm to 7 µm (Fig. 1c). EDX measurements performed on the fabricated films indicate an average gold content of about 1.1 ± 0.3 at.%. This result is consistent with the calculated composition of the sputtered bilayers.

The XRD measurements on the sputtered samples are shown in Fig. 2. The diffractograms reveal that the freestanding, as-deposited film is crystalline and shows the (111) Au diffraction peak, as well as the (110) and (200) Fe diffraction peaks. After annealing at 685 °C and 850 °C, respectively for 2 h in a vacuum furnace, the gold peak has decreased in intensity and is shifted from 38.25° to a higher angle of 38.95° (Fig. 2), whereas the Fe (110), and (200) peaks are unchanged. The decrease in the intensity is basically due to the placing of the Fe atoms in the Au lattice and less due to the change of the columnar texture. With regard to the atomic radii of Au (144.2 pm) and Fe (124.1 pm) the lattice plane distance of Au (111) decreases. The lattice parameter for the binary iron–gold compound is $a = 0.400$ nm (pure gold, as deposited $a = 0.407$ nm, literature bulk values are in the range from $a = 0.407$ nm to $a = 0.408$ [21, 22]). Referring to Vegard's law [18] this lattice parameter relates to an Fe content of approximately 15 at.% in the Au-rich phase.

Predominantly gold is segregated at the grain boundaries and just a few precipitates are dispersed within the Fe

Table 1. Sputtering parameters for bilayer-type sputtering technique.

Target Material	Power (W)	Argon flow (sccm)	Pressure (mbar)	Time (s)	Thickness layer (nm)
Fe	600 RF	25	2.3×10^{-3}	3 600	700
Au	200 DC	25	2.3×10^{-3}	10	10

grains. STEM images of the sample annealed at 685 °C show that the Au layers have started to disappear and only some parts of the Au layers remained (Fig. 3a). The accumulation of gold along the iron grain boundary is on the one hand a result of the preferred diffusion along grain boundaries and on the other hand a result of the matching of several similar lattice plane distances of the Au and Fe lattice. Due to the solved Fe atoms in Au, the lattice plane distances of Au are more similar to the Fe lattice plane distances (Table 2) [23, 24]. The segregation of Au along the grain boundaries starts with the formation of precipitates shaped like triangles (Fig. 3b).

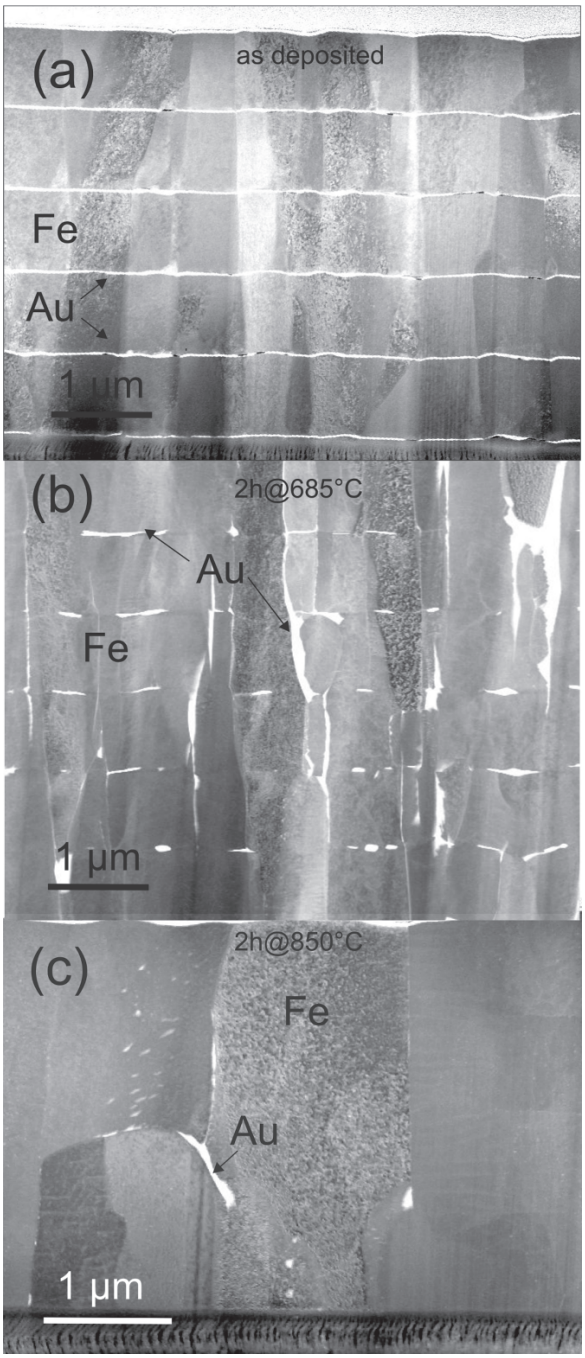

Fig. 1. (a) STEM image of a cross-section of the unannealed, as deposited, Fe–Au multilayer (layer thickness: Fe 700 nm, Au 10 nm). (b) STEM image after annealing for 2 h at 685 °C. (c) STEM image after annealing the multilayer for 2 h at 850 °C.

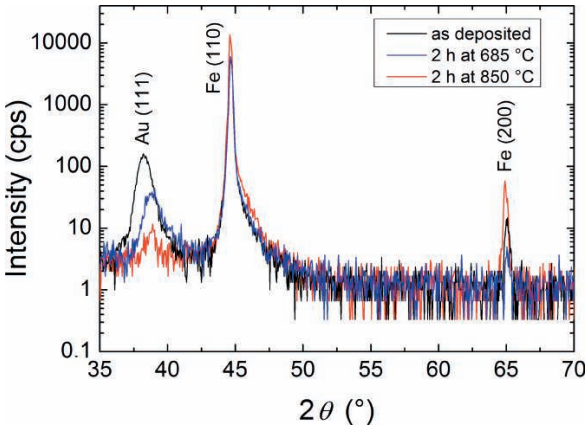

Fig. 2. X-ray diffractogram (logarithmic scale) of the as deposited (black) and the annealed Fe–Au films (blue: 2 h at 685 °C, red: 2 h at 850 °C).

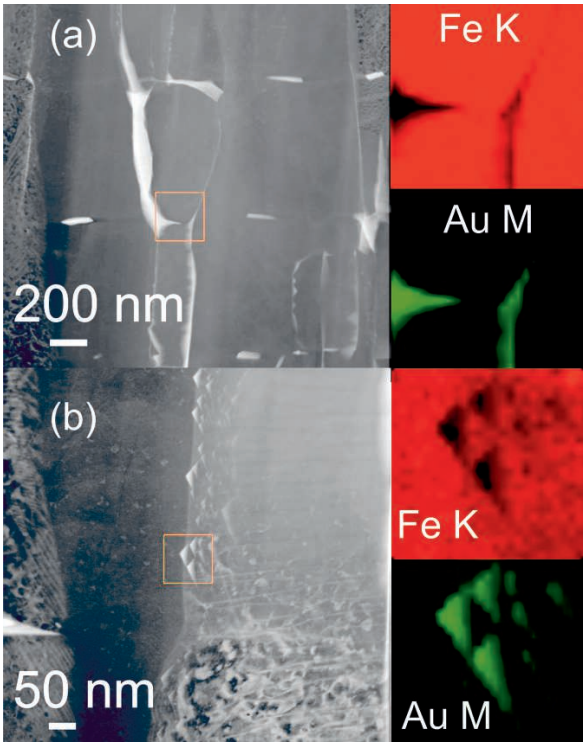

Fig. 3. Cross-section of the sample annealed for 2 h at 685 °C. (a) STEM overview image of a region with gold along the grain boundaries and rudimentary Au layers. The EDX elemental mapping of the area is marked with a square. (b) STEM image of a gold formation shaped like triangles along the iron grain boundary and the associated EDX elemental mapping.

International Journal of Materials Research downloaded from www.hanser-elibrary.com by Hanser Verlag (Office) on February 25, 2015
For personal use only.

Table 2. Lattice plane distances and 2θ angles (Cu-K_α) of Fe and Au [23, 24].

	hkl	*d*-spacing (nm)	2θ (°) with Cu-K_α	*d*-spacing (nm)	2θ (°) with Cu-K_α	*hkl*	
Au	111	0.2354	38.200				
Au	200	0.2039	44.400	0.2027	44.660	110	Fe
Au	220	0.1442	64.600	0.1434	65.000	200	Fe
Au	311	0.1229	77.600				
Au	222	0.1177	81.760	0.1170	82.320	211	Fe

STEM images of the sample annealed at 850 °C (Fig. 4a) reveal that the Au layers have disappeared and in addition to the Au formation along the grain boundaries most of the precipitates appear as nanosized filled tubes. These filled tubes are homogeneously distributed inside the Fe matrix. The STEM image in Fig. 4b shows the magnified area around an irregularly shaped ring-like structure near a gold segregation at a grain boundary. For both areas EDX elemental maps prove that the particles with the bright Z-contrast in the STEM images are composed of Au. The ring-like structure is probably a cross-section of an Au tube. The maps show relative intensities of the EDX signal; i. e. inside the ring structure the map shows no Fe though the corresponding spectrum at this point indicates only less Fe than outside the ring due to the overlay of the constituents.

The heat treatment at 850 °C allows (binary phase diagram [18]) Au atoms to dissolve in the Fe matrix. During cooling to room temperature the solubility of Au in Fe decreases and decomposition occurs. The impurity diffusion of Au in Fe is significantly higher during cooling than the self-diffusion of Fe [22]. For that reason the Au atoms move faster in the Fe matrix. This results due to the Kirkendall effect in the formation of filled hollow shaped precipitates (spheres and tubes). With regard to the solubility of Au in Fe at 850 °C and the assumed decomposition during cooling, Fe is left in the core.

Due to the restricted miscibility, commonly Fe–Au core–shell structures are observed in the shape of isometric spheres of Au with a Fe core [25, 26]. In the majority of cases the synthesis of core–shell Fe–Au nanoparticles takes place by condensation from vapour, synthesis by chemical reaction or solid-state processes such as milling. But it is also known that Au is also able to build rods [27–29]. These nanosized core–shell spheres and rods are usually not observed inside a bulk material. Their formation occurs mostly due to surface wetting.

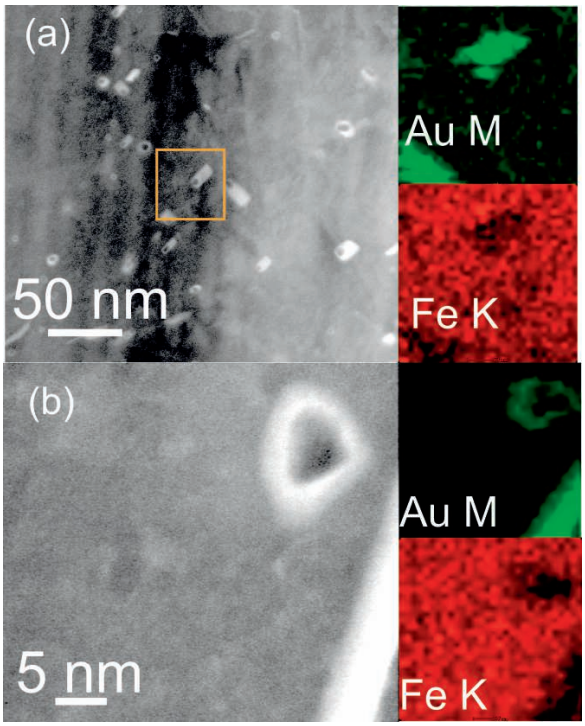

Fig. 4. Cross-section of the sample annealed for 2 h at 850 °C. (a) STEM overview image of a region with gold precipitates and EDX elemental mapping of the area marked with a square overview. (b) STEM image of a ring-like gold structure and the associated EDX elemental mapping.

4. Conclusions

In this paper freestanding Fe–Au thin films have been fabricated by means of a multilayer-like sputtering technique. After annealing for 2 h at 685 °C a two-phase material was generated composed of a homogeneous Fe matrix with segregations of Au along the grain boundaries. XRD measurements showed that the lattice plane distance (*d*-spacing) of the Au (111) and the lattice parameter decreases to 0.4 nm, whereas the lattice parameter of iron is unchanged. This indicates the solubility of Fe atoms in Au. Referring to Vegard's law [18] this lattice parameter relates to an Fe content of approximately 15 at.% in the Au phase. The columnar microstructure of Fe did not change compared to the as-deposited state, whereas the sputtered Au layers have started to vanish and to segregate along the Fe grain boundaries. This is due to the fact that, on the one hand, diffusion along the grain boundaries is preferred and on the other hand, the *d*-spacing of Au (200), (220) and (222) has a good match to the respective Fe (110), (200) and (221) *d*-spacing, and the solved Fe atoms in Au support this match [23, 24]. After annealing for 2 h at 850 °C in addition to the Au segregations along the grain boundaries the Fe matrix has recrystallized and nanosized filled Au tubes appear inside the Fe matrix via solid-state segregation. The heat treatment at 850 °C allows the Au atoms to dissolve in the Fe matrix. During the cooling to room temperature decomposition occurs.

Due to the small size and homogeneous distribution of the filled Au-rich tubes, the degradation of this material should be very uniform. By variation of the sputtering parameters the fabrication of a freestanding Fe film with variable gold content is easy to realize and thus the distribution

International Journal of Materials Research downloaded from www.hanser-elibrary.com by Hanser Verlag (Office) on February 25, 2015
For personal use only.

and dimension of gold-rich segregation could be tailored. For this reason this material could be very interesting for biomedical applications, which require biodegradable materials.

The authors want to thank the DFG for the financial support.

References

[1] R. Erbel, C. Di Mario, J. Bartunek, J. Bonnier, B. de Bruyne, F.R. Eberli, P. Erne, M. Haude, B. Heublein, M. Horrigan, C. Ilsley, D. Böse, J. Koolen, T.F. Lüscher, N. Weissman, R. Waksman: Lancet 369 (2007) 1869–1875. DOI:10.1016/S0140-6736(07)60853-8
[2] M. Moravej, D. Mantovani: Int. J. Mol. Sci. 12 (2011) 4250–4270. DOI:10.3390/ijms12074250
[3] G. Mani, M.D. Feldman, D. Patel, C. Mauli Agrawal: Biomaterials 28 (2007) 1689–1710. DOI:10.1016/j.biomaterials.2006.11.042
[4] B. O'Brien, W. Carroll: Acta Biomater. 5 (2009) 945–958. DOI:10.1016/j.actbio.2008.11.012
[5] H. Hermawan, D. Dubé, D. Mantovani: Acta Biomater. 6 (2010) 1693–1697. DOI:10.1016/j.actbio.2009.10.006
[6] M. Peuster, P. Wohlsein, M. Brügmann, M. Ehlerding, K. Seidler, C. Fink, H. Brauer, A. Fischer, G. Hausdorf: Heart 86 (2001) 563–569. DOI:10.1136/heart.86.5.563
[7] B. Heublein, R. Rohde, V. Kaese, M. Niemeyer, W. Hartung, A. Haverich: Heart 89 (2003) 651–656. DOI:10.1136/heart.89.6.651
[8] M.P. Staiger, A.M. Pietak, J. Huadmai, G. Dias: Biomaterials 27 (2006) 1728–1734. DOI:10.1016/j.biomaterials.2005.10.003
[9] R. Waksman: J. Interv. Cardiol. 19 5 (2006) 414–421. DOI:10.1111/j.1540-8183.2006.00187.x
[10] S. Zhu, N. Huang, L. Xu, Y. Zhang, H. Liu, H. Sun, Y. Leng: Mater. Sci. Eng. C29 (2009) 1589–1592. DOI:10.1016/j.msec.2008.08.037
[11] A. Purnama, H. Hermawan, J. Couet, D. Mantovani: Acta Biomater. 6 (2010) 1800–1807. DOI:10.1016/j.actbio.2010.02.027
[12] M. Peuster, C. Hesse, T. Schloo, C. Fink, P. Beerbaum, C. von Schnakenburg: Biomaterials 27 (2006) 4955–4962. DOI:10.1016/j.biomaterials.2006.05.029
[13] H. Hermawan, D. Dubé, D. Mantovani: Adv. Mater. Res. Vol. 15–17 (2007) 107–112.
[14] M. Schinhammer, A.C. Hänzi, J.F. Löffler, P. Uggowitzer: Acta Biomater. 6 (2006) 1705–1713. DOI:10.1016/j.actbio.2009.07.039
[15] B. Liu, Y.F. Zheng: Acta Biomater. 7 (2011) 1407–1420. DOI:10.1016/j.actbio.2010.11.001
[16] H. Hermawan, A. Purnama, D. Dube, J. Couet, D. Mantovani: Acta Biomater. 6 (2006) 1825–1860.
[17] H. Hermawan, D. Mantovani: Acta Biomater. 9 (2013) 8585–8592. DOI:10.1016/j.actbio.2013.04.027
[18] B. Predel, in: O. Madelung (Ed.) Landolt-Börnstein, Group IV – physical chemistry, Vol 5a, Berlin: Springer-Verlag (1998), 362–365.
[19] C. Borchers, P. Troche, C. Herweg, J. Hoffmann: J. Mater. Sci. 37 (2002) 731–736. DOI:10.1023/A:1013883629605
[20] D. Amram, E. Rabkin: Acta Mater. 61 (2013) 4113–4126. DOI:10.1016/j.actamat.2013.03.038
[21] H. Ebert, J. Abart, J. Voitländer: Z. Phys. Chem. 144 (1985) 223–229. DOI:10.1524/zpch.1985.144.144.223
[22] G. Neumann, C. Tuijn: Self-Diffusion and Impurity Diffusion in Pure Metals: Handbook of Experimental Data, Pergamon imprint of Elsevier, Oxford (2009).
[23] M. Ellner, K. Kolatschek, B. Predel: J. Less-Common Met. (1991) 170, 171–184. DOI:10.1016/0022-5088(91)90062-9
[24] K.H.J. Buschow, P.G. Van Engen, R. Jongebreur: J. Magn. Magn. Mater. 38 (1983) 1–22. DOI:10.1016/0304-8853(83)90097-5
[25] R.G. Chaudhuri, S. Paria: Chem. Rev. 112 (2012) 2373–2433. DOI:10.1021/cr100449n
[26] A. Gautam, F.C.J.M. van Veggel: J. Mater. Chem. B 1 (2013) 5186. DOI:10.1039/c3tb20738b
[27] X. Cai, C.L. Wang, H.H. Chen, C.C. Chien, S.F. Lai, Y.Y. Chen, T.E. Hua, I.M. Kempson, Y. Hwu, C.S. Yang, G. Margaritondo: Nanotechnology 21 (2010) 335604. DOI:10.1088/0957-4484/21/1/015707
[28] Q. Li, Y. Cao: Preparation and Characterization of Gold Nanorods, Nanorods, Orhan Yalcin (Ed.), ISBN: 978-953-51-0209-0, InTech publishing. DOI:10.5772/35880
[29] C.J. Johnson, E. Dujardin, S.A. Davis, C.J. Murphy, S. Mann: J. Mater. Chem. 12 (2002) 1765–1770. DOI:10.1039/b200953f

(Received July 29, 2014; accepted October 6, 2014; online since November 11, 2014)

Correspondence address

Dr. Christiane Zamponi
Faculty of Engineering
Institute for Material Science
Christian-Albrechts-Universität
Kaiserstrasse 2
24143 Kiel
Germany
Tel.: +49 431 880 6213
Fax.: +49 431 880 6203
E-mail: cz@tf.uni-kiel.de

Bibliography
DOI 10.3139/146.111159
Int. J. Mater. Res. (formerly Z. Metallkd.)
106 (2015) 2; page 103–107
© Carl Hanser Verlag GmbH & Co. KG
ISSN 1862-5282

International Journal of Materials Research downloaded from www.hanser-elibrary.com by Hanser Verlag (Office) on February 25, 2015
For personal use only.

6.3 Mechanical Properties and In Vitro Degradation of Sputtered Biodegradable Fe-Au Foils

Own contributions presented in this article:
- Sample preparation
- Measurements
- Evaluation of the data
- Writing of the manuscript

Based on the encouraging results of the previous presented study, in this work the influence of the Au precipitates was studied in order to show that corrosion rate and mechanical properties can be further enhanced by the implementation of Au precipitates.

materials

MDPI

Communication

Mechanical Properties and In Vitro Degradation of Sputtered Biodegradable Fe-Au Foils

Till Jurgeleit *, Eckhard Quandt and Christiane Zamponi

Chair for Inorganic Functional Materials, Institute for Materials Science, Faculty of Engineering, University of Kiel, Kiel 24143, Germany; eq@tf.uni-kiel.de (E.Q.); cz@tf.uni-kiel.de (C.Z.)
* Correspondence: tiju@tf.uni-kiel.de; Tel.: +49-431-880-6299; Fax: +49-431-880-6203

Academic Editor: Arne Berner
Received: 30 September 2016; Accepted: 9 November 2016; Published: 15 November 2016

Abstract: Iron-based materials proved being a viable candidate material for biodegradable implants. Magnetron sputtering combined with UV-lithography offers the possibility to fabricate structured, freestanding foils of iron-based alloys and even composites with non-solvable elements. In order to accelerate the degradation speed and enhance the mechanical properties, the technique was used to fabricate Fe-Au multilayer foils. The foils were annealed after the deposition to form a homogeneous microstructure with fine Au precipitates. The characterization of the mechanical properties was done by uniaxial tensile tests. The degradation behavior was analyzed by electrochemical tests and immersion tests under in vitro conditions. Due to the noble Au precipitates it was possible to achieve high tensile strengths between 550 and 800 MPa depending on the Au content and heat treatment. Furthermore, the Fe-Au foils showed a significantly accelerated corrosion compared to pure iron samples. The high mechanical strength is close to the properties of SS316L steel. In combination with the accelerated degradation rate, sputtered Fe-Au foils showed promising properties for use as iron-based, biodegradable implants.

Keywords: biodegradable; iron; mechanical properties; magnetron sputtering

1. Introduction

The treatment of cardiovascular diseases with permanent implants such as stents is state of the art. However, it was shown that after a certain healing period of three to 12 months [1,2], the vessel has remodeled itself. Afterwards, besides lacking a purpose for the healing, the implant acts as a foreign body which can lead to complications such as late stent restenosis and chronic inflammation reactions. One promising approach is to solve this problem with the use of non-permanent biodegradable implants. Biodegradable implants can consist of all material classes (metals, polymers and ceramics). One of the most important properties is the biocompatibility of the material as well as its degradation products. Furthermore, the material has to keep its mechanical integrity during the healing period and degrade fast enough not to cause the mentioned complications. Therefore, the degradation should be neither too fast nor too slow. The most prominent examples for biodegradable metals are magnesium and iron. While magnesium degrades rather fast and with hydrogen evolution, the in vivo degradation of pure iron was found to be slow but without significant hydrogen evolution [3–6] and thus reduces the risk of complications due to subcutaneous gas accumulations. Therefore, the challenge for iron-based materials is to either accelerate the corrosion rate or improve the mechanical properties insofar as developing thinner structures, and thus less material is sufficient to resist the load acting on the implant. It was shown by Peuster et al. [7,8] that biodegradable iron stents can be implanted into New Zealand rabbits and miniature pigs without observing any complications such as inflammation reactions, neointimal proliferation, or thrombotic events.

In the past different approaches were followed to fulfill these challenges. Moravej et al. [9] showed that due to its microstructure, electroformed iron (E-Fe) shows a higher in vitro corrosion rate compared to cast iron.

In order to enhance the mechanical properties and the degradation performance, also the implementation of noble Pd [10,11], Pt [11], Au and Ag [12,13] were investigated. In the work [13] by Huang et al., they implemented the noble precipitates by using powder metallurgy and spark plasma sintering. These precipitates act as micro-galvanic elements and thus accelerate the degradation rate. Furthermore, it was found that the formation of precipitates increases the compressive strength of the material. Additionally, they demonstrated a sufficient in vitro biocompatibility of Fe-Ag and Fe-Au composites. Due to the poor solubility or even insolubility of Au and Ag in Fe, those Fe composites cannot be produced by conventional cast techniques. Therefore, alternative fabrication techniques are required. In recent years, several studies [14–20] showed that magnetron sputtering technology in combination with structuring techniques used in micro-system technology is suitable to achieve micro-patterned metallic NiTi and Mg devices. In a previous work by the authors [21] it was presented, that the technique is even suitable for the fabrication of patterned pure Fe foils. The devices showed a high strength and a comparable degradation behavior in comparison with pure cast iron [9]. In order to accelerate the degradation speed and further enhance the mechanical properties, in another work [12] the authors investigated the microstructure of sputtered Fe-Au foils. It was shown that by annealing Fe-Au multilayer foils, it is possible to achieve a homogeneous microstructure where the Au exists in the form of finely distributed precipitates in the Fe matrix. In this study, the focus was put on the investigation of the tensile properties and the degradation behavior of such already lithographically micro structured Fe-Au foils, in order to understand how these precipitates influence the material properties. For this purpose, structured Fe-Au foils of various compositions were fabricated and characterized.

2. Experimental Section

2.1. Preparation of Samples

All metal films were deposited in a CS730S cluster magnetron sputtering machine (VON ARDENNE, Dresden, Germany). As working gas Ar was used. For the corrosion measurements quadratic foils of 15 mm edge length and 10 µm thickness were fabricated. A "dog-bone" shaped design with a strut width of 0.5 mm, 7 mm strut length and a homogeneous thickness of 30 µm was used. For the patterning of the foils 4 inch Si wafers were structured by performing UV-lithography and galvanic Cu deposition [16]. The sputtering parameters are given in Table 1.

Table 1. Sputtering parameters.

Element	Power (W)	Pressure (mbar)	Ar Gas Flow (sccm)	Sputtering Rate (nm/s)
Cu	1000 (DC *)	2.3×10^{-3}	25	4.1
Fe	600 (RF #)	2.3×10^{-3}	35	0.6
Au	200 (DC *)	2.3×10^{-3}	35	1.0

* Direct current; # Radio frequency.

Three different multilayer systems in terms of the Au layer thickness were produced. While the thickness of the Fe layers were kept constant 1 µm for all samples, the Au layer thickness was varied in order to fabricate samples with different amounts of Au. The samples are henceforth referred as (FeAu0.3), (FeAu1.0) and (FeAu2.5). The number used in the nomenclature of the samples refers to the average Au content in at %, measured at 10 different spots by EDX (energy dispersive X-ray spectroscopy). All samples were fabricated as reported previously [12]. In order to homogenize the samples they were annealed at 800 °C for two hours. Additional tensile test samples were annealed at

600 °C for two hours, in order to evaluate the mechanical behavior of samples with partially intact multilayer structure.

2.2. Corrosion Measurements

For the determination of the corrosion behavior electrochemical linear polarization measurements and immersion tests were performed. The corrosion tests were performed using stirred Hank's buffered salt solution (H1387 Sigma Aldrich, Taufkirchen, Germany), modified with sodium bicarbonate (0.35 g/L). The temperature of the solution was held constant at 37 ± 1 °C, while the pH was regulated by CO_2 inlet to obtain a value of 7.4 ± 0.05.

Since after the deposition the sample surface exhibited mirror finish quality (R_a = 14 ± 3 nm), no further polishing was necessary. Prior to testing the samples were rinsed with isopropanol and DI-water and fast dried afterwards. A VersaSTAT 3-300 potentiostat connected to a three-electrode cell was used for the electrochemical corrosion tests. The samples were mounted on the sample holder acting as the working electrode (WE) with an exposed area of 0.916 cm^2. As counter electrode (CE) a Pt- mesh and Pt-wire was used. An Ag/AgCl electrode in a 3 molar KCl solution acted as the reference electrode (RE). After determining the corrosion potential U_c in a 4000 s open circuit (OC) measurement the measurement of the I(U) curves was performed. Therefore, the WE was polarized from −400 to +400 mV around U_c with a potential shift rate of 1 mV/s. The Tafel extrapolation method was used to calculate the corrosion rate (CR) from the I(U) curves. For that reason the current was converted into the current density. By fitting the linear regimes of the logarithmically plotted j(U) curve and extrapolation to U_c, the corrosion current density j_c was determined. The corrosion rate was calculated using Equation (1) which is based on Faraday's law [22,23].

$$CR = \frac{j_c M}{n \rho F} \quad (1)$$

Here M is the molar mass of the corroding species, ρ the density, n the number of transferred elementary charges per reaction step and F Faraday constant. Under the assumption based on studies by Zhu et al. [24] on the degradation kinetics of pure-iron in physiological fluids, iron is anodic dissolved as followed $Fe - 2e^- \rightarrow Fe^{2+}$, so that n = 2. With, M = 0.056 kg/mol, ρ = 7874 kg/m^3 and a conversion factor of 31,536, the CR can be calculated in terms of mm/year. For the immersion tests the weight of the samples was determined using a high accuracy balance and afterwards different samples were immersed in 600 mL solution for two, four, six and 12 days. After immersion the corrosion products were carefully removed, the samples were rinsed in isopropanol and fast dried with nitrogen to prevent further oxidation. Afterwards the weight loss was determined. Four different samples of each type were measured. In order to evaluate the microstructure of the samples SEM surface images and EDX elemental mappings were prepared using a scanning electron microscope (Zeiss Ultra Plus, Oberkochen, Germany). Furthermore, sample cross sections were prepared by focused ion beam (FIB) using a Helios NanoLab 600 (FEI). The cross sections were investigated by scanning transmission electron microscopy (STEM) using a F30 G^2 -ST (Tecnai, FEI, Frankfurt, Germany).

2.3. Mechanical Properties

Tensile tests were performed for mechanical characterization using dog-bone-shaped samples with 0.5 mm strut width and 7 mm strut length. The uniaxial tensile tests were performed with a testing machine of the type BETA 5-5/6 × 10 (Messphysik, Fürstenfeld, Austria) with a special sample holder for thin samples. A straining rate of 0.4%/min was applied. For the fracture criterion a force reduction of 60% relative to the maximum applied force was used. For each type four samples were measured to assess the statistic reliability.

Materials **2016**, *9*, 928

3. Results and Discussion

Freestanding pure Fe and Fe-Au multilayer samples were produced by magnetron sputtering. The samples were characterized in terms of their mechanical properties and corrosion behavior. The mechanical properties of the pure Fe samples and different multilayer systems were evaluated from the stress-strain curves measured before and after annealing at 800 °C. The results are shown in the following subsection.

3.1. Mechanical Properties

From the stress-strain curves, the characteristic values of the ultimate tensile strength R_m and the fracture strain were determined for all samples. For each type of sample, the mean values and standard deviations were calculated. The results are shown in Figures 1 and 2. The high initial strength and the decrease of strength and increased ductility of pure Fe samples at higher annealing temperatures were discussed in a previous work [21]. It was found that the as-deposited foils show an energetically unfavorable, defect-rich, columnar and fine-grained structure which is characteristic for sputtered material. During annealing, secondary recrystallization was observed, leading to the reduction of defects and grain coarsening. Compared to the pure Fe samples, the Fe-Au samples show a higher strength and decreased fracture strain scaling with the Au content. While the increased strength scaling with the amount of gold is an expected behavior and is attributed to the size and amount of the Au precipitates, the behavior of the plastic deformation is less obvious. In general, it is expected that plasticity decreases, scaling with the size and the amount of the precipitates and thus the Au content, respectively.

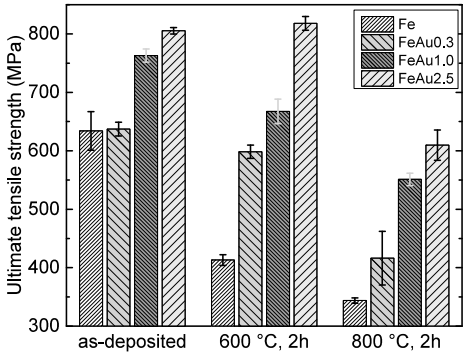

Figure 1. Ultimate tensile strength of the Fe, FeAu0.3, FeAu1.0 and FeAu2.5 samples, before and after different heat treatments.

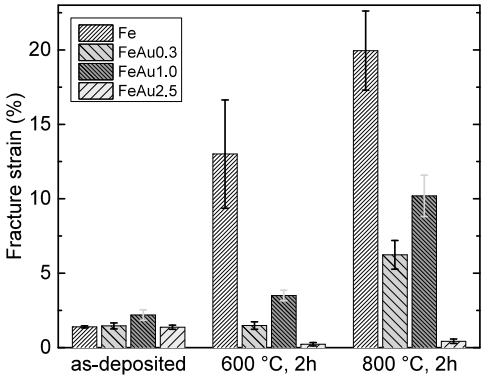

Figure 2. Fracture strain of the Fe, FeAu0.3, FeAu1.0 and FeAu2.5 samples, before and after different heat treatments.

However, the annealed FeAu0.3 samples show a significant lower elongation compared to the FeAu1.0 samples, while the FeAu2.5 samples show, as expected, the lowest value. A possible explanation for the unexpected behavior of the annealed FeAu0.3 samples can be found in the STEM images (Figure 3). While the elemental mappings of the FeAu2.5 and FeAu1.0 samples clearly show Au precipitates, in the elemental mapping of the FeAu0.3 sample no evidence of Au precipitates can be found. The Au signal is statistically distributed over the entire sample. According to the Fe-Au phase diagram, the solubility of Au in Fe at 800 °C is around 1 at % [25]. This suggests that due to the low Au content, the solubility during the annealing is high enough to dissolve the Au in the Fe matrix. With the cooling rate of 0.7 K/s, the diffusion in the sample decreases very fast. As a consequence, the gold atoms are trapped in the lattice, preferably at dislocations and grain boundaries. Due to the nominal Au content of 0.3 at %, low diffusion and homogeneous distribution during annealing, the critical nucleus size necessary for the formation of Au precipitates cannot be reached. Based on the mismatch of the different atomic radii (Fe = 124.1 pm, Au = 144.2 pm), the trapped Au atoms hinder the movement of dislocations and induce internal stresses which lead to a solid solution hardening and reduced plasticity. The decrease of strength at higher annealing temperatures is observed for all samples. The observed behavior is also attributed to the reduction of crystal defects and grain coarsening during annealing. This allows an easier dislocation movement and plastic deformation. It was shown in previous a work [12] that by annealing the multilayer structure (Figure 3a) of Fe-Au, the samples dissolve (Figure 3b–g). Afterwards, two kinds of precipitates exist, one in the grains and the second along grain boundaries (Figure 3b,c). These precipitates act as obstacles for the dislocation movement which enhance the strength while slightly decreasing the ductility of the material. The average grain size of the annealed samples (Table 2) might be an additional reason. All Fe-Au samples exhibit, independent of the Au content, a smaller grain size compared to the annealed pure iron. In agreement with the Hall-Petch relation [26,27] smaller grains will lead to a higher strength. However, since the strength clearly increases with the Au content and the different Fe-Au samples have more or less the same grain size, the precipitation hardening seems to have the major influence. From the results shown in Figures 1 and 2, the FeAu1.0 samples show the best compromise between high strength and ductility. The observed tensile strength of the annealed FeAu1.0 (551 MPa) samples is much higher compared to pure cast iron [9] (205 MPa) and sputtered pure iron (343 MPa). The value even approaches the tensile strength of the SS316L alloy (580 MPa), which is the gold standard for cardiovascular stents [9]. The tensile strength is higher than desired values (300 MPa) by almost a factor of two [28] for biodegradable scaffolds. The elongation, however, comes close to the desired values (15%) [28] but should be further improved by varying the annealing parameters (temperature, time, cooling rate), layer thickness and sequence in order to optimize the size and distribution of the precipitates.

The results of the electrochemical and immersion tests are given in Figures 4 and 5. In Figure 6a, the SEM image and EDX mapping is presented, showing the fine, distributed Au precipitates on the surfaces of a FeAu1.0 and a FeAu2.5 sample annealed at 800 °C for two hours. These samples show a clear difference in the amount of the precipitates even visible in Figure 3b–e, which preferred segregation along the grain boundaries. The difference of the corrosion rate between the as-deposited and the annealed Fe samples found in the electrochemical tests is discussed in a previous work [21] and is related to grain coarsening. However, the acceleration of the degradation rate for the annealed pure Fe was only observed for short immersion times (two days) and lost significance with longer immersion times. Thus, the influence of grain coarsening on the corrosion rate seems to be rather small, and is explained by the easier passive oxide formation on fine-grained surfaces due to an easier diffusion along grain boundaries [29]. Since in a fine-grained structure the grain boundary/grain ratio is higher, the material is able to form a stable passive oxide more efficiently. Both methods show an accelerated corrosion independent from the Au content of the Fe-Au samples compared to the as-deposited Fe samples and even the annealed Fe. While the difference of the degradation rate compared to pure Fe is significant in the electrochemical test as well as in the immersion test, the

Materials **2016**, *9*, 928

influence of different Au contents seems to be less distinct. However, at long immersion times (12 days) an influence of the Au content becomes more pronounced. The results are in good agreement with other studies [11,13] where the corrosion rate of the iron was found to be higher by implementing noble Pd, Pt, Ag and Au precipitates using powder metallurgy.

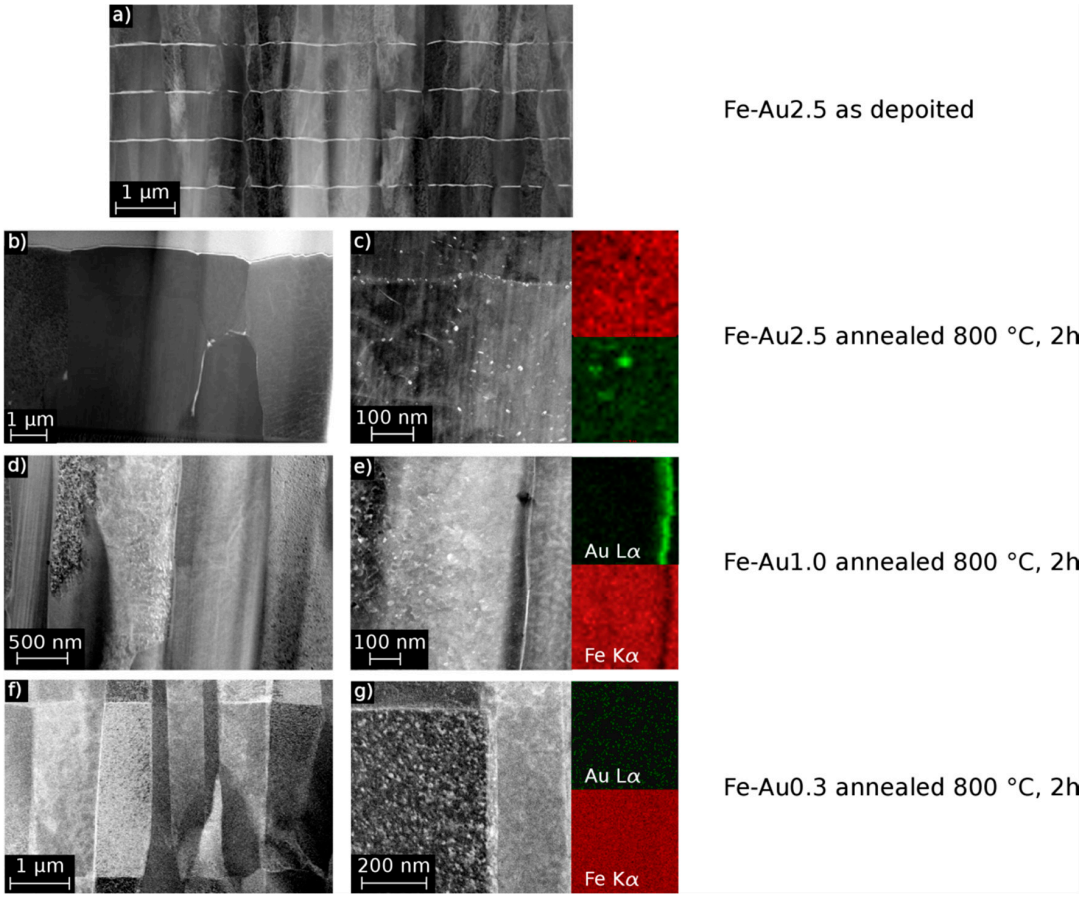

Figure 3. STEM images and EDX Fe-K-α and Au-L-α elemental mappings of Fe-Au sample cross-section, as deposited (**a**) and annealed at 800 °C for two hours (**b**–**g**). In the images Au precipitates appear bright due to the material contrast. (**a**) FeAu2.5 sample as deposited with intact multilayer structure; (**b**) FeAu2.5 sample annealed and (**c**) Fe-Au STEM/EDX mapping of Au precipitates in a grain and along a grain boundary; (**d**) FeAu1.0 sample annealed; the bright Au precipitates are barely visible along the grain boundaries but still resolvable in the EDX mapping (**e**). FeAu0.3 sample annealed (**f**), bright areas along the grain boundaries cannot be identified by EDX mapping (**g**).

Table 2. Average grain size of the different samples annealed at 800 °C, 2 h. The values are determined from SEM surface images.

Sample	Average Grain Size (µm)
Fe [21]	3.01 ± 1.14
FeAu0.3	1.34 ± 0.91
FeAu1.0	1.23 ± 0.82
FeAu2.5	1.25 ± 0.74

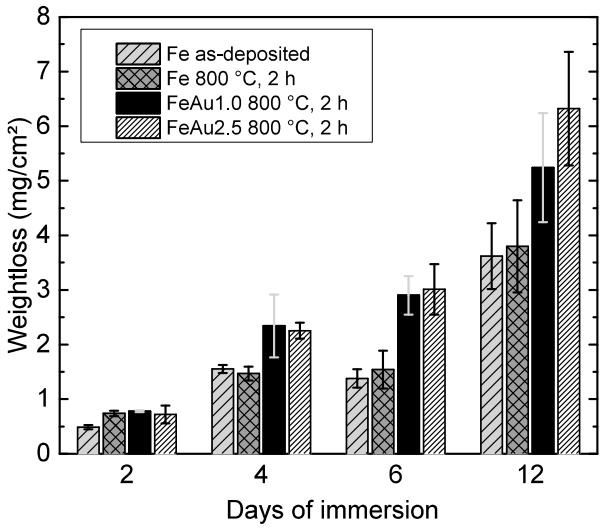

Figure 4. Weight loss of Fe, FeAu0.3, FeAu1.0 and FeAu2.5 samples, after immersion for different times in HBSS (pH 7.4; 37 °C).

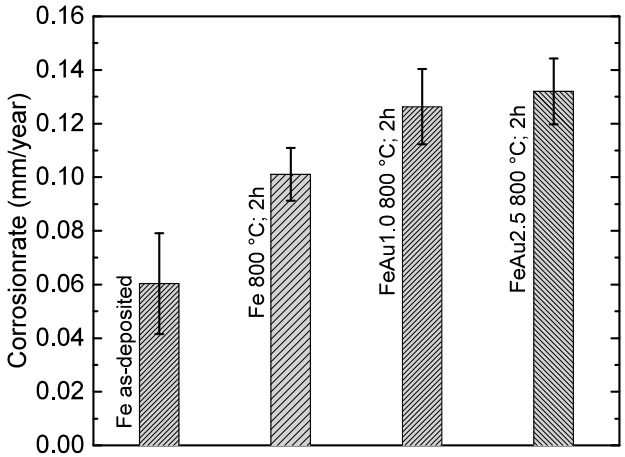

Figure 5. Mean corrosion rate of Fe, FeAu1.0 and FeAu2.5 samples. Using Equation (1), the corrosion rates were calculated from the corrosion current density j_c, determined linear polarization in HBSS (pH 7.4; 37 °C) and Tafel extrapolation method.

3.2. Corrosion Measurements

Au is one of the most noble elements in the galvanic series, and with its high standard potential of ($E^0{}_{\mathrm{Au}}$ = 1.69 V) [30] it is much more noble than iron ($E^0{}_{\mathrm{Fe}}$ = −0.44 V). It is well known [23] that in direct contact with a corroding metal, both metals form an metal- inert metal coupleand hence, a three-phase boundary at the surface (Fe/Au/electrolyte), where the Au acts as a cathode while and the iron as an anode. Thus, the Fe matrix and the Au precipitates form several micro-galvanic elements, leading to an accelerated average corrosion rate of the iron. The faster corrosion rate of the FeAu2.5 samples at 12 days of immersion time is explained by the larger cathode surface. This increased surface area promotes the reduction reaction since the reduction current has to be equal to the anodic current. As a consequence, the anodic metal dissolution has to increase.

However, since the difference of the Au amount and thus the Fe/Au surface ratio (Figure 6) is rather small, the acceleration of the anodic Fe dissolution is only substantial in long-term immersion. The results proved that sputtering of Fe-Au multilayer systems is feasible to implement Au precipitates

which accelerate the corrosion rate compared to the pure reference material. Since the corrosion reaction strongly depends on a number of parameters, e.g., pH value, gas concentrations, electrolyte flow, sample surface, impurity concentrations, cell and protein content of the electrolyte, further research has to show, to what extent the presented concept is valid under in vivo conditions.

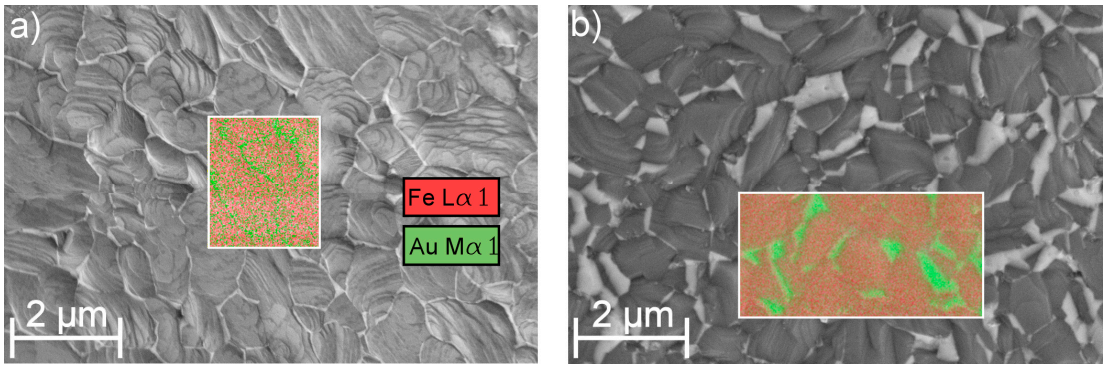

Figure 6. SEM surface image and EDX elemental mappings of the Fe-L-α and Au-M-α lines for (**a**) a FeAu1.0 and (**b**) FeAu2.5 sample annealed at 800 °C, 2 h. In the SEM image Au precipitates appearing bright due to the Z-contrast.

4. Conclusions

It is shown that the previously presented approach [12] of depositing magnetron-sputtered Fe-Au multilayer films and post-deposition heat treatments is feasible to tailor the mechanical properties and accelerate the corrosion speed of iron. While scaling with the Au amount, the strength and degradation speed is increased, the material loses ductility. With regard to the intended use as a biodegradable implant material, the amount of Au should be chosen as small as possible in order to minimize the number of Au particles remaining in the body. Thus, the FeAu1.0 samples showed the best compromise between low Au content, increased strength, sufficient ductility and accelerated degradation rate. However, it is very important to evaluate also the in vivo behavior to understand how the residual Au particles interact with a living organism.

Sputtering allows the fabrication of alreadyfiligree-patterned Fe-Au foil with enhanced mechanical and degradation properties. Due to the very good process control, even the fabrication of devices with a gradient of the precipitation density could be realized. This would allow the fabrication of the ideal biodegradable implant where the outer part degrades initially rather slowly, while the core degrades faster and is able to keep its mechanical integrity longer due to its high strength in the core.

Acknowledgments: Funding via DFG is gratefully acknowledged. Further acknowledgements to Jan Johansen and Bastian Hirsch for supporting this work in the lab.

Author Contributions: Till Jurgeleit performed the experiments and wrote the manuscript; Eckhard Quandt and Christiane Zamponi organized the research.

Conflicts of Interest: The authors declare no conflict of interest.

References

1. Colombo, A.; Karvouni, E. Biodegradable stents "fulfilling the mission and stepping away". *Circulation* **2000**, *102*, 371–373. [CrossRef] [PubMed]
2. Virmani, R.; Farb, A.; Guagliumi, G.; Kolodgie, F.D. Drug-eluting stents: Caution and concerns for long-term outcome. *Coron. Artery Dis.* **2004**, *15*, 313–318. [CrossRef] [PubMed]
3. Staiger, M.P.; Pietak, A.M.; Huadmai, J.; Dias, G. Magnesium and its alloys as orthopedic biomaterials: A review. *Biomaterials* **2006**, *27*, 1728–1734. [CrossRef] [PubMed]

4. Witte, F.; Kaese, V.; Haferkamp, H.; Switzer, E.; Meyer-Lindenberg, A.; Wirth, C.J.; Windhagen, H. In vivo corrosion of four magnesium alloys and the associated bone response. *Biomaterials* **2005**, *26*, 3557–3563. [CrossRef] [PubMed]
5. Witte, F.; Hort, N.; Vogt, C.; Cohen, S.; Kainer, K.U.; Willumeit, R.; Feyerabend, F. Degradable biomaterials based on magnesium corrosion. *Curr. Opin. Solid State Mater. Sci.* **2008**, *12*, 63–72. [CrossRef]
6. Cheng, J.; Liu, B.; Wu, Y.H.; Zheng, Y.F. Comparative in vitro study on pure metals (Fe, Mn, Mg, Zn and W) as biodegradable metals. *J. Mater. Sci. Technol.* **2013**, *29*, 619–627. [CrossRef]
7. Peuster, M.; Wohlsein, M.; Brügmann, M.; Ehlerding, M.; Seidler, K.; Fink, C.; Brauer, H.; Fischer, A.; Hausdorf, G. A novel approach to temporary stenting: Degradable cardiovascular stents produced from corrodible metal–results 6–18 months after implantation into New Zealand white rabbits. *Heart* **2001**, *86*, 563–569. [CrossRef] [PubMed]
8. Peuster, M.; Hessea, C.; Schloo, T.; Fink, C.; Beerbaum, P.; von Schnakenburg, C. Long-term biocompatibility of a corrodible peripheral iron stent in the porcine descending aorta. *Biomaterials* **2006**, *12*, 4955–4962. [CrossRef] [PubMed]
9. Moravej, M.; Prima, F.; Fiset, M.; Mantovani, D. Electroformed iron as new biomaterial for degradable stents: Development process and structure-properties relationship. *Acta Biomater.* **2010**, *6*, 1726–1735. [CrossRef] [PubMed]
10. Schinhammer, M.; Steiger, P.; Moszner, F.; Löffler, J.F.; Uggowitzer, P.J. Degradation performance of biodegradable FeMnC(Pd) alloys. *Mater. Sci. Eng.* **2013**, *33*, 1882–1893. [CrossRef] [PubMed]
11. Huang, T.; Cheng, J.; Zheng, Y.F. In vitro degradation and biocompatibility of Fe-Pd and Fe-Pt composites fabricated by spark plasma sintering. *Mater. Sci. Eng.* **2014**, *35*, 43–53. [CrossRef] [PubMed]
12. Zamponi, C.; Schürmann, U.; Jurgeleit, T.; Kienle, L.; Quandt, E. Microstructures of magnetron sputtered Fe Au thin films. *Int. J. Mater. Res.* **2015**, *106*, 103–107. [CrossRef]
13. Huang, T.; Cheng, J.; Bian, D.; Zheng, Y.F. Fe-au and Fe-Ag composites as candidates for biodegradable stent materials. *J. Biomed. Mater. Res. Part B Appl. Biomater.* **2015**. [CrossRef] [PubMed]
14. Zamponi, C.; Rumpf, H.; Schmutz, C.; Quandt, E. Structuring of sputtered superelastic niti thin films by photolithography and etching. *Mater. Sci. Eng.* **2008**, *481*, 623–625. [CrossRef]
15. Lima de Miranda, R.; Zamponi, C.; Quandt, E. Fabrication of tini thin film stents. *Smart Mater. Struct.* **2009**, *18*, 103–107. [CrossRef]
16. Lima de Miranda, R.; Zamponi, C.; Quandt, E. Micropatterned Freestanding Superelastic TiNi Films. *Adv. Eng. Mater.* **2013**, *15*, 66–69. [CrossRef]
17. Siekmeyer, G.; Schüßler, A.; Lima de Miranda, R.; Quandt, E. Comparison of the fatigue performance of commercially produced nitinol samples versus sputter-deposited nitinol. *J. Mater. Eng. Perform.* **2014**, *23*, 2437–2445. [CrossRef]
18. Schlüter, K.; Shi, Z.; Zamponi, C.; Cao, F.; Quandt, E.; Atrens, A. Corrosion performance and mechanical properties of sputter-deposited MgY and MgGd alloys. *Corros. Sci.* **2010**, *78*, 43–54. [CrossRef]
19. Schlüter, K.; Zamponi, C.; Hort, N.; Kainer, K.U.; Quandt, E. Polycrystalline and amorphous MgZnCa thin films. *Corros. Sci.* **2012**, *63*, 234–238. [CrossRef]
20. Schlüter, K.; Zamponi, C.; Piorra, A.; Quandt, E. Comparison of the corrosion behavior of bulk and thin film magnesium alloys. *Corros. Sci.* **2010**, *52*, 3973–3977. [CrossRef]
21. Jurgeleit, T.; Quandt, E.; Zamponi, C. Magnetron sputtering a new fabrication method of iron based biodegradable implant materials. *Adv. Mater. Sci. Eng.* **2015**, *2015*, 294686. Available online: http://dx.doi.org/10.1155/2015/294686 (accessed on 18 August 2016). [CrossRef]
22. Stern, M.; Geary, A.L. Electrochemical polarization i. a theoretical analysis of the shape of polarization curves. *J. Electrochem. Soc.* **1957**, *104*, 56–63. [CrossRef]
23. Jones, D.A. Electrochemical Kinetics of Corrosion: Polarization Methods to Measure Corrosion Rate. In *Principles and Prevention of Corrosion*, 2nd ed.; Stenquist, B., Kernan, R., Daly, P., Eds.; Pearson-Prentice Hall International: London, UK, 1996; pp. 75–162.
24. Zhu, S.; Huang, N.; Xu, L.; Zhang, Y.; Liu, H.; Sun, H.; Leng, Y. Biocompatibility of pure iron: In vitro assessment of degradation kinetics and cytotoxicity on endothelial cells. *Mater. Sci. Eng.* **2009**, *5*, 1589–1592. [CrossRef]
25. Predel, B.; Madelung, O. (Eds.) *Landolt-Börnstein, Group IV–Physical Chemistry*; Springer: Berlin, Germany, 1998; Volume 5a, pp. 362–365.

26. Hall, E.O. The deformation and ageing of mild steel: II characteristics of the Lüders deformation. *Proc. Phys. Soc. Sect.* **1951**, *64*, 742–747. [CrossRef]
27. Hall, E.O. The deformation and ageing of mild steel: III discussion of results. *Proc. Phys. Soc. Sect.* **1951**, *64*, 747–752. [CrossRef]
28. Heiden, M.; Walker, E.; Stanciu, L. Magnesium, Iron and Zinc Alloys, the Trifecta of Bioresorbable Orthopaedic and Vascular Implantation-A Review. *J. Biotechnol. Biomater.* **2015**, *5*, 1.
29. Ralston, K.D.; Birbilis, N.; Davies, C.H.J. Revealing the relationship between grain size and corrosion rate of metals. *Scr. Mater.* **2010**, *12*, 1201–1204. [CrossRef]
30. Lide, D.R. *CRC Handbook of Chemistry and Physics*, 90th ed.; (Internet Version 2010); CRC PressPress/Taylor and Francis: Boca Raton, FL, USA, 2010.

© 2016 by the authors; licensee MDPI, Basel, Switzerland. This article is an open access article distributed under the terms and conditions of the Creative Commons Attribution (CC-BY) license (http://creativecommons.org/licenses/by/4.0/).

6.4 Magnetron Sputtering as a Fabrication Method for a Biodegradable Fe32Mn Alloy

- Sample preparation
- Measurements
- Evaluation of the data
- Writing of the manuscript

Because sputtered material exhibits particularly a high strength compared to material fabricated by other methods, in this work the previous presented method was adopted to the fabrication of a binary FeMn32 alloy. The reason for the selection of this alloy is that FeMn alloy with high Mn contents seems to exhibit the largest potential in the field of biodegradable Fe based alloys.

materials

MDPI

Article

Magnetron Sputtering as a Fabrication Method for a Biodegradable Fe32Mn Alloy

Till Jurgeleit, Eckhard Quandt and Christiane Zamponi *

Chair for Inorganic Functional Materials, Institute for Materials Science, Faculty of Engineering, University of Kiel, Kaiserstrasse 2, 24143 Kiel, Germany; tiju@tf.uni-kiel.de (T.J.); eq@tf.uni-kiel.de (E.Q.)
* Correspondence: cz@tf.uni-kiel.de; Tel.: +49-431-880-6213

Received: 25 August 2017; Accepted: 11 October 2017; Published: 18 October 2017

Abstract: Biodegradable metals are a topic of great interest and Fe-based materials are prominent examples. The research task is to find a suitable compromise between mechanical, corrosion, and magnetic properties. For this purpose, investigations regarding alternative fabrication processes are important. In the present study, magnetron sputtering technology in combination with UV-lithography was used in order to fabricate freestanding, microstructured Fe32Mn films. To adjust the microstructure and crystalline phase composition with respect to the requirements, the foils were post-deposition annealed under a reducing atmosphere. The microstructure and crystalline phase composition were investigated by scanning electron microscopy, energy dispersive X-ray spectroscopy, and X-ray diffraction. Furthermore, for mechanical characterization, uniaxial tensile tests were performed. The in vitro corrosion rates were determined by electrochemical polarization measurements in pseudo-physiological solution. Additionally, the magnetic properties were measured via vibrating sample magnetometry. The foils showed a fine-grained structure and a tensile strength of 712 MPa, which is approximately a factor of two higher compared to the sputtered pure Fe reference material. The yield strength was observed to be even higher than values reported in literature for alloys with similar composition. Against expectations, the corrosion rates were found to be lower in comparison to pure Fe. Since the annealed foils exist in the austenitic, and antiferromagnetic γ-phase, an additional advantage of the FeMn foils is the low magnetic saturation polarization of 0.003 T, compared to Fe with 1.978 T. This value is even lower compared to the SS 316L steel acting as a gold standard for implants, and thus enhances the MRI compatibility of the material. The study demonstrates that magnetron sputtering in combination with UV-lithography is a new concept for the fabrication of already in situ geometrically structured FeMn-based foils with promising mechanical and magnetic properties.

Keywords: magnetron sputtering; biodegradable metals; FeMn alloys; material characterization

1. Introduction

In the recent years, biodegradable metals have been the subject of intense research. Temporary medical implants such as wires, meshes, screws nails, and stents would be beneficial in order to reduce the risk of late complications such as stent restenosis and chronic inflammation reactions [1]. A biodegradable vascular implant has to keep its mechanical integrity to serve its purpose at least for the entire healing period of 3–12 months [2–4]. Afterwards, the degradation should occur as fast as possible. Several in vivo studies have shown that Fe is a suitable candidate for biodegradable cardiovascular implants. However, the degradation rate of pure Fe was found to be too slow [2,4]. Thus, the degradation rate either has to be accelerated or the mechanical strength has to be increased. A higher strength reduces the required thickness for implant structures to bear the load acting on the implant. As a consequence, even the surface-to-volume ratio is changed. Therefore, a lower corrosion

rate can be compensated by a larger relative surface and thus reduce the time an implant is retained in the body.

For the use as medical implant, the magnetic properties are also of great importance. With respect to MRI investigations, a candidate material should exhibit a low magnetic polarization in order to reduce health risks due to magnetic-induced heating, forces, and torques on the implant. Furthermore, it prevents or reduces image artifacts due to susceptibility effects [5].

In the literature, numerous strategies were presented in order to obtain the desired material properties. Several studies investigated the microstructural influences on the mechanical properties and the degradation behavior of pure Fe. Therefore, different fabrication or metal processing techniques were investigated, such as electroforming (E-Fe) [6,7], magnetron sputtering (S-Fe) [8], rolling techniques [9,10], and equal channel angular pressing (ECAP-Fe) [11–13]. Also, the influence of implementing precipitates, namely Pd [14–17], Au [18–21], Pt [17], Fe_2O_3 particles [22], and carbon nanotubes [23] into the Fe matrix was studied. To enhance the material properties with respect to the requirements, the addition of different alloying elements such as Mn, Co, Al, W, Sn, B, C, and S was investigated [24]. Since Mn was found to show a sufficient biocompatibility and significantly enhance the mechanical properties, many studies focused on different compositions of FeMn alloys [15,25–37]. Even the magnetic properties of FeMn alloys were found to be highly beneficial for the intended use. If the Mn content in the alloy exceeds about 25 at %, the γ-phase becomes predominant, resulting in antiferromagnetic behavior [38,39]. FeMn alloys with an Mn content of 30–35 at % were found to show promising properties in terms of mechanical, magnetic, and corrosion behavior. In order to optimize the material properties, even the research on alternative fabrication methods is reasonable. Recent studies by Zamponi, de Miranda, and Siekmeyer et al. [40–43] showed that magnetron sputtering can be used to fabricate in situ structured and freestanding NiTi foils. Schlüter and Haffner et al. [44–47] demonstrated that this method can be used as well for freestanding, biodegradable Mg-based devices. It was shown that the technique allows the fabrication of scaffold devices with a film thickness up to 250 µm and minimal feature sizes of 5 µm [47].

In a previous work by the authors [8], potential biodegradable pure Fe foils were produced by the same technique. It was found that the foils show high strength due to the fine-grained, columnar crystalline structure. Since the magnetron sputtering technology is not limited to the deposition of pure metals, it can be used as well for the deposition of a wide variety of alloys. In the present study, magnetron sputtering was employed for the deposition of freestanding Fe32Mn (FeMn) foils geometrically structured by means of UV-lithography. The unique microstructure obtained by this technique enables the further enhancement of the mechanical properties. The microstructural properties and composition were investigated by scanning electron microscopy (SEM), X-ray diffraction (XRD), and energy dispersive X-ray spectroscopy (EDX). For the determination of the mechanical values, uniaxial tensile tests were performed. Furthermore, the in vitro degradation rates were measured by electrochemical polarization. Additionally, a vibrating sample magnetometer (VSM) was used in order to determine the magnetic properties of the foils.

2. Materials and Methods

2.1. Sample Preparation

The preparation of the samples was done in a similar way as presented in the authors' previous work [8,20]. An important difference, however, is the choice of the substrate material. In this work, monocrystalline, 4-inch Z-cut quartz wafers (Microchemicals) were used in order to minimize internal stresses arising due to the mismatch of the thermal expansion coefficients—α ($\alpha_{\alpha\text{-Fe}} = 11.8 \times 10^{-6}$ K^{-1} [48]; $\alpha_{\alpha\text{-Mn}} = 21.7 \times 10^{-6}$ K^{-1} [48]; $\alpha_{\gamma\text{-FeMn30}} \approx 18 \times 10^{-6}$ K^{-1} [49]; $\alpha_{Si} = 2.6 \times 10^{-6}$ K^{-1} [48] $\alpha_{\alpha\text{-SiO2}} \perp Z = 13.7 \times 10^{-6}$ K^{-1} [50])—and the elevated substrate temperatures $T_S = 250$ °C.

For the deposition of the in situ structured FeMn foils, the substrates first had to be pre-structured. Therefore, a Cu sacrificial layer was deposited by magnetron sputtering. All sputter depositions were done in a Von Ardenne CS730S cluster magnetron sputtering machine (VON ARDENNE, Dresden, Germany).

After the Cu deposition, the wafers received their final geometric structuring by UV-lithography followed by galvanic copper deposition [42]. For the final deposition, a 4-inch FeMn target (Ingpuls) with a nominal composition of 65 at % Fe, 35 at % and a purity of 99.9%, was used. The deposition parameters were 500 W, 25 sccm Ar flow, and a gas pressure of 2.3×10^{-3} mbar. The given parameters were chosen due to the experience of previous work in order to minimize the residual film stress, and this resulted in a sputter rate of approximately 2 $nm \cdot s^{-1}$. The final geometrical shape of the deposited films is predetermined by the structured substrate. To release these in situ structured films from the substrates, selective wet etching in an alkaline solution containing H_2O, NH_3, and H_2O_2 was done. The sample preparation was finished by annealing at 400 °C, 600 °C (only XRD samples), 800 °C or 950 °C for two hours respectively, in order to adjust the microstructure and the phase composition towards the needs. In order to achieve the desired ductility, the recrystallization temperature has to be reached (>600 °C). Furthermore, non-ferromagnetic behavior is required. Based on the below discussed findings by XRD in this study, only annealing temperatures that showed a significant reduction of α'-phase were considered for the further grain size determination, tensile tests, corrosion tests, and VSM measurements. Mn especially exhibits a very strong affinity to oxygen, thus, in order to prevent oxidation, very low O_2 partial pressures in the range of 10^{-24} mbar [51] are required. Hence, the furnace recipient used for the annealing was first evacuated to a pressure in the 10^{-5} mbar range before annealing. Afterwards, the recipient was purged at 1 bar overpressure with a reducing gas mixture containing 90% and 10% H_2 (VarigonH10®, Linde, Pullach, Germany). Additionally, an O_2/H_2O absorber (Oxisorb®, spectron, Frankfurt, Germany) immediately preceding the gas inlet was used to minimize gas contamination. After annealing, the samples were rapidly cooled down (0.7 °C/s) to room temperature under gas flow for one hour.

For the tensile tests, a "dog-bone" shaped sample design with a strut width of 0.5 mm, 7 mm strut length, 5.5 mm parallel length and a homogeneous thickness of 20 µm, was used. Square shaped samples with an edge length of 15 mm and 10 µm thickness were used for the corrosion and XRD measurements. Therefore, substrates were diced into pieces, followed by the deposition of the sacrificial layer. In order to prevent measurement artifacts due to shape anisotropy in the VSM, circular pieces with a radius of 2 mm were punched out of the 15 mm × 15 mm foils.

2.2. Microstructure

2.2.1. X-ray Diffraction (XRD)

All XRD diffractograms were measured using a XRD-3000 PTS X-ray diffractometer (Seifert, Ahrensburg, Germany), employing monochromatic Cu-Kα radiation. The θ-2 θ-absolute scans were performed in the range of 35° to 90°, with 0.05° step width and 3 s dwell time per step. Square-shaped samples with an edge length of 15 mm were employed.

2.2.2. Electron Microscopy (SEM/EDX)

Surface images of the samples were optically evaluated in order to determine the grain sizes of the different annealing states. To reveal the grains, focused ion beam (FIB) etching was used to prepare the sample surface. Also, the imaging was done using an FIB to get an additional orientation contrast of the grains due to ion channeling effects. Furthermore, images of the fracture area of the tensile test samples were made after the measurement to estimate the fracture behavior. EDX analyses were used to determine the composition of the sputtered foils. To determine the compositional homogeneity, an elemental mapping was done over an entire 4-inch wafer, coated with a 10 µm thick FeMn film.

The measurements were done on a Helios NanoLab 600 (FEI, Frankfurt, Germany) and an EDX detector (Oxford instruments, Abingdon, UK).

2.3. Corrosion

The electrochemical corrosion measurements were performed as previously reported [8], according to the ASTM G59–97 [52]. An electrolyte Hanks buffered salt solution (HBSS) (H1387, Sigma Aldrich, Taufkirchen, Germany) was modified with sodium bicarbonate 0.35 g/L. The pH of the solution was adjusted by CO_2 inlet and held constant at 7.4 $\pm$ 0.05. The I(U) curves were measured using a three-electrode cell and a VersaStat 3 (Princton Applied Research). A Pt mesh was used as the counter electrode, an Ag/AgCl as the reference electrode, and the corrosion samples as the working electrode. The corrosion current density was determined by tafel extrapolation [53,54] in order to calculate the corrosion rates (*CR*) using Equation (1):

$$CR = \frac{j_c M}{n \rho F} \tag{1}$$

where j_c = corrosion current density (Am^{-2}), ρ = density 7690 kg/m^3, M = molar mass 55 g/mol, n = 2 (number of elementary charges per reaction step), and F = Faraday constant. Based on investigations regarding the degradation mechanisms of Fe [55] and FeMn based alloys, [56] the anodic dissolution reaction follows Equations (2) and (3).

$$Fe \rightarrow Fe^{2+} + 2e^- \tag{2}$$

$$Mn \rightarrow Mn^{2+} + 2e^- \tag{3}$$

Since the surface roughness depends predominantly on the substrate roughness, no additional surface treatment was done, and the foils exhibit a mirror finished surface (R_a = 14 nm $\pm$ 3 nm).

In order to determine the mean value and deviation, four samples of each type were measured.

2.4. Mechanical Properties

Uniaxial tensile tests were performed using a BETA 5 $-$ 5/6 $\times$ 10 (Messphysik, Fürstenfeld, Austria) and the above described "dog-bone" shaped tensile test samples. The testing parameters were set to a strain rate of 0.4%/min and 60% force loss relative to the maximum applied force as fracture criterion. Samples annealed at 800 °C and 950 °C for two hours were measured. To express the results in stress, the sample dimensions' strut width was measured by profilometer measurements while the thickness was determined with a dial gauge. Four samples were measured in order to determine the mean values and deviation of the yield strength (YS), ultimate tensile strength (UTS), and fracture strain (A).

2.5. Magnetic Properties

A vibrating sample magnetometer (VSM) of the type Lake Shore 7400 series was used to record magnetic polarization curves in order to determine saturation polarization J_S, remanence J_R, and coercive field H_C. The measurements were performed in-plane in a range of $\pm$0.5 T with a ramping rate of 3 mT s^{-1}.

3. Results

3.1. Microstructure

In Figure 1, XRD diffractograms of freestanding FeMn foils after different heat treatments are shown. The (111) γ-FeMn reflection has the highest intensity. In all samples, even the (200) and (220) reflection corrosponding to the γ-FeMn phase can be found. The (110) reflex of the ferritic α'-phase is

Materials **2017**, *10*, 1196

only present for samples annealed below 800 °C. After annealing at 600 °C, the intensity of the reflex decreases and finally disappears.

Figure 2 displays the SEM surface images used for the optical evaluation of the grain sizes. The images show a shift to larger grain sizes with increasing annealing temperature. Furthermore, the grains become more isometric after annealing, whereas in the as-deposited state numerous small needle shaped grains are also observed. In Figure 3, grain size distributions of as-deposited and annealed FeMn samples are shown. In Table 1, the mean grain size $\bar{d}$, maximum grain size $d_{\max}$, and minimum grain size $d_{\min}$ of as-deposited and annealed FeMn samples are summarized. The as-deposited films show a very fine-grained structure. The majority of the grains exhibit diameters below 500 nm. Whereas just a few grains show diameters >2 µm, several nano-scaled grains d <50 nm are observed. Annealing leads to a shift to larger grain diameters increasing with the temperature. However, even after annealing, a certain amount of grains d < 500 nm is present. Figure 4 displays the elemental distribution of the Fe and the Mn content over an entire 4-inch wafer, measured by EDX. Whereas in the center of the wafer, the composition is homogeneous in an area with a radius of approximately 25 mm (32 at % Mn and 68 at % Fe), in the outer regime, a shift ≈ 1 at % towards higher Mn contents is observed. The small tensile testing, XRD, corrosion, and VSM samples are taken from the center area with homogeneous composition. Furthermore, they are much smaller than the homogeneous region. Therefore, it is assumed that there is no elemental distribution within the single samples.

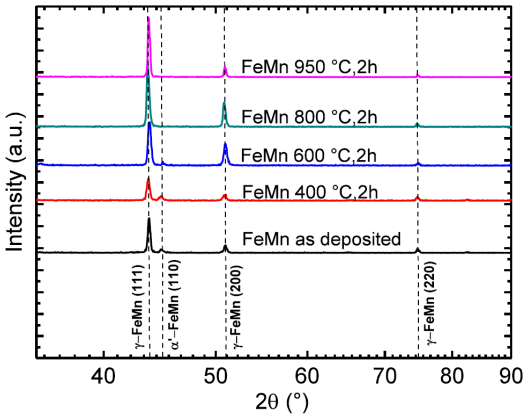

Figure 1. XRD measurements of freestanding FeMn foils as-deposited and after heat treatments at different temperatures for two hours.

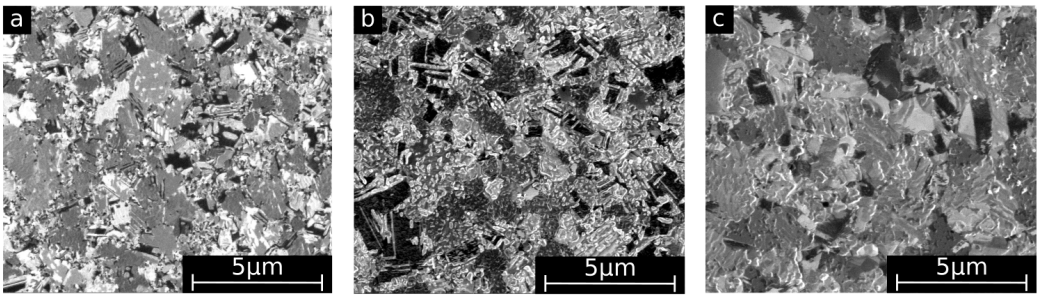

Figure 2. SEM/Focused ion beam (FIB) surface pictures of: (**a**) as-deposited; (**b**) annealed 800 °C for two hours; (**c**) annealed 950 °C for two hours.

Table 1. Mean grain size $\overline{d}$, maximum grain size d_{max}, and minimum grain size d_{min} of as-deposited and annealed FeMn samples.

Sample	$\overline{d}$ (nm)	d_{max} (nm)	d_{min} (nm)
FeMn as-deposited	451	2517	30
FeMn 800 °C, 2 h	965	3193	68
FeMn 950 °C, 2 h	1305	5078	143

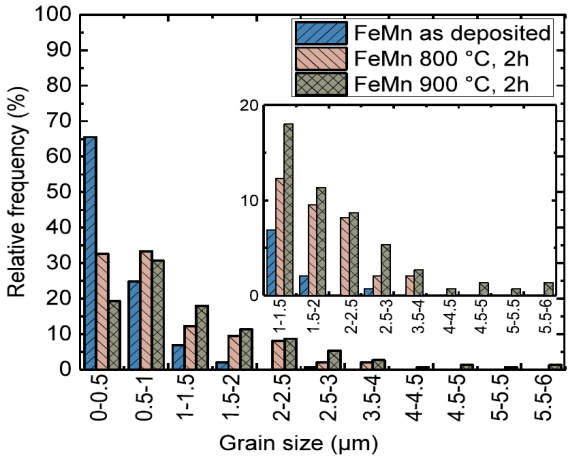

Figure 3. Grain size distribution of as-deposited and annealed FeMn samples.

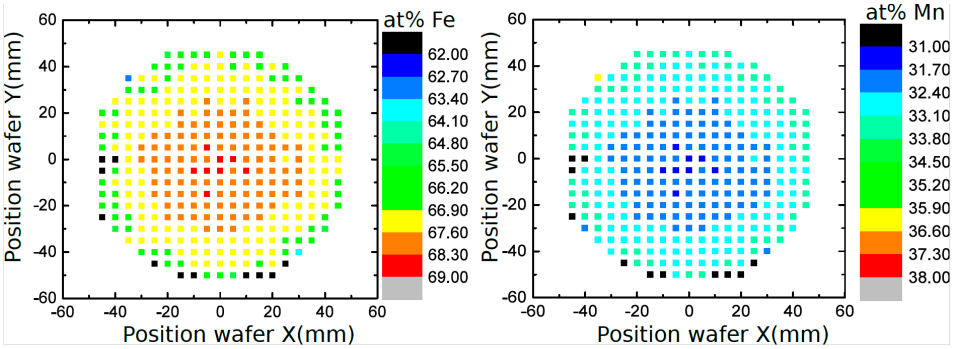

Figure 4. Composition distribution of the Fe and Mn over an entire 4-inch quartz wafer with a FeMn thickness of approximately 10 µm, measured by energy dispersive X-ray spectroscopy (EDX). The material is in the as-deposited state.

3.2. Corrosion

Exemplary measured tafel plots of as-deposited, annealed FeMn, and annealed sputtered pure Fe are shown in Figure 5a. No significant influence on j_c and the corrosion potential U_c between the FeMn samples are observed. In comparison to the pure Fe reference, the j_c values of all FeMn samples are approximately 0.05 Am^{-2} lower. The U_c values of the FeMn samples are approximately 80 mV negatively shifted in comparison to the pure Fe.

The mean values and deviations of the corrosion rates, calculated from the corrosion current densities using Equation (1), are shown in Figure 5b. In addition, a comparison value of the previously presented [8] sputtered pure Fe is shown. The FeMn samples exhibit a corrosion rate by the factor of two lower in comparison to the pure Fe. No significant influence of the heat treatments on the corrosion rates was found.

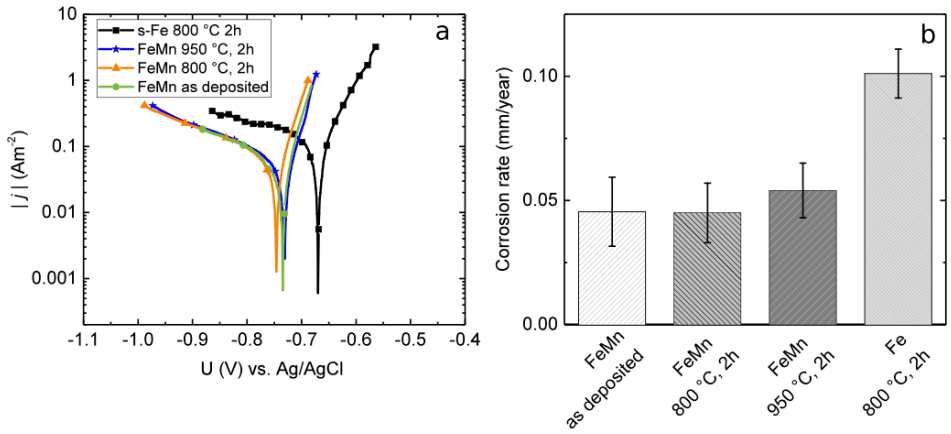

Figure 5. (**a**) Tafel plots of as-deposited, annealed FeMn, and annealed sputtered pure Fe; (**b**) Corrosion rates calculated from electrochemical measurements in Hanks buffered salt solution (HBSS) at 37 °C. For as-deposited and annealed FeMn samples in comparison to previously presented results for annealed pure Fe [8].

3.3. Mechanical Properties

Exemplary stress-strain curves of annealed FeMn samples in comparison to previously presented results for annealed pure Fe are shown in Figure 6. Due to the markedly brittle behavior of the as-deposited samples, most of them were damaged during clamping. Therefore, it was not possible to obtain reliable results for the as-deposited samples. Figure 7a,b show the fracture surface of an as-deposited and an 800 °C annealed FeMn sample after the tensile test. The images show a clear difference in the fracture mode. The fracture area of the as-deposited sample shows columnar splintery areas which are visible in the vertical direction. This is also the growing direction during sputtering. After annealing, a dimple patterned fracture surface with necking is observed. The mean values and deviations of the tensile tests are summarized in Figure 8. Reference values for annealed sputtered pure Fe are given as well. Both the 800 °C and 950 °C annealed FeMn samples show an appreciably higher yield strength (YS) and ultimate tensile strength (UTS) compared to pure Fe. However, the samples annealed at 950 °C show a marginally lower strength. The fracture strain of the FeMn samples is approximately 4% higher than the values for pure Fe and increasing at higher annealing temperatures.

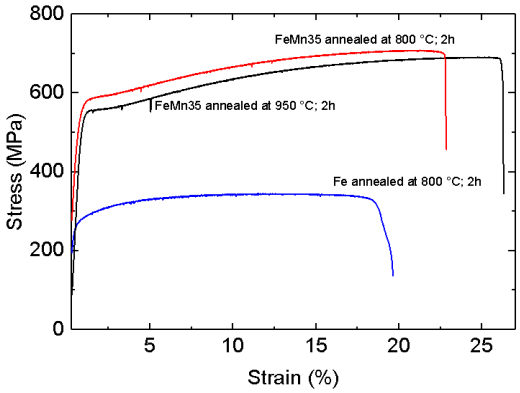

Figure 6. Exemplary stress–strain curves of annealed FeMn samples in comparison to previously presented results for annealed pure Fe [8].

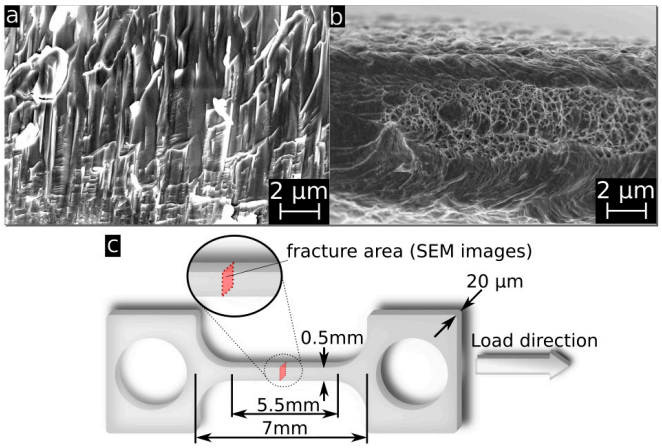

Figure 7. SEM image of the fracture surface of (**a**) as-deposited FeMn sample; (**b**) 800 °C annealed tensile testing sample; and (**c**) schematic drawing of a "dog-bone" shaped tensile testing sample with the relevant sample dimensions and an indication of the perspective of the SEM images.

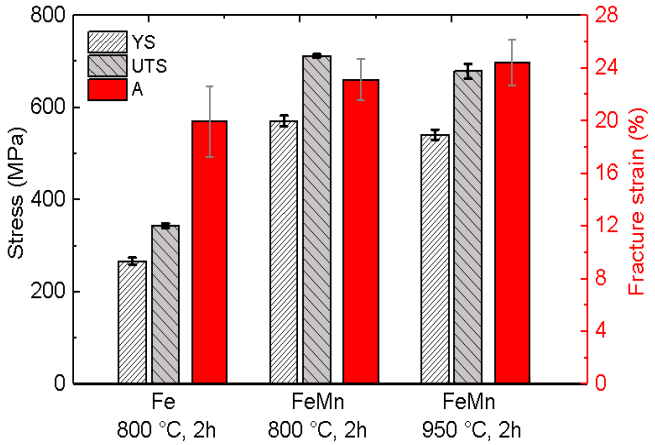

Figure 8. Mean values of the mechanical properties yield strength (YS), ultimate tensile strength (A) and fracture strain (A), of as-deposited and annealed FeMn samples in comparison to previously presented results for annealed pure Fe [8].

3.4. Magnetic Properties

In Figure 9a, magnetic polarization curves of pure Fe in comparison with FeMn are shown for the as-deposited and annealed state. Figure 9b displays the polarization curves of sputtered FeMn as-deposited and in different annealing states compared to a SS 316L reference sample. The J_S, J_R, and H_c values for all samples are summarized in Table 2. Pure Fe, in comparison to FeMn and SS 316L, shows a several orders of magnitude higher magnetic saturation polarization. Whereas the J_S of the as-deposited FeMn is significantly higher compared to SS 316L, an explicit decrease of the polarization is observed for the annealed samples, even noticeable below the value for SS 316L.

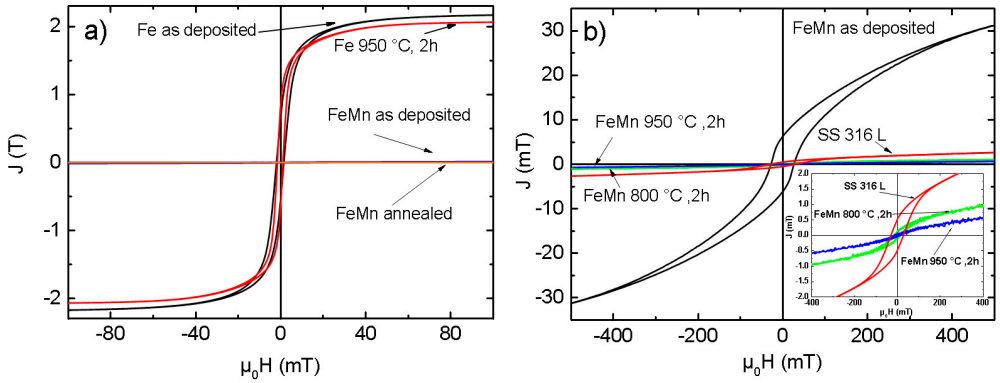

Figure 9. (**a**) Magnetic polarization curves of sputtered Fe and FeMn samples as-deposited and annealed at 950 °C for two hours; (**b**) Magnetic polarization curves of an SS 316L steel reference and sputtered FeMn samples as-deposited and annealed at different temperatures. The inset shows a zoom of the region of interest.

Table 2. Magnetic Properties.

Sample	J_S (T)	J_R (T)	$\mu_0 H_C$ (mT)
Fe as-deposited	2.146	0.823	1.584
Fe 950 °C, 2 h	2.032	0.715	1.147
FeMn as-deposited	0.031	6.21×10^{-3}	26.576
FeMn 800 °C, 2 h	1.09×10^{-3}	0.13×10^{-3}	14.752
FeMn 950 °C, 2 h	0.64×10^{-3}	0.04×10^{-3}	8.586
SS 316L	2.65×10^{-3}	0.51×10^{-3}	30.212

4. Discussion

Magnetron sputtering in combination with UV-lithography is a feasible method to produce freestanding, structured FeMn foils. The grain size measurements (Figures 2 and 3, Table 1) and XRD measurements (Figure 1) indicate a fine-grained microstructure composed of a fcc γ-FeMn phase and a Fe-rich bcc α′-phase. It was found that the phase composition of sputter-deposited films can distinctly differ from the thermodynamic equilibrium (TDE) and strongly depends on the composition [57]. During the deposition process, atoms condense on the substrate and undergo a random walk by diffusion. What type of nuclei and microstructure are formed mainly depends on the ratio of Mn to Fe atoms and substrate temperature T_S. Studies on the dependency of T_S on the microstructure of sputtered films [58,59] showed that increasing T_S results in a microstructure more similar to those grown close to TDE. Thus, the elevated substrate temperature (250 °C) and the high Mn content in the present study result in a favored formation of the fcc γ-FeMn phase. However, both the XRD measurements and the slightly ferromagnetic nature determined by VSM indicate a certain amount of α′-FeMn phase. Since all initially observed reflexes are still present after annealing at 400 °C, there seems to be no significant changes in the crystalline phase composition. However, annealing at 600 °C leads to a reduction of the (110) α′ reflection and an increase of the γ reflections. After annealing at 800 °C and higher temperatures, only γ reflexes are observable. The equilibrium phase diagram of FeMn [60] exhibits an extensive γ region with a solubility for Mn up to 64 at % at 800 °C and 67 at % at 950 °C, respectively. During annealing, the high Mn concentration and increased diffusion processes lead to the stabilization of the γ-phase. The fast cooling after annealing inhibits the retransformation of new α′ grains during cooling. Since the amount of α′-phase is proportional to J_S, it can be concluded that the observed stabilization of the γ-phase after annealing at temperatures above 600 °C is supported by the VSM data (Table 2, Figure 9). As suggested by the XRD investigation, the mean value of J_S of the measured pure Fe (2.089 T) corresponds to 100 vol % ferromagnetic

α′-phase. Furthermore, the low magnetic polarization arising from antiferromagnetic material can be neglected. In this case, the following α′-phase contents are estimated: FeMn as-deposited ≈1.49 vol %, FeMn 800 °C, 2 h ≈ 0.05 vol %, FeMn 950 °C, 2 h ≈ 0.03 vol %.

The observed fine-grained structure is characteristic for sputtered materials (Table 1, Figures 2 and 3). It is known that the film growth at a low ratio of substrate temperature to melting temperature $T_S/T_m < 0.3$ is determined by the surface diffusion. The low surface diffusion hinders adatoms to overcome the roughness or forming nuclei. As a consequence, especially in the grain boundary regions, shadowing effects lead to a fine-grained and very defect rich structure, distinctive for sputtered films at low substrate temperatures [59,61]. Due to the high amount of defects, the movement of dislocations and plastic deformation is strongly limited.

Recrystallization is expected at annealing temperatures above 600 °C, according to the rule of thumb $T_{recrystallization} \approx 0.4\ T_m$ with $T_m \approx 1300$ °C [60]. This is in good agreement with the findings made in this study. Up to 600 °C, there is no evidence for a change in the crystalline phase composition (Figure 1) and thus a recrystallization. At 800 °C, there is a clear change of the crystalline phase composition indicated by XRD. Furthermore, the grain size distribution (Figure 3) shows a clear shift towards higher diameters with increasing annealing temperature. However, after annealing at 950 °C, there is still a very fine-grained structure present with a mean grain size in the lower µm range. Although a significant number of very small grains far below one µm are observed.

The observed brittleness of the as-deposited foils fits to the observed intercrystalline fracture mode (Figure 7a) and supports the assumption of a very defect rich growth, especially in the grain boundaries. A second reason for the initially low ductility is the amount of α′-phase evidenced by XRD. If α′ grains are dispersed in the γ-matrix, they act as further obstacles for dislocation movement and plastic deformation, respectively.

Due to the drastically reduced defect density and predominance of the γ-phase, the annealed material exhibits high strength and concurrently high ductility. Whereas the high UTS has its origin in the intense solid solution hardening, there is also a strain hardening of ≈100 MPa observed in the strain range of 2–15% (Figure 6). The combination of high strength and ductility is characteristic for FeMn alloys with high Mn content. It is either attributed to a strain-induced transformation of the austenitic γ-phase into the martensitic ε-phase (TRIP effect) [62,63], or an intensive formation of strain-induced twins (TWIP effect) [63,64]. Both effects result in high tensile strength and ductility. Due to the composition used in this study, the TWIP effect seems to be more probable. The tensile strength and fracture strain values found in this study are comparable to those found in studies published on FeMn alloys of similar composition [25,31,33,34]. The yield strength is even significantly higher than reported in literature. The high yield strength is attributed to the small grain size in agreement with the Hall–Petch relation [65,66]. Especially the existence of the very small, almost nano-scaled grains enhances the resistance to dislocation movement and, in turn, enhances the yield strength. High yield strength is a very desirable feature since thinner structures are sufficient in order to fulfill the mechanical requirements for an implant.

Besides improving the mechanical properties, it is the goal [25] to control the corrosion rate by alloying Fe with the less noble Mn and U_c to shift to more negative values. A number of studies proved that alloying with Mn leads to an increased degradation rate [25,26,28,31]. However, other studies [24,36,67,68] displayed contradictory results. Especially in vivo, the corrosion rate of FeMn seems to be slower compared to pure Fe. Even the results of the electrochemical corrosion measurements (Figure 5) show distinctly lower j_c and CR values for the FeMn samples in comparison to the previously reported results for sputtered pure Fe. It is difficult to make a meaningful comparison with literature results since there is no standard procedure for the in vitro corrosion tests. Even if, in all works, it is attempted to mimic physiological conditions, there are still significant differences. Besides the used testing solution, the employed buffer system may have a significant influence. In this work, the pH was adjusted to 7.4 by a bicarbonate buffer system which includes a CO_2 inlet. Mouzou et al. [56,69] showed that the type of degradation products of in vitro corrosion measurements

strongly depends on the exact composition of the used electrolyte. Furthermore, they demonstrated that the CO_2 content plays a key role. It was inferred that a CO_2-rich environment favors the formation of Fe/$MnCO_3$ layers. These layers were found to be Mn-rich. Thus, especially Mn-rich alloys under CO_2-rich electrolyte tend to form carbonate passivation layers that hinder the degradation. This is assumed to be the explanation for the low degradation rates found in this study. However, to prove this assumption, further investigations regarding the degradation products are necessary. In comparison to studies that related the corrosion rate to the grain size [10,13], the differences in this study are up to two orders of magnitude smaller. It is inferred that the rather slight differences in the grain sizes are too small to significantly affect the passivation behavior and CR, respectively.

With respect to the application as biodegradable material, the low CR is not necessarily a drawback. Schinhammer et al. showed a decreasing biocompatibility of FeMn alloys with an increasing degradation rate. The effect was related to the increased release of Mn^{2+} ions into the testing medium [70]. Thus, in case of biodegradable FeMn alloys, a lower degradation rate could even be beneficial in terms of the biocompatibility, especially if the lower degradation rate is compensated by a high strength. Overall, the strength exceeds the values reported [31] for the SS 316L gold standard and in general values demanded in literature for biodegradable vascular implants (YS > 200 MPa, UTS > 300 MPa and A > 15–18%) [71]. The high yield strength of the presented material would allow thinner structures. The sample designing via UV-lithography offers great freedom in the device layout, which would allow the fabrication of filigree structured devices with a high relative surface. Therefore, less material would be required and the retention time of the implant could be reduced without increasing the amount of released Mn ions.

5. Conclusions

This study demonstrated that magnetron sputtering in combination with UV-lithography allows the fabrication of in situ structured FeMn foils. Hence, no further forming processes are necessary that might affect the microstructure or the phase composition and thus the material properties. The microstructure and phase composition of the foils are adjusted by heat treatment after the deposition in order to obtain a fine-grained homogeneous microstructure, resulting in a high strength and ductile material. The mechanical properties completely fulfill the requirements for biodegradable implants. The corrosion rate is lower compared to pure Fe. Furthermore, it is shown that the material exhibits an antiferromagnetic character, which is beneficial with respect to MRI compatibility. The saturation polarization is even lower compared to SS 316L used as FDA-approved material for medical implants.

This study opens the field for the further development of sputtered, biodegradable FeMn-based alloys. The method of sputtering allows a large number of further possibilities to enhance the degradation and mechanical properties. Considering the results found in this and the previous work on pure Fe, due to the microstructure of the sputtered material, superior mechanical properties can be expected.

Acknowledgments: Funding via DFG is gratefully acknowledged. Furthermore, Ana María Araújo Cordero and Viktor Schell are acknowledged for supporting this work in the lab.

Author Contributions: Till Jurgeleit performed the experiments and wrote the manuscript; Eckhard Quandt and Christiane Zamponi organized the research.

Conflicts of Interest: The authors declare no conflict of interest.

References

1. Hermawan, H. *Biodegradable Metals*; Springer: Berlin/Heidelberg, Germany, 2012.
2. Peuster, M.; Wohlsein, P.; Brügmann, M.; Ehlerding, M.; Seidler, K.; Fink, C.; Brauer, H.; Fischer, A.; Hausdorf, G. A novel approach to temporary stenting: Degradable cardiovascular stents produced from corrodible metal-results 6–18 months afterimplantation into New Zealand white rabbits. *Heart* **2001**, *86*, 563–569. [CrossRef] [PubMed]

3. Bowen, P.K.; Drelich, J.; Goldman, J. Zinc exhibits ideal physiological corrosion behavior for bioabsorbable stents. *Adv. Mater.* **2013**, *25*, 2577–2582. [CrossRef] [PubMed]
4. Peuster, M.; Hesse, C.; Schloo, T.; Fink, C.; Beerbaum, P.; von Schnakenburg, C. Long-term biocompatibility of a corrodible peripheral iron stent in the porcine descending aorta. *Biomaterials* **2006**, *27*, 4955–4962. [CrossRef] [PubMed]
5. Schenck, J.F. The role of magnetic susceptibility in magnetic resonance imaging: MRI magnetic compatibility of the first and second kinds. *Med. Phys.* **1996**, *23*, 815–850. [CrossRef] [PubMed]
6. Moravej, M.; Prima, F.; Fiset, M.; Mantovani, D. Electroformed iron as new biomaterial for degradable stents: Development process and structure properties relationship. *Acta Biomater.* **2010**, *6*, 1726–1735. [CrossRef] [PubMed]
7. Moravej, M.; Purnama, A.; Fiset, M.; Couet, J.; Mantovani, D. Electroformed pure iron as a new biomaterial for degradable stents: In vitro degradation and preliminary cell viability studies. *Acta Biomater.* **2010**, *6*, 1843–1851. [CrossRef] [PubMed]
8. Jurgeleit, T.; Quandt, E.; Zamponi, C. Magnetron Sputtering a New Fabrication Method of Iron Based Biodegradable Implant Materials. *Adv. Mater. Sci. Eng.* **2015**, *2015*, 294686. [CrossRef]
9. Obayi, C.S.; Tolouei, R.; Paternoster, C.; Turgeon, S.; Okorie, B.A.; Obikwelu, D.O.; Cassar, G.; Buhagiar, J.; Mantovani, D. Influence of cross-rolling on the micro-texture and biodegradation of pure iron as biodegradable material for medical implants. *Acta Biomater.* **2015**, *17*, 68–77. [CrossRef] [PubMed]
10. Obayi, C.S.; Tolouei, R.; Mostavan, A.; Paternoster, C.; Turgeon, S.; Okorie, B.A.; Obikwelu, D.O.; Mantovani, D. Effect of grain sizes on mechanical properties and biodegradation behavior of pure iron for cardiovascular stent application. *Biomatter* **2016**, *6*, e959874. [CrossRef] [PubMed]
11. Xu, X.X.; Nie, F.L.; Zhang, J.X.; Zheng, W.; Zheng, Y.F.; Hu, C.; Yang, G. Corrosion and ion release behavior of ultra-fine grained bulk pure copper fabricated by ECAP in Hanks solution as potential biomaterial for contraception. *Mater. Lett.* **2010**, *64*, 524–527. [CrossRef]
12. Nie, F.L.; Zheng, Y.F.; Wei, S.C.; Hu, C.; Yang, G. In vitro corrosion, cytotoxicity and hemocompatibility of bulk nanocrystalline pure iron. *Biomed. Mater.* **2010**, *5*, 65015. [CrossRef] [PubMed]
13. Nie, F.L.; Zheng, Y.F. Surface chemistry of bulk nanocrystalline pure iron and electrochemistry study in gas-flow physiological saline. *J. Biomed. Mater. Res. B Appl. Biomater.* **2012**, *100*, 1404–1410. [CrossRef] [PubMed]
14. Moszner, F.; Sologubenko, A.S.; Schinhammer, M.; Lerchbacher, C.; Hänzi, A.C.; Leitner, H.; Uggowitzer, P.J.; Löffler, J.F. Precipitation hardening of biodegradable Fe–Mn–Pd alloys. *Acta Mater.* **2011**, *59*, 981–991. [CrossRef]
15. Schinhammer, M.; Steiger, P.; Moszner, F.; Löffler, J.F.; Uggowitzer, P.J. Degradation performance of biodegradable Fe-Mn-C(-Pd) alloys. *Mater. Sci. Eng. C Mater. Biol. Appl.* **2013**, *33*, 1882–1893. [CrossRef] [PubMed]
16. Schinhammer, M.; Pecnik, C.M.; Rechberger, F.; Hänzi, A.C.; Löffler, J.F.; Uggowitzer, P.J. Recrystallization behavior, microstructure evolution and mechanical properties of biodegradable Fe–Mn–C(–Pd) TWIP alloys. *Acta Mater.* **2012**, *60*, 2746–2756. [CrossRef]
17. Huang, T.; Cheng, J.; Zheng, Y.F. In vitro degradation and biocompatibility of Fe-Pd and FE-Pt composites fabricated by spark plasma sintering. *Mater. Sci. Eng. C Mater. Biol. Appl.* **2014**, *35*, 43–53. [CrossRef] [PubMed]
18. Zamponi, C.; Schürmann, U.; Jurgeleit, T.; Kienle, L.; Quandt, E. Microstructures of magnetron sputtered Fe Au thin films. *IJMR* **2015**, *106*, 103–107. [CrossRef]
19. Huang, T.; Cheng, J.; Bian, D.; Zheng, Y. Fe-Au and Fe-Ag composites as candidates for biodegradable stent materials. *J. Biomed. Mater. Res. B Appl. Biomater.* **2016**, *104*, 225–240. [CrossRef] [PubMed]
20. Jurgeleit, T.; Quandt, E.; Zamponi, C. Mechanical Properties and In Vitro Degradation of Sputtered Biodegradable Fe-Au Foils. *Materials* **2016**, *9*, 928. [CrossRef] [PubMed]
21. Cheng, J.; Huang, T.; Zheng, Y.F. Relatively uniform and accelerated degradation of pure iron coated with micro-patterned Au disc arrays. *Mater. Sci. Eng. C Mater. Biol. Appl.* **2015**, *48*, 679–687. [CrossRef] [PubMed]
22. Cheng, J.; Huang, T.; Zheng, Y.F. Microstructure, mechanical property, biodegradation behavior, and biocompatibility of biodegradable Fe-Fe_2O_3 composites. *J. Biomed. Mater. Res. A* **2014**, *102*, 2277–2287. [CrossRef] [PubMed]

23. Cheng, J.; Zheng, Y.F. In vitro study on newly designed biodegradable Fe-X composites (X = W, CNT) prepared by spark plasma sintering. *J. Biomed. Mater. Res. B Appl. Biomater.* **2013**, *101B*, 485–497. [CrossRef] [PubMed]
24. Liu, B.; Zheng, Y.F. Effects of alloying elements (Mn, Co, Al, W, Sn, B, C and S) on biodegradability and in vitro biocompatibility of pure iron. *Acta Biomater.* **2011**, *7*, 1407–1420. [CrossRef] [PubMed]
25. Hermawan, H.; Alamdari, H.; Mantovani, D.; Dubé, D. Iron-manganese. *Powder Met.* **2013**, *51*, 38–45. [CrossRef]
26. Chou, D.-T.; Wells, D.; Hong, D.; Lee, B.; Kuhn, H.; Kumta, P.N. Novel processing of iron-manganese alloy-based biomaterials by inkjet 3-D printing. *Acta Biomater.* **2013**, *9*, 8593–8603. [CrossRef] [PubMed]
27. Hufenbach, J.; Wendrock, H.; Kochta, F.; Kühn, U.; Gebert, A. Novel biodegradable Fe-Mn-C-S alloy with superior mechanical and corrosion properties. *Mater. Lett.* **2017**, *186*, 330–333. [CrossRef]
28. Hermawan, H.; Purnama, A.; Dube, D.; Couet, J.; Mantovani, D. Fe-Mn alloys for metallic biodegradable stents: Degradation and cell viability studies. *Acta Biomater.* **2010**, *6*, 1852–1860. [CrossRef] [PubMed]
29. Hermawan, H.; Mantovani, D. Process of prototyping coronary stents from biodegradable Fe-Mn alloys. *Acta Biomater.* **2013**, *9*, 8585–8592. [CrossRef] [PubMed]
30. Guo, Z.H.; Rong, Y.; Chen, S.; Hsu, T.Y. Deformation Behavior of FeMnSi-Based Shape-Memory Alloys. *Mater. Sci. Forum* **2002**, *394–395*, 427–430. [CrossRef]
31. Hermawan, H.; Dubé, D.; Mantovani, D. Degradable metallic biomaterials: Design and development of Fe-Mn alloys for stents. *J. Biomed. Mater. Res. A* **2010**, *93*, 1–11. [CrossRef] [PubMed]
32. Sing, N.B.; Mostavan, A.; Hamzah, E.; Mantovani, D.; Hermawan, H. Degradation behavior of biodegradable Fe35Mn alloy stents. *J. Biomed. Mater. Res. B Appl. Biomater.* **2015**, *103*, 572–577. [CrossRef] [PubMed]
33. Vojtěch, D.; Kubásek, J.; Čapek, J. Comparative mechanical and corrosion studies on magnesium, zinc and iron alloys as biodegradable metals. *Mater. Tehnol.* **2015**, *49*, 877–882. [CrossRef]
34. Capek, J.; Kubasek, J.; Vojtech, D.; Jablonska, E.; Lipov, J.; Ruml, T. Microstructural, mechanical, corrosion and cytotoxicity characterization of the hot forged FeMn30 (wt. %) alloy. *Mater. Sci. Eng. C Mater. Biol. Appl.* **2016**, *58*, 900–908. [CrossRef] [PubMed]
35. Schinhammer, M.; Hanzi, A.C.; Löffler, J.F.; Uggowitzer, P.J. Design strategy for biodegradable Fe-based alloys for medical applications. *Acta Biomater.* **2010**, *6*, 1705–1713. [CrossRef] [PubMed]
36. Drynda, A.; Hassel, T.; Bach, F.W.; Peuster, M. In vitro and in vivo corrosion properties of new iron-manganese alloys designed for cardiovascular applications. *J. Biomed. Mater. Res. B Appl. Biomater.* **2015**, *103*, 649–660. [CrossRef] [PubMed]
37. Zhang, Q.; Cao, P. Degradable porous Fe-35 wt. %Mn produced via powder sintering from NH_4HCO_3 porogen. *Mater. Chem. Phys.* **2015**, *163*, 394–401. [CrossRef]
38. Endoh, Y.; Ishikawa, Y. Antiferromagnetism of γ Iron Manganes Alloys. *J. Phys. Soc. Jpn.* **1971**, *30*, 1614–1627. [CrossRef]
39. Lee, Y.-K.; Jun, J.-H.; Choi, C.-S. Damping Capacity in Fe-Mn Binary Alloys. *ISIJ Int.* **1997**, *37*, 1023–1030. [CrossRef]
40. Zamponi, C.; Rumpf, H.; Schmutz, C.; Quandt, E. Structuring of sputtered superelastic NiTi thin films by photolithography and etching. *Mater. Sci. Eng. A* **2008**, *481–482*, 623–625. [CrossRef]
41. De Miranda, R.L.; Zamponi, C.; Quandt, E. Fabrication of TiNi thin film stents. *Smart Mater. Struct.* **2009**, *18*, 104010. [CrossRef]
42. De Miranda, R.L.; Zamponi, C.; Quandt, E. Micropatterned Freestanding Superelastic TiNi Films. *Adv. Eng. Mater.* **2013**, *15*, 66–69. [CrossRef]
43. Siekmeyer, G.; Schüßler, A.; de Miranda, R.L.; Quandt, E. Comparison of the Fatigue Performance of Commercially Produced Nitinol Samples versus Sputter-Deposited Nitinol. *J. Mater. Eng. Perform.* **2014**, *23*, 2437–2445. [CrossRef]
44. Schlüter, K.; Zamponi, C.; Piorra, A.; Quandt, E. Comparison of the corrosion behaviour of bulk and thin film magnesium alloys. *Corros. Sci.* **2010**, *52*, 3973–3977. [CrossRef]
45. Schlüter, K.; Zamponi, C.; Hort, N.; Kainer, K.U.; Quandt, E. Polycrystalline and amorphous MgZnCa thin films. *Corros. Sci.* **2012**, *63*, 234–238. [CrossRef]
46. Schlüter, K.; Shi, Z.; Zamponi, C.; Cao, F.; Quandt, E.; Atrens, A. Corrosion performance and mechanical properties of sputter-deposited MgY and MgGd alloys. *Corros. Sci.* **2014**, *78*, 43–54. [CrossRef]

47. Haffner, D.; Zamponi, C.; de Miranda, R.L.; Quandt, E. Micropatterned freestanding magnetron sputtered Mg-alloy scaffolds. *BioNanoMaterials* **2015**, *16*, 19–22. [CrossRef]
48. Lide, D. *Handbook of Chemistry and Physics-crc*, 90th ed.; CRC Press: Boca Raton, FL, USA, 2010.
49. Yasuo, E.; Yasuhisa, N.; Masashi, I. Lattice Dynamics and Invar Properties in f.c.c. FeMn Alloy. *J. Phys. Soc. Jpn.* **1981**, *50*, 469–475.
50. Kushibiki, J.; Takanaga, I.; Nishiyama, S. Accurate measurements of the acoustical physical constants of synthetic/spl alpha/-quartz for SAW devices. *IEEE Trans. Ultrason. Ferroelectr. Freq. Control* **2002**, *49*, 125–135. [CrossRef] [PubMed]
51. Cahn, R.W.; Haasen, P. (Eds.) *Physical Metallurgy*, 4th ed.; North-Holland: Amsterdam, The Netherlands; New York, NY, USA, 1996.
52. American Society for Testing Materials. *Annual Book of ASTM Standards: Metal Test Methods and Analytical Procedures*; Metals—Mechanical Testing; Elevated and Low-Temperature Tests; Metallography. Section 3. Volume 03.01; American Society for Testing Materials: West Conshohocken, PA, USA, 2007.
53. Stern, M.; Geary, A.L. Electrochemical polarization I. A theoretical analysis of the shape of polarization curves. *J. Electrochem. Soc.* **1957**, *104*, 56–63. [CrossRef]
54. Jones, D.A. *Principles and Prevention of Corrosion*, 2nd ed.; Pearson-Prentice Hall: London, UK, 1996.
55. Zhu, S.; Huang, N.; Xu, L.; Zhang, Y.; Liu, H.; Sun, H.; Leng, Y. Biocompatibility of pure iron. *Mater. Sci. Eng. B* **2009**, *29*, 1589–1592. [CrossRef]
56. Mouzou, E.; Paternoster, C.; Tolouei, R.; Chevallier, P.; Biffi, C.A.; Tuissi, A.; Mantovani, D. CO_2-rich atmosphere strongly affects the degradation of Fe-21Mn-1C for biodegradable metallic implants. *Mater. Lett.* **2016**, *181*, 362–366. [CrossRef]
57. Sumiyama, K.; Ohshima, N.; Nakamura, Y. Magnetic Properties of Metastable [alpha]-Mn-Type Mn1 yFey Alloys Produced by Vapor Quenching. *Phys. Status Solidi A* **1986**, *98*, 229–238. [CrossRef]
58. Thornton, J.A. The microstructure of sputter-deposited coatings. *J. Vac. Sci. Technol. A* **1986**, *4*, 3059. [CrossRef]
59. Thornton, J.A. High Rate Thick Film Growth. *Annu. Rev. Mater. Sci.* **1977**, *7*, 239–260. [CrossRef]
60. Von Goldbeck, O.K. *IRON—Binary Phase Diagrams*, 1st ed.; Springer-Verlag: Berlin/Heidelberg, Germany, 1982.
61. Bunshah, R.F. 3.1 mechanical properties of PVD films. *Vacuum* **1977**, *27*, 353–362. [CrossRef]
62. Fischer, F.D.; Reisner, G.; Werner, E.; Tanaka, K.; Cailletaud, G.; Antretter, T. A new view on transformation induced plasticity (TRIP). *Int. J. Plast.* **2000**, *16*, 723–748. [CrossRef]
63. Grässel, O.; Krüger, L.; Frommeyer, G.; Meyer, L. High strength Fe–Mn–(Al, Si) TRIP/TWIP steels development—Properties—Application. *Int. J. Plast.* **2000**, *16*, 1391–1409. [CrossRef]
64. Neu, R.W. Performance and Characterization of TWIP Steels for Automotive Applications. *Mater. Perform. Charact.* **2013**, *2*, 20130009. [CrossRef]
65. Hall, E.O. The Deformation and Ageing of Mild Steel: III Discussion of Results. *Proc. Phys. Soc. Sect. B* **1951**, *64*, 747–752. [CrossRef]
66. Petch, N.J. XVI. The ductile fracture of polycrystalline α-iron. *Philos. Mag.* **1956**, *1*, 186–190. [CrossRef]
67. Liu, B.; Zheng, Y.F.; Ruan, L. In vitro investigation of Fe30Mn6Si shape memory alloy as potential biodegradable metallic material. *Mater. Lett.* **2011**, *65*, 540–543. [CrossRef]
68. Hermawan, H.; Dube, D.; Mantovani, D. Developments in metallic biodegradable stents. *Acta Biomater.* **2010**, *6*, 1693–1697. [CrossRef] [PubMed]
69. Mouzou, E.; Paternoster, C.; Tolouei, R.; Purnama, A.; Chevallier, P.; Dube, D.; Prima, F.; Mantovani, D. In vitro degradation behavior of Fe-20 Mn-1.2C alloy in three different pseudo-physiological solutions. *Mater. Sci. Eng. C Mater. Biol. Appl.* **2016**, *61*, 564–573. [CrossRef] [PubMed]
70. Schinhammer, M.; Gerber, I.; Hanzi, A.C.; Uggowitzer, P.J. On the cytocompatibility of biodegradable Fe-based alloys. *Mater. Sci. Eng. C Mater. Biol. Appl.* **2013**, *33*, 782–789. [CrossRef] [PubMed]
71. Michael, M.; Walker, E.; Stanciu, L. Magnesium, Iron and Zinc Alloys, the Trifecta of Bioresorbable Orthopaedic and Vascular Implantation—A Review. *J. Biotechnol. Biomater.* **2015**, *5*, 185–193.

© 2017 by the authors. Licensee MDPI, Basel, Switzerland. This article is an open access article distributed under the terms and conditions of the Creative Commons Attribution (CC BY) license (http://creativecommons.org/licenses/by/4.0/).

6.5 Magnetron-Sputtered, Biodegradable FeMn Foils: The Influence of Manganese Content on Microstructure, Mechanical, Corrosion, and Magnetic Properties

- Guiding sample preparation and measurements
- Partially sample preparation
- Partially Measurements
- Evaluation of the data
- Writing of the manuscript

As stated in chapter 4 one criterion for FeMn alloys is to keep the Mn content as low as possible and as high as necessarry in order to exploit its full potential. The main motive for this work was the determination of this critical Mn content which was hitherto specified with 20 % Mn by Hermawan et al. [HDM08], but can be expected at lower Mn contents according to the phase diagram Fig. 3.0.5. Furthermore, it was the goal to study the influence of different Mn contents on the material properties of sputtered material.

materials

MDPI

Article

Magnetron-Sputtered, Biodegradable FeMn Foils: The Influence of Manganese Content on Microstructure, Mechanical, Corrosion, and Magnetic Properties

Till Jurgeleit *, Lea Katharina Jessen, Eckhard Quandt and Christiane Zamponi *

Institute for Materials Science, Faculty of Engineering, University of Kiel, Kaiserstrasse 2, 24143 Kiel, Germany; leje@tf.uni-kiel.de (L.K.J.); eq@tf.uni-kiel.de (E.Q.)

* Correspondence: tiju@tf.uni-kiel.de (T.J.); cz@tf.uni-kiel.de (C.Z.); Tel.: +49-431-880-6213 (C.Z.)

Received: 6 March 2018; Accepted: 20 March 2018; Published: 23 March 2018

Abstract: FeMn alloys show a great potential for the use as a biodegradable material for medical vascular implants. To optimize the material properties, with respect to the intended application, new fabrication methods also have to be investigated. In this work different Fe–FeMn32 multilayer films were deposited by magnetron sputtering. The deposition was done on a substrate structured by UV lithography. This technique allows the fabrication of in-situ structured foils. In order to investigate the influence of the Mn content on the material properties foils with an overall Mn content of 5, 10, 15, and 17 wt % were fabricated. The freestanding foils were annealed post-deposition, in order to homogenize them and adjust the material properties. The material was characterized in terms of microstructure, corrosion, mechanical, and magnetic properties using X-ray diffraction, electron microscopy, electrochemical polarization, immersion tests, uniaxial tensile tests, and vibrating sample magnetometry. Due to the unique microstructure that can be achieved by the fabrication via magnetron sputtering, the annealed foils showed a high mechanical yield strength (686–926 MPa) and tensile strength (712–1147 MPa). Owing the stabilization of the non-ferromagnetic ε- and γ-phase, it was shown that even Mn concentrations of 15–17 wt % are sufficient to distinctly enhance the magnetic resonance imaging (MRI) compatibility of FeMn alloys.

Keywords: magnetron sputtering; biodegradable metals; FeMn alloys; material characterization; mechanical properties; corrosion properties; magnetic properties

1. Introduction

Biodegradable metallic materials for the intended use as temporary implants (e.g., stents) are a topic of intense research. One of the most prominent material classes are iron-based materials. In early in vivo studies by Peuster et al. [1,2], it was shown that the general feasibility of Fe as a biodegradable material, with regards to its biocompatibility, is given. However, with respect to the desired degradation time of 6–12 months, the degradation rate of pure Fe was found to be too slow. Therefore, from the material science point of view, the goal is to increase the corrosion rate of the material. Another possible strategy is to enhance its strength, to the extent that thinner structures bear the load acting on an implant and relativize the low corrosion rate. A further drawback are the ferromagnetic (FM) properties of Fe, which can cause complications during magnetic resonance imaging (MRI), such as implant heating, torque, or image distortions due to susceptibility effects [3]. One strategy to obtain the desired material properties is alloying. One of the most promising alloying elements is Mn. Alike Fe, Mn is an essential trace element in the human metabolism [4]. Furthermore, FeMn alloys are known for their good mechanical properties. Since Mn exhibits a lower standard

potential than Fe [5], the overall corrosion potential of the FeMn alloy is in turn shifted to lower values, and the alloy should be more prone to corrosion. Additionally, FeMn alloys with high Mn concentrations of 15–35 wt % are known for their high strength and even ductility. This is attributed to the two effects called transformation induced plasticity (TRIP) and twinning induced plasticity (TWIP) [6]. An additional advantage of those highly-alloyed FeMn alloys are the magnetic properties. FeMn alloys exist in three crystal modifications: the α'-, ε-, and γ-phases. While the FM α'-phase occurs at rather low Mn concentrations, the ε- and γ-phase are stable at higher Mn concentrations [7]. It was found that the ε-phase exhibits paramagnetic (PM) behavior, whereas the γ-phase shows antiferromagnetic (AFM) behavior [8,9], and thus is beneficial for biodegradable implant applications. Hermawan et al. first investigated FeMn alloys with 20, 25, 30, and 35 wt % Mn content. The alloys showed significantly higher strength and corrosion rates compared to pure iron. All the investigated alloys showed AFM behavior with an saturation magnetization below those of the stainless steel 316 L (SS 316 L), which acts as a gold standard for medical implants [10,11].

In previous works of the authors, it was shown that magnetron sputtering is a feasible method for fabricating freestanding micro-patterned devices for degradable implants. A high strength was observed, due to the unique microstructure achieved by this technique [12–15]. The usage of magnetron sputtering in combination of UV lithography for the fabrication of NiTi devices for medical applications was first shown by Zamponi, Siekmeyer, and de Miranda et al. [16–19]. Furthermore, the method was adapted by Schlüter and Haffner et al. for the fabrication of biodegradable Mg-based devices with feature sizes down to 5 µm [20–23]. In other work, the technique was used for the fabrication of biodegradable FeMn foils. It was found that due to the microstructure, the foils show a higher strength compared to the values of FeMn alloys with comparable compositions presented in literature. Furthermore, the saturation magnetization of the annealed foils was found to be lower compared to a SS 316 L reference [15].

Because there are worries about Mn toxicity, the daily dose should not exceed 500 µg/day [4,24,25]. Even though it is almost impossible to reach this limit with a vascular stent that degrades over 6–12 months, the Mn content should be as small as possible, but as high as necessary. Considering the non-equilibrium phase diagram for FeMn [26,27], the desired phase composition that only contains the ε- and γ-phase, and thus non-ferromagnetic behavior, can be expected at significantly lower Mn concentrations than the 20 wt % Mn reported by Hermawan [10]. Hence, in this study, the influence of different Mn concentrations (5, 10, 15, and 17 wt %) on the microstructure—and in turn the magnetic properties, mechanical behavior, and corrosion—was investigated. In order to achieve the desired composition, the foils were fabricated by sputtering Fe-FeMn32 multilayers (ML), followed by a heat treatment for homogenization. The magnetic characterization was done via vibrating sample magnetometry (VSM). Electrochemical polarization measurements and immersion tests were performed in order to evaluate the corrosion rates under in vitro conditions. The mechanical properties were determined by uniaxial tensile tests. The microstructural characterizations were done via X-ray diffraction (XRD), scanning electron microscopy (SEM), energy-dispersive X-ray spectroscopy (EDX), and focused ion beam (FIB) analysis.

2. Materials and Methods

2.1. Sample Preparation

All sputter depositions in this work were done in a Von Ardenne CS730S (VON ARDENNE, Dresden, Germany) cluster magnetron sputtering machine. Crystalline, Z-cut, quartz wafers with 10 cm diameter were used as substrate material. Three different sample designs were used. Square shaped foils (15 mm $\times$ 15 mm) with a thickness of 10 µm were used for the corrosion tests and XRD measurements. For the tensile tests, "dog-bone" shaped samples with a strut width of 0.5 mm, 7 mm strut length, and a homogeneous thickness of 20 µm were used. The VSM measurements were performed on circular-shaped foils with a radius of 1 mm and 20 µm thickness. For more details about

the structuring process, refer to previous work [12,14,15]. As sputter targets, a pure Fe plate with (20 cm diameter) (FHR, Ottendorf-Okrilla, Germany) and a Fe35Mn plate (10 cm diameter) (Ingpuls, Bochum, Germany) were used, both with a purity of 99.9%. All foils were deposited as multilayers, where the first and last layer was a Fe layer. A schematic drawing of a multilayer stack is shown in Figure 1. The Fe layer thickness was kept constant at 250 nm, whereas the Fe35Mn layer thickness varied between 50–280 nm. In this way, batches of different overall Mn concentrations (5, 10, 15, and 17 wt %) were fabricated. In the following, the different samples are named FeMnX. Here, X stands for the mean, overall Mn content ± 0.5 wt % in the foils determined by EDX, after the homogenization step explained below. Table 1 displays an overview of the sample names, corresponding desired Mn layer thickness, and the measured nominal Mn content. The multilayer stacks were released from the substrate by selective chemical wet etching of the sacrificial layer. In order to homogenize the foils and reduce the defect density, the samples were annealed. Based on the experience of previous work, samples were annealed at 800 °C and 950 °C for two hours. In order to prevent oxidation, the heat treatments were performed under a reducing atmosphere (Varigon H10®, Linde, Pullach, Germany), as described previously [15].

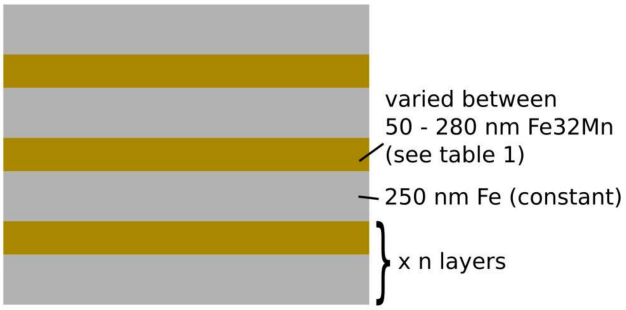

Figure 1. Schematic drawing of Fe–FeMn32 multilayer stack.

Table 1. Sample parameters.

Sample	Target (s)	FeMn32 Thickness (nm)	Nominal Mn Content (wt %)
Fe [12]	pure Fe	-	0.0
FeMn5	Fe-FeMn35 multilayer	50	4.8
FeMn10	Fe-FeMn35 multilayer	125	10.0
FeMn15	Fe-FeMn35 multilayer	250	15.5
FeMn17	Fe-FeMn35 multilayer	325	17.2
FeMn32 [15]	Pre-alloyed FeMn35	-	32

Fe layer thickness constant (250 nm) for all ML samples.

2.2. Microstructure

2.2.1. X-ray Diffraction

The identification of the crystallographic phases were done using an X-ray diffractometer XRD-3000 PTS (Seifert, Ahrensburg, Germany), employing monochromatic Cu-Kα radiation. The θ–2θ absolute scans were performed in the range of 35° to 90°, with 0.05° step width and 3 s dwell time per step.

2.2.2. Scanning Electron Microscopy/Energy-Dispersive X-ray Spectroscopy

Further investigations regarding the composition and microstructure were done by EDX and SEM. For the investigations of the composition, an SEM (Zeiss Ultra Plus, Oberkochen, Germany) associated with an EDX detector (Oxford instruments, Abingdon, UK) was used. Cross-sectional SEM images

were prepared by FIB NanoLab 600 (FEI, Frankfurt, Germany) to obtain the grain structure. In order to reveal the grains, ion beam excitation was used for the images, to give an additional orientation contrast due to channeling effects. The grain size was optically measured.

2.3. Corrosion

2.3.1. Electrochemical Polarization Measurements

Electrochemical, linear polarization corrosion measurements were performed as previously reported [12], according to the ASTM G59-97 [28]. As electrolyte, Hanks' buffered salt solution (HBSS) (H1387 Sigma Aldrich, Taufkirchen, Germany) was modified with sodium bicarbonate at 0.35 g/L. The temperature of the solution was held constant at 37 ± 1 °C, and the pH was adjusted by CO_2 inlet and regulated to 7.4 ± 0.05. The polarization curves were measured using a three-electrode cell and a VersaStat 3 (Princton Applied Research, Oak Ridge, TN, USA). A Pt mesh as counter electrode, an Ag/AgCl reference electrode, and the corrosion samples as working electrodes were used. The corrosion current density rates were determined by Tafel extrapolation [29,30], in order to calculate the corrosion rates (CR) using (Equation (1)):

$$CR = \frac{j_c M}{n \rho F} \tag{1}$$

where j_c is the corrosion current density (A/m^2), ρ is the density (7690 kg/m^3), M is the molar mass (55 g/mol), n is the number of elementary charges per reaction step (2), and F is the Faraday constant. Based on investigations regarding the degradation mechanisms of Fe [31] and FeMn-based alloys [32], the anodic dissolution reaction follows (Equations (2) and (3)).

In order to determine the mean value and deviation, four samples of each type were measured.

$$Fe \rightarrow Fe^{2+} + 2e^- \tag{2}$$

$$Mn \rightarrow Mn^{2+} + 2e^- \tag{3}$$

2.3.2. Immersion Tests

Additionally, immersion tests were performed to determine the weight loss. The test conditions were the same as described above. Before the tests, the weight of the samples was determined using a high accuracy balance, and samples were cleaned in isopropanol. All samples were immersed in 600 mL HBSS for 12 days. After the immersion period, the samples were washed in de-ionized (DI) water, and residual corrosion products were carefully removed by dipping them into diluted H_3PO_4 for 20 s. Next, the samples were carefully rinsed in DI water and isopropanol, and fast-dried with nitrogen. Finally, the weight loss (WL) was determined. Four samples of each type were measured.

2.4. Mechanical Properties

Uniaxial tensile tests were performed using the above described "dog-bone" shaped samples and a testing machine of the type BETA 5-5/6 × 10 (Messphysik, Fürstenfeld, Austria), with a special sample holder for thin samples. A straining rate of 0.4%/min was applied. For the fracture criterion, a force reduction of 60% relative to the maximum applied force was used. For each type, four samples were measured to assess the statistic reliability. Since for the desired application exclusively the annealed samples are of interest, no as-deposited samples were tested.

2.5. Magnetic Properties

A vibrating sample magnetometer (VSM) of the type Lake Shore 7400 series (Lake Shore, Darmstadt, Germany) was used to record magnetic polarization curves, in order to determine

saturation polarization J_S, remanence J_R, and coercive field H_C. The measurements were performed in-plane, with a range of ± 0.5 T and with a ramping rate of 3 mT/s.

3. Results

3.1. Microstructure

3.1.1. X-ray Diffraction

In Figure 2, the XRD measurements of different FeMnX samples in the as-deposited and annealed state are shown. The measured reflexes are indexed by a Greek letter and a number, respectively. The letter refers to the phase type, and the number to the corresponding lattice plane. The indexes, and their corresponding 2θ values and lattice planes, are shown in Table 2. All as-deposited samples showed reflexes of the α'- and γ-phase. Furthermore, additional reflexes of the ε-phase and the α-Mn phase were observed in the samples with higher Mn concentrations (5–17 wt %). The annealed FeMn5 samples showed an increase of the intensity of the α'-phase reflexes. After annealing at 800 °C, reflexes of the γ- and ε-phase were also present. Only reflexes of the α'-phase were observed for the samples annealed at 950 °C. The measurement of the FeMn10 sample looks similar; however, the detected intensity of the γ reflexes was higher. The measurement of the annealed FeMn15/17 samples showed a different behavior. Here, annealing led to the reduction of the α'-phase reflexes, while reflexes of the γ- and ε-phase became more pronounced. The FeM15/17 samples did not even show any definite α'-phase reflexes in the annealed state. However, in general the reflexes were quite broad; therefore, the main $\alpha'1$ reflex cannot be definitively excluded.

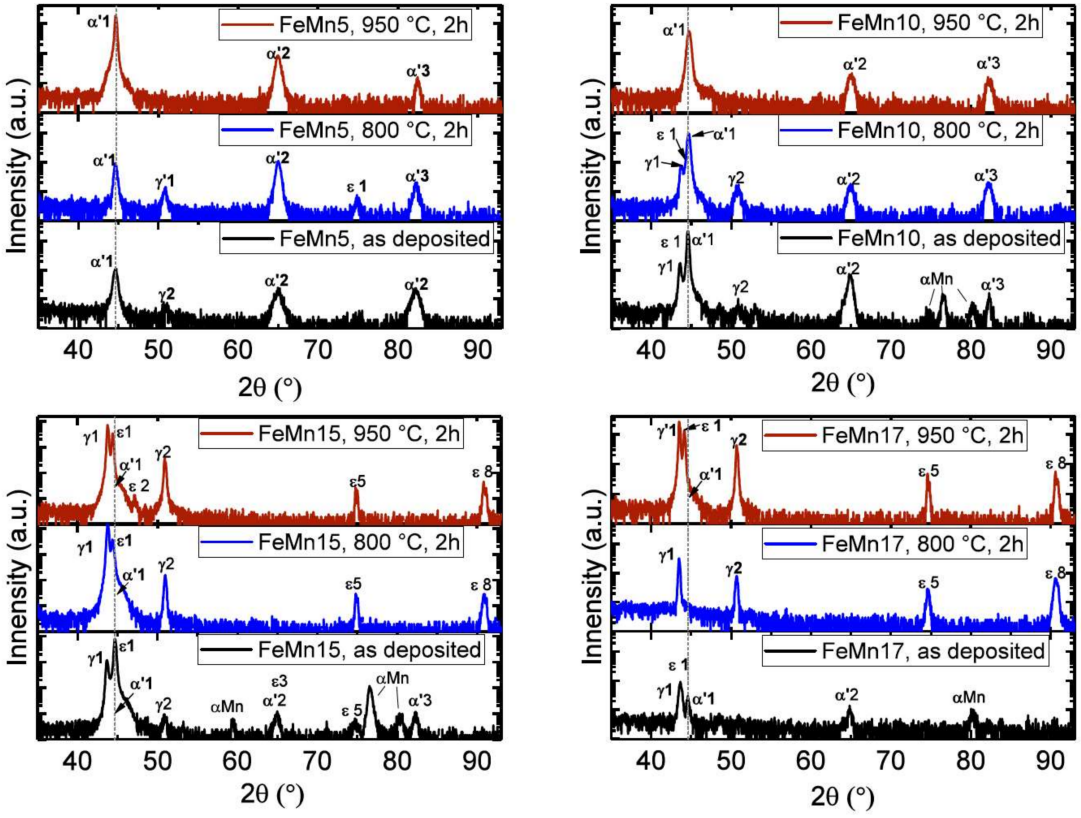

Figure 2. XRD measurements of different FeMnX samples in the as deposited and annealed state. The 2θ angles and lattice planes corresponding to the labeled reflexes are presented in Table 2.

Table 2. List of relevant 2θ angles, corresponding phases and lattice planes.

Symbol	2θ (°)	hkl
α′ 1	44.660	110
α′ 2	65.000	200
α′ 3	82.300	211
γ 1	43.120	111
γ 2	50.220	200
γ 3	73.760	220
γ 4	89.460	311
ε 1	41.160	100
ε 2	44.380	002
ε 3	47.040	101
ε 4	62.120	102
ε 5	75.020	110
ε 6	83.640	103
ε 7	89.360	200
ε 8	91.540	112

3.1.2. Scanning Electron Microscopy

Figure 3 shows the cross-sectional SEM images used to determine the grain sizes of the samples. The grain size values are presented in Table 3. After annealing, there was no evidence for a layered structure like in the as deposited samples, exemplary shown for the FeMn15 sample in Figure 3a. Overall, the annealed samples showed a homogeneous fine-grained structure. The mean grain size was in the sub-µm range for the 800 °C as well as for the 950 °C annealed samples. In general, with higher annealing temperatures, larger grain size values were observed. Furthermore, there is a trend of decreasing grain size with increasing Mn content, independently of the annealing temperature.

Table 3. Grain sizes.

Sample	$\overline{d}$ (µm)	d_{min} (µm)	d_{max} (µm)
Fe 800 °C, 2 h [12]	3.01	-	-
FeMn5 800 °C, 2 h	0.621	0.062	2.139
FeMn10 800 °C, 2 h	0.521	0.093	1.731
FeMn15 800 °C, 2 h	0.481	0.076	1.497
FeMn17 800 °C, 2 h	0.406	0.078	1.133
FeMn32 800 °C, 2 h [15]	0.965	3.193	0.068
FeMn5 950 °C, 2 h	0.965	0.223	3.478
FeMn10 950 °C, 2 h	0.860	0.179	2.208
FeMn15 950 °C, 2 h	0.843	0.216	2.635
FeMn17 950 °C, 2 h	0.578	0.990	1.618
FeMn32 950 °C, 2 h [15]	1.305	5.078	0.143

3.2. Corrosion

In Table 4 and Figure 4, the results of the corrosion measurements are presented. In addition, previously-presented values of pure Fe and FeMn32 [12,14,15] are given as a reference. The CR determined from the electrochemical measurements were decreasing with increasing Mn content (0–10 wt %) at first; this decrease is saturated with further increase of the Mn content (15–32 wt %) and remains constant within the error range. With lower Mn concentrations, a higher CR is found for the samples annealed at 950 °C. At higher Mn concentrations, there is no evidence for the influence of the annealing temperature on the CR.

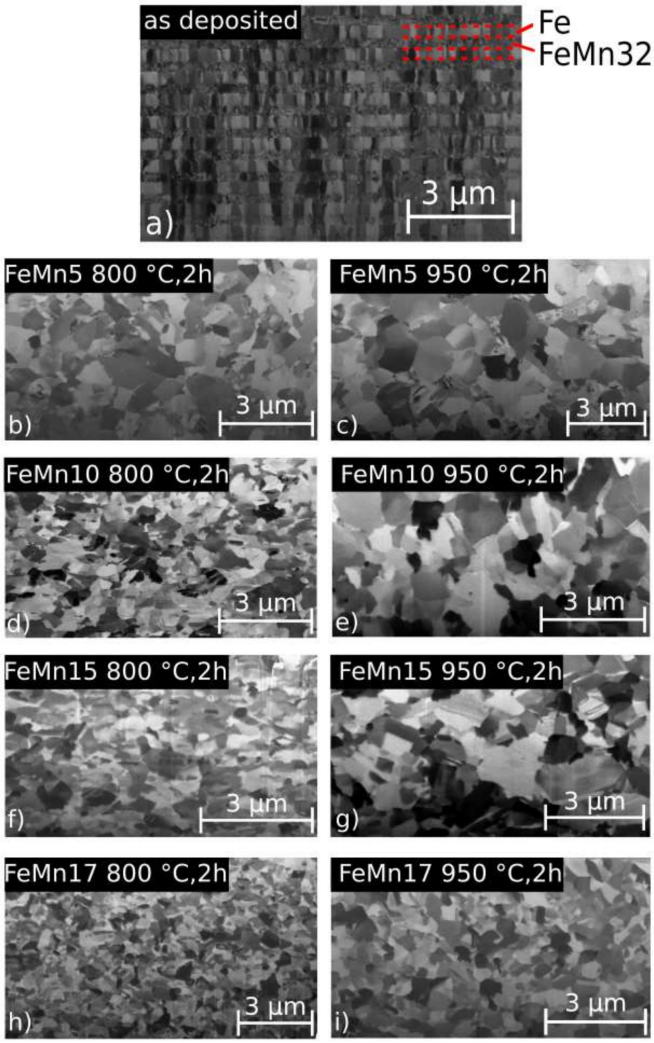

Figure 3. Cross-sectional SEM images of the microstructure: (**a**) shows the example as-deposited micro structure (FeMn15 sample). (**b**) shows FeMn5 at 800 °C, for 2 h; (**c**) FeMn5 at 950 °C, for 2 h; (**d**) FeMn10 at 800 °C, for 2 h; (**e**) FeMn10 at 950 °C, for 2 h; (**f**) FeMn15 at 800 °C, for 2 h; (**g**) FeMn15 at 950 °C, for 2 h; (**h**) FeMn17 at 800 °C, for 2 h; and (**i**) FeMn17 at 950 °C, for 2 h.

Table 4. Mean values of U_0, j_0, corrosion rate (CR), and weight loss (WL), determined from the electrochemical and immersion corrosion measurements.

Sample	U_0 (V)	j_0 (A/m^2)	CR (mm/year)	WL (mg/cm^2)
Fe 800 °C, 2 h [12,14]	−0.661 ± 0.019	0.092 ± 0.008	0.101 ± 0.009	3.80 ± 0.84
Fe 950 °C, 2 h	−0.657 ± 0.025	0.109 ± 0.025	0.120 ± 0.012	3.01 ± 0.54
FeMn5 800 °C, 2 h	−0.705 ± 0.007	0.651 ± 0.010	0.072 ± 0.006	3.17 ± 1.01
FeMn5 950 °C, 2 h	−0.704 ± 0.015	0.073 ± 0.006	0.081 ± 0.007	2.25 ± 0.48
FeMn10 800 °C, 2 h	−0.724 ± 0.006	0.053 ± 0.005	0.059 ± 0.006	2.34 ± 0.99
FeMn10 950 °C, 2 h	−0.719 ± 0.004	0.064 ± 0.007	0.071 ± 0.006	1.98 ± 0.64
FeMn15 800 °C, 2 h	−0,735 ± 0,008	0.036 ± 0.006	0.040 ± 0.018	1.65 ± 0.63
FeMn15 950 °C, 2 h	−0.728 ± 0.008	0.038 ± 0.019	0.042 ± 0.008	1.49 ± 0.45
FeMn17 800 °C, 2 h	−0.737 ± 0.018	0.034 ± 0.008	0.030 ± 0.008	1.41 ± 0.32
FeMn17 950 °C, 2 h	−0.737 ± 0,019	0.030 ± 0.002	0.033 ± 0.002	1.42 ± 0.35
FeMn32 800 °C, 2 h [15]	−0.749 ± 0.006	0.041 ± 0.011	0.045 ± 0.012	1.81 ± 0.65
FeMn32 950 °C, 2 h [15]	−0.741 ± 0.010	0.048 ± 0.010	0.054 ± 0.011	1.68 ± 0.75

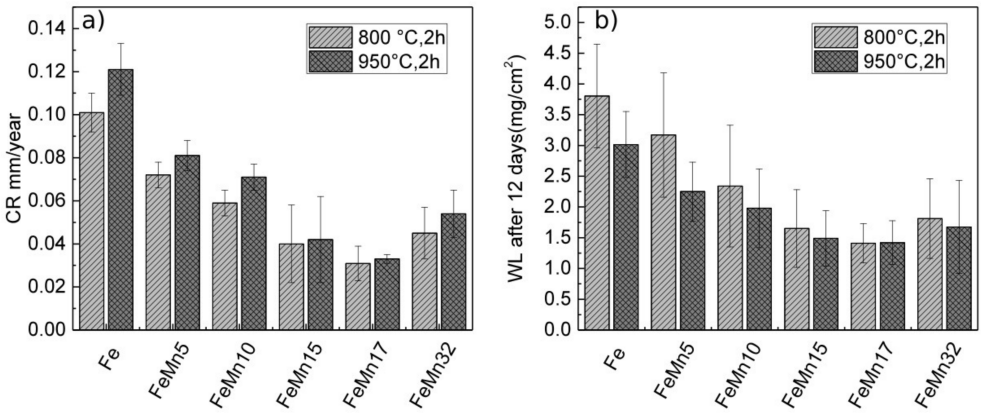

Figure 4. Graphically representation of (**a**) the mean corrosion rates and standard deviations determined from the electrochemical polarization measurements, and (**b**) the weight loss determined by immersion tests.

3.3. Mechanical Properties

Figure 5 shows the graphical depiction of fractures strain (A), yield strength (YS), and ultimate tensile strength (UTS) of all samples. The values are presented in Table 5. Additionally, the values for pure Fe [12] and FeMn32 are given as a reference. At low Mn concentrations (5 wt %, 10 wt %), the fracture strain was significantly smaller compared to that of pure Fe. The fracture strain of the FeMn10 samples was slightly lower compared to that of the FeMn5 samples. The YS and UTS of the FeMnX samples was strongly increased compared to those of pure Fe. The strength increased with the Mn content up to 10 wt %, and slightly decreased at higher Mn concentrations (>10 wt %). The YS of the FeMn17 sample was higher compared to the YS of FeMn15 for both annealing temperatures, whereas the UTS was almost the same for both sample types.

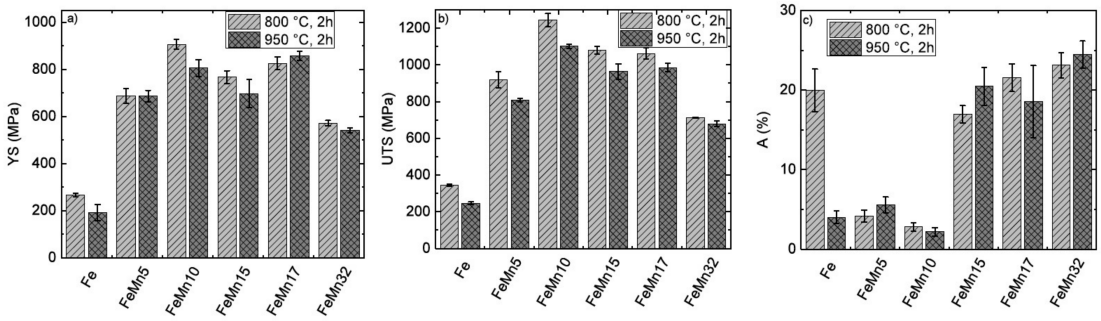

Figure 5. Graphically depiction of the (**a**) yield strength (YS), (**b**) ultimate tensile strength (UTS) and (**c**) fracture strain (A) for the different FeMnX samples, after annealing at 800 °C and 950 °C for 2 hours. Additionally, the values of pure Fe [12] and FeMn32 are shown [15].

3.4. Magnetic Properties

In Table 6, the characteristic values for J_S, J_R, $\mu_0 H_C$, χ_{max}, and E_{diss} are presented. The influence of the different Mn concentrations on J_S, χ_{max}, and E_{diss} are graphically displayed in Figure 6. In general, the values of J_S, J_R, and χ_{max}, of the as deposited samples decreased with increasing Mn content. In comparison, with the as-deposited samples, J_S, J_R, and χ_{max} decreased after annealing. However, at lower Mn concentrations (5/10 wt %), the values of the samples annealed at higher temperatures increased. Samples with higher Mn content (15–32 wt %) showed a decreasing tendency of J_S, J_R, and

χ_{max} with increasing annealing temperature. The E_{diss} of the as-deposited samples first increased up to a Mn content of 10 wt %, and then stayed more or less constant. The FeMn32 showed a marked decrease of E_{diss}. Annealing led to a decrease of E_{diss} compared to the as-deposited samples. At higher Mn concentrations (15/17 wt %), a marked drop of E_{diss} was observed.

Table 5. Mean values and standard deviations of the mechanical properties for the different FeMnX samples after annealing. Additionally, the values for sputtered pure Fe [12] and FeMn32 are given [15], as well as the SS 316 L gold standard [10] and required reference values for the desired application.

Sample	YS (MPa)	UTS (MPa)	A (%)
Fe 800 °C, 2 h [12]	266.9 ± 7.5	343.8 ± 4.8	20.0 ± 2.7
Fe 950 °C, 2 h	191.3 ± 34.7	246.6 ± 7.3	4.0 ± 0.8
FeMn5 800 °C, 2 h	686.2 ± 32.0	918.2 ± 44.6	4.2 ± 0.6
FeMn5 950 °C, 2 h	686.3 ± 24.1	809.1 ± 9.7	5.6 ± 1.0
FeMn10 800 °C, 2 h	905.8 ± 21.3	1242.9 ± 36.2	2.8 ± 0.5
FeMn10 950 °C, 2 h	805.3 ± 35.3	1100.9 ±11.5	2.2 ± 0.5
FeMn15 800 °C, 2 h	766.6 ± 27.1	1080.7± 20.9	17.0 ± 1.1
FeMn15 950 °C, 2 h	697.4 ± 59.7	963.9 ± 41.8	20.5 ± 2.4
FeMn17 800 °C, 2 h	824.8 ± 27.0	1061.4 ± 29.4	21.5 ± 1.7
FeMn17 950 °C, 2 h	857.0 ± 18.8	984.7 ± 22.9	18.5 ± 4.6
FeMn32 800 °C, 2 h [15]	571.0 ± 11.5	712.5 ± 3.7	23.1 ± 1.6
FeMn32 950 °C, 2 h [15]	541.0 ± 10.9	678.9 ± 15.9	24.4 ± 1.7
SS 316 L [10,33]	190	490	40
Required properties [34]	>200	>300	>15–18

Table 6. Magnetic properties.

Sample	J_S (T)	J_R (T)	$\mu_0 H_C$ (mT)	χ_{max}	E_{diss} (mJ/cm^3)
Fe as deposited [15]	2.206	0.650	1.874	560.59	10.50
Fe 800 °C, 2 h [15]	2.141	0.545	1.695	510.26	9.10
Fe 950 °C, 2 h [15]	2.052	0.715	1.147	595.34	7.77
FeMn5 as deposited	1.822	0.462	2.115	225.18	18.32
FeMn5 800 °C, 2 h	1.888	0.340	1.463	223.26	18.35
FeMn5 950 °C, 2 h	1.919	0.391	1.804	218.45	14.30
FeMn10 as deposited	1.542	0.682	2.62	270.22	19.59
FeMn10 800 °C, 2 h	1.619	0.486	2.530	221.57	12.59
FeMn10 950 °C, 2 h	1.726	0.395	1.876	207.46	10.83
FeMn15 as deposited	1.257	0.360	3.699	101.92	19.38
FeMn15 800 °C, 2 h	0.014	1.12×10^{-3}	8.440	0.18	0.24
FeMn15 950 °C, 2 h	9.31×10^{-3}	0.38×10^{-3}	12.549	0.04	0.13
FeMn17 as deposited	1.118	0.289	2.959	102.41	17.04
FeMn17 800 °C, 2 h	0.014	0.84×10^{-3}	8.026	0.14	0.20
FeMn17 950 °C, 2 h	9.40×10^{-3}	0.13×10^{-3}	7.129	0.09	0.09
FeMn32 as deposited [15]	0.032	6.02×10^{-3}	26.32	0.37	1.83
FeMn32 800 °C, 2 h [15]	1.09×10^{-3}	0.13×10^{-3}	14.752	0.02	0.03
FeMn32 950 °C, 2 h [15]	0.64×10^{-3}	0.04×10^{-3}	8.586	0.01	0.02
SS 316L [15]	2.65×10^{-3}	0.51×10^{-3}	30.212	0.02	0.11

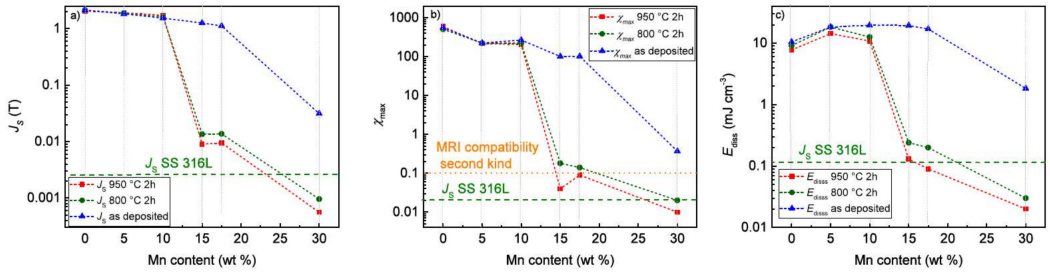

Figure 6. Graphic representation of the dependency between Mn content and (**a**) saturation polarization; (**b**) maximum susceptibility χ_{max}; and (**c**) dissipated energy. The values of the SS 316 L reference are indicated by the green horizontal line. Additionally, in (**b**) the MRI compatibility according to Schenck [3] (given below) is also indicated, as a horizontal orange dot line.

4. Discussion

4.1. Microstructure

It is shown that the presented approach is feasible for the fabrication of freestanding, in-situ structured Fe–FeMn composite films by using magnetron sputtering. From the SEM images, a clear separation of the layers was observed before annealing (Figure 3a). Based on the XRD measurements shown in Figure 2, as well as the previously-presented investigated microstructures of pure Fe [12] and FeMn32 [15], it is inferred that the pure Fe layers consisted of the ferritic α-Fe phase, while the FeMn32 layer was primarily composed of γ-FeMn, accompanied with small amounts of α-Fe. In contradiction to the results of the single layer FeMn32, even minor amounts of the ε-FeMn phase and α′-Mn phase are present, maybe related to the concentration shifts at the layer interfaces and the fact that a deposition by sputtering is not in thermodynamic equilibrium. Independent of the Mn content, after annealing the layer structure completely disappeared, and a recrystallized and homogeneous fine grained structure was observed. However, the Mn content showed a strong influence on the crystalline phase composition. According the XRD data, samples containing 5 wt % and 10 wt % Mn tended to increase the amount of α′-phase. However, the XRD data of the 800 °C annealed FeMn5/10 samples also showed evidence for the existence of the γ- and ε-phase. According to the XRD data of the annealed FeMn 15/17 samples, a stabilization of the ε- and γ-phase was observed. Nevertheless, due to the width of the overlapping reflexes, the α′(110) reflex cannot be assuredly excluded. Overall, the findings are in good agreement with the literature, and correlate with the non-equilibrium phase diagram of FeMn. The diagram predicts the formation of the α′-phase for Mn concentrations of 0–10 wt %. A phase mixture of α′-, ε-, and γ-phases is suggested for Mn concentrations of 10–14.5 wt %, while at concentrations of 14.5–27 wt % Mn, only ε- and γ-phases are expected [7,27]. The small grain sizes are attributed to the combination of different properties arising from the fabrication method. Sputtered films are known to exhibit a high defect density [35]. Also, the fabrication as Fe–FeMn multilayer may contribute to the grain size, since each layer interrupts a growing grain and provides additional nuclei. The combination of high defect densities and small initial grain sizes promotes recrystallization with a large number of additional nuclei, explaining the fine-grained microstructure after annealing. Furthermore, increasing the Mn content seems to have a grain-refining effect. In order to clearly distinguish between the influence of the grain size, the fabrication as multilayer, and the grain-refining effect of Mn, further studies would be necessary, in order to compare a multilayer system and single deposition of the same overall composition.

4.2. Mechanical Properties

The Mn content was found to strongly influence the mechanical properties. The FeMn5/10 samples both exhibited a high strength but low ductility. The high strength is, on one hand, attributed to the small grain size, in agreement with the Hall-Petch relation [36]; on the other hand, the strength is also attributed to the extensive solubility of the Mn atoms in the bcc Fe. With increasing Mn content, more Mn atoms are substituted for Fe atoms. The substituted Mn atoms induce internal stresses and hinder dislocation movement. As long as the α′-Fe phase is predominant, this results in an increasing strength and declining ductility at Mn concentrations 5/10 wt %. As discussed, higher amounts of Mn (15/17 wt %) lead to the stabilization of the ε- and γ-phase. These phases are known for showing the TRIP and TWIP effect. These effects occur due to the low stacking fault energy (SFE) of those alloys, which favor the formation of deformation twins or even a $\gamma \rightarrow \varepsilon$ phase transformation. Both effects are known to enhance mechanical strength and ductility, due to the extensive formation of deformation twins or strain-induced martensite. It is reported that both effects can coexist at lower Mn concentrations (23.8%). However, lower Mn concentrations favor the TRIP effect, whereas an intense strain-induced twinning, associated with the TWIP effect, is observed rather at higher Mn concentrations [37–39]. Therefore, it is assumed that at the Mn concentrations of 15/17 wt % used in this study, the TRIP effect is the predominant mechanism. The high strength of the FeMn15/17,

compared to pure iron, is mainly attributed to the TRIP effect. The strength is even higher than that of FeMn32. One reason for this can be that the TRIP effect was found to contribute more to strength than the TWIP effect [37], which is predominantly seen in the FeMn samples. However, the smaller grains of the FeMn15/17 samples will increase the strength as well. The smaller grains of the FeMn17 sample also explains the higher YS in comparison to the FeMn15 samples. Since phase boundaries also hinder plastic deformation, the dual-phase microstructure contributes to the strength as well, and gives an additional reason for the higher strength compared to the strength of FeMn32, which exhibits an exclusively austenitic structure [15]. In general, the films exhibit a superior strength. With respect to the mechanical requirements (Table 5), the FeMn15 and FeMn17 samples exhibited the best properties, namely a very high strength accompanied by sufficient ductility. The strength of the samples exceeded the values given for the SS 316 L gold standard, and were even up to four times higher than the required values.

4.3. Corrosion

The initial trend of a decreasing corrosion rate (Figure 4) with increasing Mn content is found for electrochemical measurements, as well as for immersion tests. It was the origin of the idea [40] of using FeMn alloys in order to accelerate the corrosion of biodegradable Fe-based alloys. Since the U_0 values shift to higher negative values with increasing Mn content, actually an increase of the corrosion rate was expected. However, the findings contradicted this expectation, and were in agreement with previous findings on sputtered FeMn32 [15]. The main decrease of CR already occurs at Mn concentrations of 5–10 wt %, which have a primarily ferritic structure. Thus, it is inferred that the major reason for the decrease is not the phase composition, but the Mn content. Studies on the influence of the electrolyte composition on the degradation behavior of FeMn alloys concluded that the amount of carbonate and hydrogen carbonate ions plays an essential role in the formation of insoluble $MnCO_3$ layers, which can hinder further degradation [32,41]. The $NaHCO_3$- and CO_2-rich atmosphere was used to adjust the pH value, thus favoring the formation of those protection layers and explaining the low degradation rate for the Mn rich samples. Since the decrease of CR saturates at Mn concentrations >10 wt %, it is assumed that a critical Mn concentration (10–15 wt %) is necessary to reach the full protective effect. In general, degradation is a complex chemical process, and depends on a variety of parameters. Even though the in vitro test gave a hint, a direct comparison with the literature is difficult, due to different testing conditions. Furthermore, in vitro tests are not able to mimic the living system 100%, which makes in vitro tests indispensable. Even though a lower corrosion rate is a drawback with respect to the application, the higher strength allows the use of thinner structures, and in turn a higher relative surface, which reduces the retention time of an implant in the body. To make a definitive assessment of the materials' suitability, in terms of the degradability, in vivo tests therefore should be performed in the future, even when considering geometrical design aspects.

4.4. Magnetic Properties

The magnetic properties (Figure 6 and Table 6) of the as-deposited samples mainly depend on the amount of FM α'-phase, where J_S, $J_{R,}$ and χ_{max} decrease with the Mn content and the amount of α'-phase. The increased E_{diss} of the FeMnX samples, compared to pure Fe, can be attributed to an FM–AFM pinning of the layers. This exchange anisotropy requires additional energy to rotate the magnetic moments, and is a well-known phenomenon [42]. The decrease of J_S, J_R, χ_{max}, and E_{diss} with increasing Mn content is also, on one hand, related to the crystalline phase composition. On the other hand, different amounts of alloying elements will also affect the magnetic moment per atom, and in turn the magnetization. Paduani et al. showed that, when alloying up to 17 wt % Mn into bcc-stabilized Fe, a decrease of the magnetization with increasing Mn content is observed. The authors concluded that the effect is related to an antiparallel coupling of the magnetic moments, between the Fe and Mn atoms substituted as nearest neighbors. This decrease was described as nonlinear, with the most pronounced drop between 12% and 17% Mn [43]. Considering the results of microstructural analysis

(Figure 2) at Mn concentrations <15 wt %, the decrease of J_S is related to the discussed mechanism. At higher Mn concentrations, the PM ε- and AFM γ-phases are primarily evident, explaining the low J_S, J_R, χ_{max}, and E_{diss}. Considering that, in terms of MRI compatibility, low values of J_S, χ, and E_{diss} are required, the FeMn15/17 shows the best values. Furthermore, higher annealing temperatures facilitate low J_S, χ, and E_{diss} values, probably due to the enhanced diffusion and, in turn, better homogenization. The values approach those of the SS 316 L standard. According to Schenk, the MRI compatibility of the first kind is defined as $10^{-5} < |\chi - \chi_{water}| < 10^{-2}$, where $\chi_{water} = -9.05 \times 10^{-6}$ [3]. According to this definition, the MRI compatibility is given for the FeMn15 and FeMn17 samples annealed at 950 °C.

5. Conclusions

It is shown that freestanding, in situ, structured Fe–FeMn32 multilayer films can be deposited via magnetron sputtering. By post-deposition annealing, the films can be homogenized, and a recrystallized, very fine-grained microstructure is obtained. The phase composition is influenced by the Mn content. At up to 10 wt %, the Mn α′-phase is present, whereas at Mn concentrations of 15 and 17 wt %, the γ- and ε-phase are observed. The Mn content significantly influences the material properties, summarized in the following:

- FeMn5: Showed a decrease of the ferromagnetic behavior and a decrease of the CR compared to pure Fe—a high strength, but a rather low ductility
- FeMn10: Further decrease of the ferromagnetic behavior and a further decrease of CR compared to FeMn5—an increase of strength, but lower ductility.
- FeMn15: Marked drop of ferromagnetic characteristics and a slightly decreased CR compared to FeMn10—lower but still high strength, with enhanced ductility.
- FeMn17: Similar magnetic and corrosion behavior to FeMn15, with a higher YS but similar UTS and ductility, compared to FeMn15.

With respect to the desired application, the FeMn15 and FeMn17 showed great potential and the best compromise between high strength, sufficient ductility, non-ferromagnetic behavior, and low Mn content. The samples distinctly exceeded the requirements in terms of the mechanical properties. Even the magnetic properties were very promising, and show that Mn concentrations of 15/17 wt % are sufficient in order to reach MRI compatibility of the first kind. The low degradation rate could be compensated for by increasing the relative surface of an implant. Thus, fabrication by magnetron sputtering is clearly beneficial, due to the fine-grained microstructure and in turn, the high strength that can be achieved. Furthermore, the small feature sizes that can be achieved by the in-situ structuring give a large freedom of design and make formative processing steps obsolete, which could affect the microstructure and material properties.

Acknowledgments: Funding of the project "ZA748/2-2" via DFG is gratefully acknowledged. Further acknowledgements to Ana María Araújo Cordero and Viktor Schell for supporting this work in the lab. Eckhard Quandt also thanks the Research Training Group 2154 "Materials for Brain" founded by the DFG.

Author Contributions: Till Jurgeleit evaluated the data and wrote the manuscript; Lea Katharina Jessen fabricated the samples and performed the experiments; Eckhard Quandt and Christiane Zamponi organized the research.

Conflicts of Interest: The authors declare no conflict of interest.

References

1. Peuster, M.; Wohlsein, P.; Brügmann, M.; Ehlerding, M.; Seidler, K.; Fink, C.; Brauer, H.; Fischer, A.; Hausdorf, G. A novel approach to temporary stenting: Degradable cardiovascular stents produced from corrodible metal-results 6–18 months afterimplantation into New Zealand white rabbits. *Heart* **2001**, *86*, 563–569. [CrossRef] [PubMed]
2. Peuster, M.; Hesse, C.; Schloo, T.; Fink, C.; Beerbaum, P.; von Schnakenburg, C. Long-term biocompatibility of a corrodible peripheral iron stent in the porcine descending aorta. *Biomaterials* **2006**, *27*, 4955–4962. [CrossRef] [PubMed]

3. Schenck, J.F. The role of magnetic susceptibility in magnetic resonance imaging: MRI magnetic compatibility of the first and second kinds. *Med. Phys.* **1996**, *23*, 815–850. [CrossRef] [PubMed]
4. Santamaria, A.B.; Sulsky, S.I. Risk assessment of an essential element: Manganese. *J. Toxicol. Environ. Health A* **2010**, *73*, 128–155. [CrossRef] [PubMed]
5. Lide, D. *Handbook of Chemistry and Physics-crc*, 90th ed.; CRC Press: Boca Raton, FL, USA, 2010.
6. Grässel, O.; Krüger, L.; Frommeyer, G.; Meyer, L. High strength Fe-Mn-(Al, Si) TRIP/TWIP steelsdevelopment—Properties—Application. *Int. J. Plast.* **2000**, *16*, 1391–1409. [CrossRef]
7. Schumann, H. Die martensitischen Umwandlungen in kohlenstoffarmen Manganstählen. *Arch. Eisenhüttenwes* **1967**, *38*, 647–656. [CrossRef]
8. Endoh, Y.; Ishikawa, Y. Antiferromagnetism of Iron Manganes Alloys. *J. Phys. Soc. Jpn.* **1971**, *30*, 1614–1627. [CrossRef]
9. Rabinkin, A. On magnetic contributions to $\gamma \rightarrow \varepsilon$ phase transformations in Fe-Mn alloys. *Calphad* **1979**, *3*, 77–84. [CrossRef]
10. Hermawan, H.; Dubé, D.; Mantovani, D. Degradable metallic biomaterials: Design and development of Fe-Mn alloys for stents. *J. Biomed. Mater. Res. A* **2010**, *93*, 1–11. [CrossRef] [PubMed]
11. Hermawan, H.; Alamdari, H.; Mantovani, D.; Dubé, D. Iron–manganese. *Powder Met.* **2013**, *51*, 38–45. [CrossRef]
12. Jurgeleit, T.; Quandt, E.; Zamponi, C. Magnetron Sputtering a New Fabrication Method of Iron Based Biodegradable Implant Materials. *Adv. Mater. Sci. Eng.* **2015**, *2015*, 294686. [CrossRef]
13. Zamponi, C.; Schürmann, U.; Jurgeleit, T.; Kienle, L.; Quandt, E. Microstructures of magnetron sputtered FeAu thin films. *IJMR* **2015**, *106*, 103–107. [CrossRef]
14. Jurgeleit, T.; Quandt, E.; Zamponi, C. Mechanical Properties and In Vitro Degradation of SputteredBiodegradable Fe-Au Foils. *Materials* **2016**, *9*, 928. [CrossRef] [PubMed]
15. Jurgeleit, T.; Quandt, E.; Zamponi, C. Magnetron Sputtering as a Fabrication Method for a Biodegradable Fe32Mn Alloy. *Materials* **2017**, *10*, 1196. [CrossRef] [PubMed]
16. Zamponi, C.; Rumpf, H.; Schmutz, C.; Quandt, E. Structuring of sputtered superelastic NiTi thin films byphotolithography and etching. *Mater. Sci. Eng. A* **2008**, *481–482*, 623–625. [CrossRef]
17. De Miranda, R.L.; Zamponi, C.; Quandt, E. Fabrication of TiNi thin film stents. *Smart Mater. Struct.* **2009**, *18*, 104010. [CrossRef]
18. DeMiranda, R.L.; Zamponi, C.; Quandt, E. Micropatterned Freestanding Superelastic TiNi Films. *Adv. Eng. Mater.* **2013**, *15*, 66–69. [CrossRef]
19. Siekmeyer, G.; Schüßler, A.; de Miranda, R.L.; Quandt, E. Comparison of the Fatigue Performance of Commercially Produced Nitinol Samples versus Sputter-Deposited Nitinol. *J. Mater. Eng. Perform.* **2014**, *23*, 2437–2445. [CrossRef]
20. Schlüter, K.; Zamponi, C.; Piorra, A.; Quandt, E. Comparison of the corrosion behaviour of bulk and thin film magnesium alloys. *Corros. Sci.* **2010**, *52*, 3973–3977. [CrossRef]
21. Schlüter, K.; Zamponi, C.; Hort, N.; Kainer, K.U.; Quandt, E. Polycrystalline and amorphous MgZnCa thin films. *Corros. Sci.* **2012**, *63*, 234–238. [CrossRef]
22. Schlüter, K.; Shi, Z.; Zamponi, C.; Cao, F.; Quandt, E.; Atrens, A. Corrosion performance and mechanical properties of sputter-deposited MgY and MgGd alloys. *Corros. Sci.* **2014**, *78*, 43–54. [CrossRef]
23. Haffner, D.; Zamponi, C.; de Miranda, R.L.; Quandt, E. Micropatterned freestanding magnetron sputtered Mg-alloy scaffolds. *BioNanoMaterials* **2015**, *16*, 19–22. [CrossRef]
24. Jynge, P.; Brurok, H.; Asplund, A.; Towart, R.; Refsum, H.; Karlsson, J.O.G. Cardiovascular safety of MnDPDP and $MnCl_2$. *Acta Radiol.* **1997**, *38*, 740–749. [CrossRef] [PubMed]
25. Crossgrove, J.; Zheng, W. Manganese toxicity upon overexposure. *NMR Biomed.* **2004**, *17*, 544–553. [CrossRef] [PubMed]
26. Lee, Y.-K.; Jun, J.-H.; Choi, C.-S. Damping Capacity in Fe-Mn Binary Alloys. *ISIJ Int.* **1997**, *37*, 1023–1030. [CrossRef]
27. Martínez, J.; Cotes, S.M.; Cabrera, A.F.; Desimoni, J.; Fernández Guillermet, A. On the relative fraction of ε martensite in γ-Fe-Mn alloys. *Mater. Sci. Eng. A* **2005**, *408*, 26–32. [CrossRef]
28. American Society for Testing Materials. *Annual Book of ASTM Standards: Metal Test Methods and Analytical Procedures*; Metals—Mechanical Testing; Elevated and Low-Temperature Tests; Metallography. Section 3. Volume 03.01; American Society for Testing Materials: West Conshohocken, PA, USA, 2007.

29. Stern, M.; Geary, A.L. Electrochemical polarization I. A theoretical analysis of the shape of polarization curves. *J. Electrochem. Soc.* **1957**, *104*, 56–63. [CrossRef]
30. Jones, D.A. *Principles and Prevention of Corrosion*, 2nd ed.; Pearson-Prentice Hall: London, UK, 1996.
31. Zhu, S.; Huang, N.; Xu, L.; Zhang, Y.; Liu, H.; Sun, H.; Leng, Y. Biocompatibility of pure iron. *Mater. Sci. Eng. B* **2009**, *29*, 1589–1592. [CrossRef]
32. Mouzou, E.; Paternoster, C.; Tolouei, R.; Purnama, A.; Chevallier, P.; Prima, F.; Mantovani, D. In vitro degradation behavior of Fe-20 Mn-1.2C alloy in three different pseudo-physiological solutions. *Matter. Sci. Eng. C Mater. Biol. Appl.* **2016**, *61*, 564–573. [CrossRef] [PubMed]
33. Moravej, M.; Prima, F.; Fiset, M.; Mantovani, D. Electroformed iron as new biomaterial for degradable stents: Development process and structure properties relationship. *Acta Biomater.* **2010**, *6*, 1726–1735. [CrossRef] [PubMed]
34. Heiden, M.; Walker, E.; Stanciu, L. Magnesium, Iron and Zinc Alloys, the Trifecta of Bioresorbable Orthopaedic and Vascular Implantation-A Review. *J. Biotechnol. Biomater.* **2015**. [CrossRef]
35. Thornton, J.A. High Rate Thick Film Growth. *Annu. Rev. Mater. Sci.* **1977**, *7*, 239–260. [CrossRef]
36. Hall, E.O. The Deformation and Ageing of Mild Steel: III Discussion of Results. *Proc. Phys. Soc. Sect. B* **1951**, *64*, 747–752. [CrossRef]
37. Ding, H.; Tang, Z.Y.; Li, W.; Wang, M.; Song, D. Microstructures and Mechanical Properties of Fe-Mn-(Al, Si) TRIP/TWIP Steels. *J. Iron Steel Res. Int.* **2006**, *13*, 66–70. [CrossRef]
38. Bouaziz, O.; Allain, S.; Scott, C.P.; Cugy, P.; Barbier, D. High manganese austenitic twinning induced plasticity steels. *Curr. Opin. Solid State Mater.* **2011**, *15*, 141–168. [CrossRef]
39. Neu, R.W. Performance and Characterization of TWIP Steels for Automotive Applications. *Mater. Perform. Charact.* **2013**, *2*, 244–284. [CrossRef]
40. Hermawan, H.; Mantovani, D. Process of prototyping coronary stents from biodegradable Fe-Mn alloys. *Acta Biomater.* **2013**, *9*, 8585–8592. [CrossRef] [PubMed]
41. Mouzou, E.; Paternoster, C.; Tolouei, R.; Chevallier, P.; Biffi, C.A.; Tuissi, A.; Mantovani, D. CO_2-rich atmosphere strongly affects the degradation of Fe-21Mn-1C for biodegradable metallic implants. *Mater. Lett.* **2016**, *181*, 362–366. [CrossRef]
42. Ivan, N.J.; Schuller, K. Exchange bias. *J. Magn.* **1999**, *192*, 203–232.
43. Paduani, C.; Galvão da Silva, E.; Perez-Alcazar, G.A.; McElfresh, M. Mössbauer effect and magnetization studies of α-FeMn alloys. *J. Appl. Phys.* **1991**, *70*, 7524–7531. [CrossRef]

© 2018 by the authors. Licensee MDPI, Basel, Switzerland. This article is an open access article distributed under the terms and conditions of the Creative Commons Attribution (CC BY) license (http://creativecommons.org/licenses/by/4.0/).

7 Conclusion

Freestanding, filigree structured Fe, Fe-Au, and FeMn(Xwt%) (FeMn(X)) foils were successfully fabricated by magnetron sputtering in combination with UV-lithography. In the following, the key findings for the different material systems are presented.

Fe
A higher strength ≈ 15–40 % compared to cast, rolled [Oba+16] [Oba+15] and electroformed [Mor+10a] Fe was found, accompanied with sufficient ductility. The initial corrosion rate of the annealed samples was up to 66 % increased, scaling with annealing temperature and grain size, respectively. However no significant acceleration in the long term corrosion rate could be proofed for the annealed samples. The pure Fe samples showed a typically ferromagnetic behavior with values common for Fe.

Fe − Au
It was shown that the multilayer deposition in combination with annealing is feasible to implement fine precipitates. Due to these gold precipitates and resulting in micro galvanic corrosion, the corrosion rate was significantly increased, up to ≈ 40–80 %, compared to the pure Fe reference. However, the variation of the Au content did not significantly influenced the corrosion rate. On one hand, the strength was found to be ≈ 77–100 % higher compared to the pure Fe reference, decreasing with higher annealing temperature and increasing with Au content. On the other hand a limited ductility (fracture strain $< 1 - 11\%$) was found, especially at high Au contents.The samples containing 1 at% Au exhibited the best compromise between increased strength and ductility.

FeMn(Xwt%)
Depending on the Mn content an up to ≈ 310 % higher strength compared to pure Fe was found. The strength of the FeMn32 samples exhibited a ≈ 20-30 % higher strength compared to the similar, powder sintered FeMn30/35 alloys presented by Hermawan et al. [HDM08][Her+08]. Compared to the FeMn32 samples a twofold strength was found for the FeMn15 and FeMn17 samples. Furthermore, these FeMn32, FeMn15 and FeMn17 samples exhibited a fracture strain suitable for the desired application. Even though the corrosion rate was ≈ 60% lower compared to pure Fe, this is compensated by the threefold increase in strength compared to pure Fe.
This enable a reduction of the strut cross section and in turn allow a reduction of the degradation time by ≈ 60%. Additionally, non ferromagnetic behavior was observed for FeMn samples with Mn contents ≥ 15 wt%. This non ferromagnetic behavior shows that MRI compatibility of first kind can be reached at 15 wt% Mn which is 5 wt% lower than previously reported by Hermawan et al. [HDM08]. This aids to further decrease the risk of intoxication due to a Mn over exposure. Summarized, the foils exhibit a strength due to the unique microstructure that is achieved by the fabrication by magnetron sputtering. The values are higher compared to reference values of comparable material found in literature which can be also seen in Fig. 7.0.1. Especially the FeMn15/17 shows a great compromise between corrosion, mechanical and magnetic properties. Due to the stabilization of the non-ferromagnetic ϵ- and γ-phases, for FeMn alloys with a Mn content ≥15 %, these materials exhibit a low magnetization and magnetic susceptibility and thus reach MRI compatibility of the first kind. In addition, the decreased corrosion rate is compensated by its high strength, because it increases the freedom in design, which allows a

modification of the relative surface of an implant and in turn its degradation time. Also it was shown that a the implementation of Au precipitates allows an acceleration of the degradation. For this reason the fabrication by magnetron sputtering in combination with UV-lithography is very advantageous as it allows very small feature sizes. Furthermore, in situ structuring of the material makes an shape giving processing step obsolete. Such processing steps like dicing or laser cutting will affect the material properties by e.g. work hardening or heat affected zones. In terms of this aspect the presented method is superior compared to powder sintered, ECAP, or rolled material because the microstructure and material properties are adjusted after giving the shape to the material, and not the other way around.
Due to the possible combination of a large freedom of design, unique microstructure and material properties there is a great potential for the fabrication of Fe based medical devices by magnetron sputtering in combination with UV-Lithography.

Perspective
In future, tests regarding the influence of different designs on the degradation time should be performed. Because the in vitro tests can only give an idea about the degradation behavior, in vivo tests are indispensable in order to validate the suitability in terms of degradability.
Even though the presented material showed very promising properties, there is still room for further improvements. One possible option would be the combination of the concepts presented in this work. The combination of FeMn with Au or other noble metals for example, should accelerate the degradation rate and further enhance the strength. An other logical step would be the deposition of ternary or quaternary alloy where C or Si. These alloys seems to be promising in order to enhance the material properties. Besides the fabrication of small degradable implants, the method shown in this work could also help to develop biodegradable microelectronic mechanical devices (MEMS) for medical applications. Hereby the introduced process could fully exploit its strentgh of the small feature sizes and integrability that can be achieved. Possible devices would be pressure sensors [Bou+13], micro-osmotic pumps [Ryu+07] or passive wireless communication devices for biosensors [Bou+13]. The ferromagnetic and magnetostrictive properties of Fe could be even beneficial for the development of smart magnetic devices like endoscopic robots or delivery systems [Pou+11].

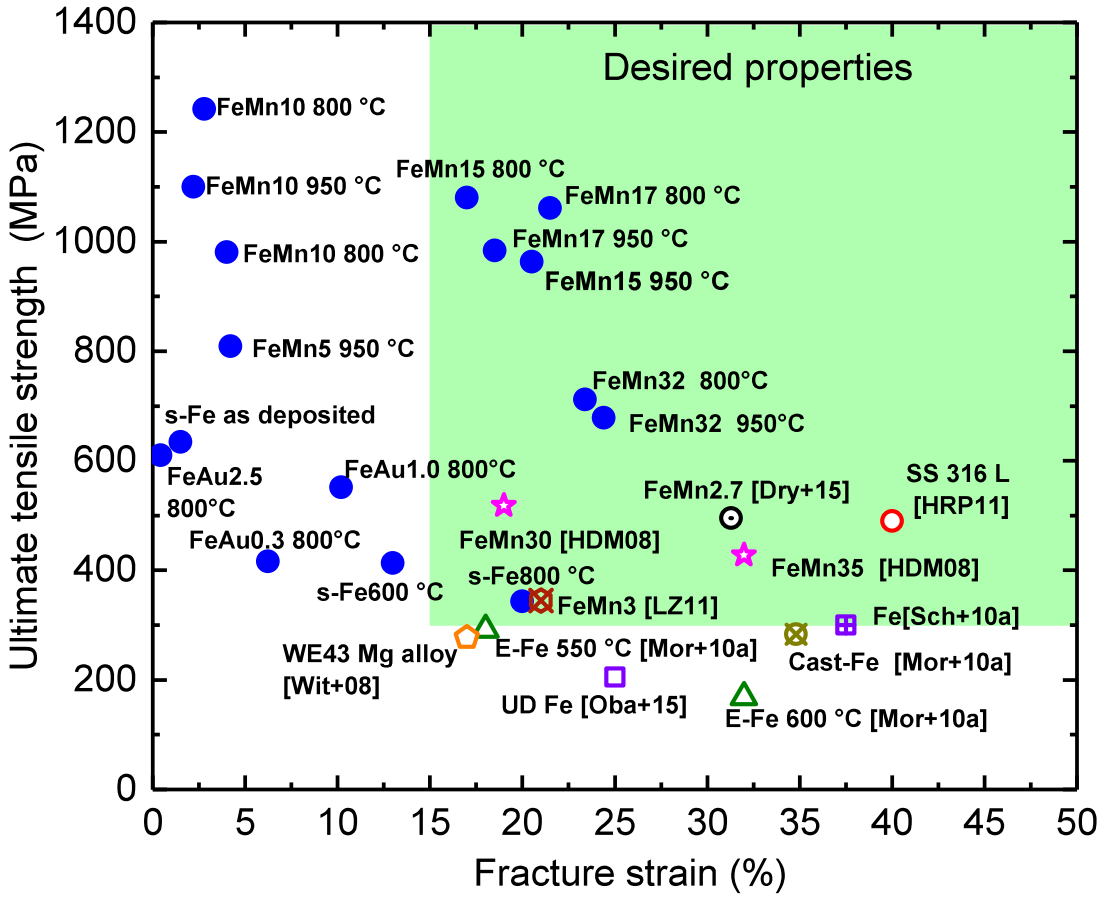

Figure 7.0.1: Compilation of the ultimate tensile strength and fracture strain, of different sputtered Fe-based materials presented in this work in comparison to literature values. For reasons of clarity only literature values of materials with similar compositions (pure-Fe, binary FeMn and the SS 316 L gold standard) are considered. Furthermore only those values are shown, that at least almost fulfill the mechanical requirements for vascular implants, specified in Tab. 3.0.1.
and indicated by the colored area. The filled circular symbols indicate values determined in this work, the hollow symbols indicate values presented in various publications.

Bibliography

[AL13] R. D. Alexy and D. S. Levi. "Materials and manufacturing technologies available for production of a pediatric bioabsorbable stent". In: *BioMed research international* 2013 (2013), p. 137985.

[BDG13] P. K. Bowen, J. Drelich, and J. Goldman. "Zinc exhibits ideal physiological corrosion behavior for bioabsorbable stents". In: *Advanced materials (Deerfield Beach, Fla.)* 25.18 (2013), pp. 2577–2582.

[Bou+11] O. Bouaziz, S. Allain, C. P. Scott, P. Cugy, and D. Barbier. "High manganese austenitic twinning induced plasticity steels: A review of the microstructure properties relationships". In: *Current Opinion in Solid State and Materials Science* 15.4 (2011), pp. 141–168.

[Bou+13] C. M. Boutry, H. Chandrahalim, P. Streit, M. Schinhammer, A. C. Hänzi, and C. Hierold. "Characterization of miniaturized RLC resonators made of biodegradable materials for wireless implant applications". In: *Sensors and Actuators A: Physical* 189 (2013), pp. 344–355.

[Bun77] R. F. Bunshah. "3.1 mechanical properties of PVD films". In: *Vacuum* 27 (1977), pp. 353–362.

[Cap+16] J. Capek, J. Kubasek, D. Vojtech, E. Jablonska, J. Lipov, and T. Ruml. "Microstructural, mechanical, corrosion and cytotoxicity characterization of the hot forged FeMn30(wt.%) alloy". In: *Materials science & engineering. C, Materials for biological applications* 58 (2016), pp. 900–908.

[Čap+17] J. Čapek, Š. Msallamová, E. Jablonská, J. Lipov, and D. Vojtěch. "A novel high-strength and highly corrosive biodegradable Fe-Pd alloy: Structural, mechanical and in vitro corrosion and cytotoxicity study". In: *Materials science & engineering. C, Materials for biological applications* 79 (2017), pp. 550–562.

[CH96] R. W. Cahn and P. Haasen, eds. *Physical metallurgy.* 4th, rev. and enhanced ed. Amsterdam and New York: North-Holland, 1996.

[Che+13] J. Cheng, B. Liu, Y. H. Wu, and Y. F. Zheng. "Comparative in vitro Study on Pure Metals (Fe, Mn, Mg, Zn and W) as Biodegradable Metals". In: *Journal of Materials Science & Technology* 29.7 (2013), pp. 619–627.

[Cho+13] D. T. Chou, D. Wells, D. Hong, B. Lee, H. Kuhn, and P. N. Kumta. "Novel processing of iron-manganese alloy-based biomaterials by inkjet 3-D printing". In: *Acta biomaterialia* 9.10 (2013), pp. 8593–8603.

[CHZ15] J. Cheng, T. Huang, and Y. F. Zheng. "Relatively uniform and accelerated degradation of pure iron coated with micro-patterned Au disc arrays". In: *Materials science & engineering. C, Materials for biological applications* 48 (2015), pp. 679–687.

[CK00] A. Colombo and E. Karvouni. "Biodegradable Stents: Fulfilling the Mission and Stepping Away". In: *Circulation* 102.4 (2000), pp. 371–373.

[CL02] E. Chang and T. Lee. "Effect of surface chemistries and characteristics of Ti6Al4V on the Ca and P adsorption and ion dissolution in Hank's ethylene diamine tetraacetic acid solution". In: *Biomaterials* 23.14 (2002), pp. 2917–2925.

[CSG95] S. Cotes, M. Sade, and A. F. Guillermet. "Fcc/Hcp martensitic transformation in the Fe-Mn system: Experimental study and thermodynamic analysis of phase stability". In: *Metallurgical and Materials Transactions A* 26.8 (1995), pp. 1957–1969.

[CZ04] J. Crossgrove and W. Zheng. "Manganese toxicity upon overexposure". In: *NMR in biomedicine* 17.8 (2004), pp. 544–553.

[CZ13a] J. Cheng and Y. F. Zheng. "In vitro study on newly designed biodegradable Fe-X composites (X = W, CNT) prepared by spark plasma sintering". In: *Journal of biomedical materials research. Part B, Applied biomaterials* 101.4 (2013), pp. 485–497.

[CZ13b] J. Cheng and Y. F. Zheng. "Microstructure, mechanical property, biodegradation behavior, and biocompatibility of biodegradable Fe–Fe2O3 composites". In: *Journal of Biomedical Materials Research Part B: Applied Biomaterials* 101B.4 (2013), pp. 485–497.

[Dav00] J. R. Davis. *Corrosion: Understanding the Basics*. A S M International, 2000.

[DIN+06] H. DING, Z.-Y. TANG, W. LI, M. WANG, and D. SONG. "Microstructures and Mechanical Properties of Fe-Mn-(Al, Si) TRIP/TWIP Steels". In: *Journal of Iron and Steel Research, International* 13.6 (2006), pp. 66–70.

[Dre+18] R. Drevet, Y. Zhukova, P. Malikova, S. Dubinskiy, A. Korotitskiy, Y. Pustov, and S. Prokoshkin. "Martensitic Transformations and Mechanical and Corrosion Properties of Fe-Mn-Si Alloys for Biodegradable Medical Implants". In: *Metallurgical and Materials Transactions A* 49.3 (2018), pp. 1006–1013.

[Dry+15] A. Drynda, T. Hassel, F. W. Bach, and M. Peuster. "In vitro and in vivo corrosion properties of new iron-manganese alloys designed for cardiovascular applications". In: *Journal of biomedical materials research. Part B, Applied biomaterials* 103.3 (2015), pp. 649–660.

[ES08] W. Erich and H. Suk-Woo. *Medizintechnik: Life Science Engineering*. 4th ed. Springer, 2008.

[Fen+13] Q. Feng, D. Zhang, C. Xin, X. Liu, W. Lin, W. Zhang, S. Chen, and K. Sun. "Characterization and in vivo evaluation of a bio-corrodible nitrided iron stent". In: *Journal of materials science. Materials in medicine* 24.3 (2013), pp. 713–724.

[Fon15] N. Fonstein. *Advanced High Strength Sheet Steels: Physical Metallurgy, Design, Processing, and Properties*. 1st ed. 2015. Cham: Springer, 2015.

[Geb+17] A. Gebert, F. Kochta, A. Voß, S. Oswald, M. Fernandez-Barcia, U. Kühn, and J. Hufenbach. "Corrosion studies on Fe-30Mn-1C alloy in chloride-containing solutions with view to biomedical application". In: *Materials and Corrosion* 16 (2017), p. 1391.

[Got07] G. Gottstein. *Physikalische Grundlagen der Materialkunde*. 3. Auflage. Springer-Lehrbuch. Berlin, Heidelberg: Springer-Verlag Berlin Heidelberg, 2007.

[Grä+00] O. Grässel, L. Krüger, G. Frommeyer, and L. Meyer. "High strength Fe–Mn–(Al, Si) TRIP/TWIP steels development — properties — application". In: *International Journal of Plasticity* 16.10-11 (2000), pp. 1391–1409.

[Haf+15] D. Haffner, C. Zamponi, R. Lima de Miranda, and E. Quandt. "Micropatterned freestanding magnetron sputtered Mg-alloy scaffolds". In: *BioNanoMaterials* 16.1 (2015).

[Hal51a] E. O. Hall. "The Deformation and Ageing of Mild Steel: II Characteristics of the Lüders Deformation". In: *Proceedings of the Physical Society. Section B* 64.9 (1951), pp. 742–747.

[Hal51b] E. O. Hall. "The Deformation and Ageing of Mild Steel: III Discussion of Results". In: *Proceedings of the Physical Society. Section B* 64.9 (1951), pp. 747–752.

[HCZ14] T. Huang, J. Cheng, and Y. F. Zheng. "In vitro degradation and biocompatibility of Fe-Pd and Fe-Pt composites fabricated by spark plasma sintering". In: *Materials science & engineering. C, Materials for biological applications* 35 (2014), pp. 43–53.

[HCZ16] T. Huang, Y. Cheng, and Y. Zheng. "In vitro studies on silver implanted pure iron by metal vapor vacuum arc technique". In: *Colloids and surfaces. B, Biointerfaces* 142 (2016), pp. 20–29.

[HDM08] H. Hermawan, D. Dubé, and D. Mantovani. "Degradable metallic biomaterials: design and development of Fe–Mn alloys for stents". In: *Journal of Biomedical Materials Research Part A* 93.1 (2008), pp. 1–11.

[HDM10] H. Hermawan, D. Dube, and D. Mantovani. "Developments in metallic biodegradable stents". In: *Acta biomaterialia* 6.5 (2010), pp. 1693–1697.

[Hei+15a] M. Heiden, E. Walker, E. Nauman, and L. Stanciu. "Evolution of novel bioresorbable iron-manganese implant surfaces and their degradation behaviors in vitro". In: *Journal of biomedical materials research. Part A* 103.1 (2015), pp. 185–193.

[Hei+15b] M. Heiden, A. Kustas, K. Chaput, E. Nauman, D. Johnson, and L. Stanciu. "Effect of microstructure and strain on the degradation behavior of novel bioresorbable iron-manganese alloy implants". In: *Journal of biomedical materials research. Part A* 103.2 (2015), pp. 738–745.

[Her+08] H. Hermawan, H. Alamdari, D. Mantovani, and D. Dubé. "Iron–manganese: New class of metallic degradable biomaterials prepared by powder metallurgy". In: *Powder Metallurgy* 51.1 (2008), pp. 38–45.

[Her12] H. Hermawan. *Biodegradable Metals*. Berlin, Heidelberg: Springer Berlin Heidelberg, 2012.

[HH06] B. Harshad K. D. H. and R. W. K. Honeycombe. *Steels Microstructure and properties*. 3. ed. Amsterdam: Elsevier/Butterworth-Heinemann, 2006.

[HMA04] M. W. Hentze, M. U. Muckenthaler, and N. C. Andrews. "Balancing Acts". In: *Cell* 117.3 (2004), pp. 285–297.

[HRP11] H. Hermawan, D. Ramdan, and J. R. P. Djuansjah. *Metals for Biomedical Applications*. Ed. by Intech. 2011.

[Hua+16] T. Huang, J. Cheng, D. Bian, and Y. Zheng. "Fe-Au and Fe-Ag composites as candidates for biodegradable stent materials". In: *Journal of biomedical materials research. Part B, Applied biomaterials* 104.2 (2016), pp. 225–240.

[Huf+17] J. Hufenbach, H. Wendrock, F. Kochta, U. Kühn, and A. Gebert. "Novel biodegradable Fe-Mn-C-S alloy with superior mechanical and corrosion properties". In: *Materials Letters* 186 (2017), pp. 330–333.

[HW06] E. Hornbogen and H. Warlimont. *Metalle: Struktur und Eigenschaften der Metalle und Legierungen*. 5., neu bearb. Aufl. Berlin and Heidelberg: Springer, 2006.

[HWS15] M. Heiden, E. Walker, and L. Stanciu. "Magnesium, Iron and Zinc Alloys, the Trifecta of Bioresorbable Orthopaedic and Vascular Implantation - A Review". In: *Journal of Biotechnology & Biomaterials* 05.02 (2015).

[HZ16] T. Huang and Y. Zheng. "Uniform and accelerated degradation of pure iron patterned by Pt disc arrays". In: *Scientific reports* 6 (2016), p. 23627.

[Jon96] D. A. Jones. *Principles and Prevention of Corrosion.* 2nd ed. London: Pearson-Prentice Hall, 1996.

[Kim+96] T. Kimura, H. Yokoi, Y. Nakagawa, T. Tamura, S. Kaburagi, Y. Sawada, Y. Sato, N. Hamasaki, and H. Nosaka. "Three-year follow-up after implantation of metallic coronary-artery stents". In: *The New England journal of medicine* 334.9 (1996), pp. 561–566.

[Koh+08] Y. Kohgo, K. Ikuta, T. Ohtake, and Y. Torimoto. "Body iron metabolism and pathophysiology of iron overload". In: *International journal of hematology* 88 (2008), pp. 7–15.

[KTN02] J. Kushibiki, I. Takanaga, and S. Nishiyama. "Accurate measurements of the acoustical physical constants of synthetic /spl alpha/-quartz for SAW devices". In: *IEEE Transactions on Ultrasonics, Ferroelectrics and Frequency Control* 49.1 (2002), pp. 125–135.

[Kuc07] H. Kuchling. *Taschenbuch der Physik.* Fachbuchverl. Leipzig im Carl-Hanser-Verlag, 2007.

[LEC14] S. Lee, Y. Estrin, and B. C. de Cooman. "Effect of the Strain Rate on the TRIP–TWIP Transition in Austenitic Fe-12 pct Mn-0.6 pct C TWIP Steel". In: *Metallurgical and Materials Transactions A* 45.2 (2014), pp. 717–730.

[Lid10] D. Lide. *handbook of chemistry and physics-crc (2010).* 90 (Internet Version). Boca Raton: CRC Press/Taylor and Francis, 2010.

[Lie+01] P. T. Lieu, M. Heiskala, P. A. Peterson, and Y. Yang. "The roles of iron in health and disease". In: *Molecular aspects of medicine* 22.1-2 (2001), pp. 1–87.

[Liu+13] M. Liu, D. Jing, Z. Zhou, and L. Guo. "Twin-induced one-dimensional homojunctions yield high quantum efficiency for solar hydrogen generation". In: *Nature communications* 4 (2013), p. 2278.

[Liu+18] R. Y. Liu, R.-G. He, L.-Q. Xu, and S.-F. Guo. "Design of Fe–Mn–Ag Alloys as Potential Candidates for Biodegradable Metals". In: *Acta Metallurgica Sinica (English Letters)* 258 (2018), p. 6087.

[LJC97] Y.-K. Lee, J.-H. Jun, and C.-S. Choi. "Damping Capacity in Fe-Mn Binary Alloys". In: *ISIJ International* 37.10 (1997), pp. 1023–1030.

[LSL09] K. H. Lo, C. H. Shek, and J. Lai. "Recent developments in stainless steels". In: *Materials Science and Engineering: R: Reports* 65.4-6 (2009), pp. 39–104.

[LZ11] B. Liu and Y. F. Zheng. "Effects of alloying elements (Mn, Co, Al, W, Sn, B, C and S) on biodegradability and in vitro biocompatibility of pure iron". In: *Acta biomaterialia* 7.3 (2011), pp. 1407–1420.

[LZQ09] R. Lima de Miranda, C. Zamponi, and E. Quandt. "Fabrication of TiNi thin film stents". In: *Smart Materials and Structures* 18.10 (2009), p. 104010.

[LZQ13] R. Lima de Miranda, C. Zamponi, and E. Quandt. "Micropatterned Freestanding Superelastic TiNi Films". In: *Advanced Engineering Materials* 15.1-2 (2013), pp. 66–69.

[Mad02] M. J. Madou. *Fundamentals of microfabrication: The science of miniaturization.* 2. ed. Boca Raton: CRC Press, 2002.

[Mar+01] P. Marinelli, A. Baruj, A. F. Guillermet, and M. Sade. "Lattice parameters of metastable structures in quenched Fe-Mn alloys. Part II: hcp phase". In: *Zeitschrift fur Metallkunde* 92.5 (2001), pp. 489–493.

[Mar+05] J. Martínez, S. M. Cotes, A. F. Cabrera, J. Desimoni, and A. Fernández Guillermet. "On the relative fraction of ε martensite in γ Fe–Mn alloys". In: *Materials Science and Engineering: A* 408.1-2 (2005), pp. 26–32.

[McG+00] D. McGregor, R. Baan, C. Partensky, J. Rice, and J. Wilbourn. "Evaluation of the carcinogenic risks to humans associated with surgical implants and other foreign bodies — a report of an IARC Monographs Programme Meeting". In: *European Journal of Cancer* 36.3 (2000), pp. 307–313.

[MM11] M. Moravej and D. Mantovani. "Biodegradable metals for cardiovascular stent application: interests and new opportunities". In: *International journal of molecular sciences* 12.7 (2011), pp. 4250–4270.

[Moh+14] N. Mohd Daud, N. B. Sing, A. H. Yusop, F. A. Abdul Majid, and H. Hermawan. "Degradation and in vitro cell–material interaction studies on hydroxyapatite-coated biodegradable porous iron for hard tissue scaffolds". In: *Journal of Orthopaedic Translation* 2.4 (2014), pp. 177–184.

[Mor+10a] M. Moravej, F. Prima, M. Fiset, and D. Mantovani. "Electroformed iron as new biomaterial for degradable stents: development process and structure-properties relationship". In: *Acta biomaterialia* 6.5 (2010), pp. 1726–1735.

[Mor+10b] M. Moravej, A. Purnama, M. Fiset, J. Couet, and D. Mantovani. "Electroformed pure iron as a new biomaterial for degradable stents: in vitro degradation and preliminary cell viability studies". In: *Acta biomaterialia* 6.5 (2010), pp. 1843–1851.

[Mor+11] M. Moravej, S. Amira, F. Prima, A. Rahem, M. Fiset, and D. Mantovani. "Effect of electrodeposition current density on the microstructure and the degradation of electroformed iron for degradable stents". In: *Materials Science and Engineering: B* 176.20 (2011), pp. 1812–1822.

[Mos+11] F. Moszner, A. S. Sologubenko, M. Schinhammer, C. Lerchbacher, A. C. Hänzi, H. Leitner, P. J. Uggowitzer, and J. F. Löffler. "Precipitation hardening of biodegradable Fe–Mn–Pd alloys". In: *Acta Materialia* 59.3 (2011), pp. 981–991.

[Mou+16a] E. Mouzou, C. Paternoster, R. Tolouei, P. Chevallier, C. A. Biffi, A. Tuissi, and D. Mantovani. "CO2-rich atmosphere strongly affects the degradation of Fe-21Mn-1C for biodegradable metallic implants". In: *Materials Letters* 181 (2016), pp. 362–366.

[Mou+16b] E. Mouzou, C. Paternoster, R. Tolouei, A. Purnama, P. Chevallier, D. Dube, F. Prima, and D. Mantovani. "In vitro degradation behavior of Fe-20 Mn-1.2C alloy in three different pseudo-physiological solutions". In: *Materials science & engineering. C, Materials for biological applications* 61 (2016), pp. 564–573.

[MT00] J. C. Middleton and A. J. Tipton. "Synthetic biodegradable polymers as orthopedic devices". In: *Biomaterials* 21.23 (2000), pp. 2335–2346.

[Neu13] R. W. Neu. "Performance and Characterization of TWIP Steels for Automotive Applications". In: *Materials Performance and Characterization* 2.1 (2013), p. 20130009.

[Nie+10] F. L. Nie, Y. F. Zheng, S. C. Wei, C. Hu, and G. Yang. "In vitro corrosion, cytotoxicity and hemocompatibility of bulk nanocrystalline pure iron". In: *Biomedical materials (Bristol, England)* 5.6 (2010), p. 065015.

[NZ12] F. L. Nie and Y. F. Zheng. "Surface chemistry of bulk nanocrystalline pure iron and electrochemistry study in gas-flow physiological saline". In: *Journal of biomedical materials research. Part B, Applied biomaterials* 100.5 (2012), pp. 1404–1410.

[Oba+15] C. S. Obayi, R. Tolouei, C. Paternoster, S. Turgeon, B. A. Okorie, D. O. Obikwelu, G. Cassar, J. Buhagiar, and D. Mantovani. "Influence of cross-rolling on the micro-texture and biodegradation of pure iron as biodegradable material for medical implants". In: *Acta biomaterialia* 17 (2015), pp. 68–77.

[Oba+16] C. S. Obayi, R. Tolouei, A. Mostavan, C. Paternoster, S. Turgeon, B. A. Okorie, D. O. Obikwelu, and D. Mantovani. "Effect of grain sizes on mechanical properties and biodegradation behavior of pure iron for cardiovascular stent application". In: *Biomatter* 6 (2016), e959874.

[OC09] B. O'Brien and W. Carroll. "The evolution of cardiovascular stent materials and surfaces in response to clinical drivers: a review". In: *Acta biomaterialia* 5.4 (2009), pp. 945–958.

[Ori+14] A. Oriňák, R. Oriňáková, Z. O. Králová, A. M. Turoňová, M. Kupková, M. Hrubovčáková, J. Radoňák, and R. Džunda. "Sintered metallic foams for biodegradable bone replacement materials". In: *Journal of Porous Materials* 21.2 (2014), pp. 131–140.

[Par65] Paracelsus. *Die dritte Defension wegen des Schreibens der neuen Rezepte: Sieben Defensiones*. Vol. 2. Darmstadt: Wissenschaftliche Buchgesellschaft, 1965.

[Peu+01] M. Peuster, P. Wohlsein, M. Brügmann, M. Ehlerding, K. Seidler, C. Fink, H. Brauer, A. Fischer, and G. Hausdorf. "A novel approach to temporary stenting:Degradable cardiovascular stents produced from corrodible metal—results 6-18 months after implantation into New Zealand white rabbits". In: *Heart* 86.5 (2001), pp. 563–569.

[Peu+06] M. Peuster, C. Hesse, T. Schloo, C. Fink, P. Beerbaum, and C. von Schnakenburg. "Long-term biocompatibility of a corrodible peripheral iron stent in the porcine descending aorta". In: *Biomaterials* 27.28 (2006), pp. 4955–4962.

[Pou+11] P. Pouponneau, O. Savadogo, T. Napporn, L. Yahia, and S. Martel. "Corrosion study of single crystal Ni-Mn-Ga alloy and Tb0.27Dy0.73Fe1.95 alloy for the design of new medical microdevices". In: *Journal of materials science. Materials in medicine* 22.2 (2011), pp. 237–245.

[Rat+12] B. D. Ratner, H. Allan S., S. Frederick J., and L. Jack E. *Biomaterials science: an introduction to materials in medicine*. 3rd ed. Academic Press, 2012.

[RBD10] K. D. Ralston, N. Birbilis, and C. Davies. "Revealing the relationship between grain size and corrosion rate of metals". In: *Scripta Materialia* 63.12 (2010), pp. 1201–1204.

[Rei+14] A. Reindl, R. Borowsky, S. B. Hein, J. Geis-Gerstorfer, P. Imgrund, and F. Petzoldt. "Degradation behavior of novel Fe/ß-TCP composites produced by powder injection molding for cortical bone replacement". In: *Journal of Materials Science* 49.24 (2014), pp. 8234–8243.

[RT95] M. Richard L. and S. Timothy A. "The history of interventional cardiology: Cardiac catheterization, angioplasty, and related interventions". In: *American Heart Journal* 129 (1995), pp. 146–172.

[Ryu+07] W. Ryu, Z. Huang, F. B. Prinz, S. B. Goodman, and R. Fasching. "Biodegradable micro-osmotic pump for long-term and controlled release of basic fibroblast growth factor". In: *Journal of controlled release : official journal of the Controlled Release Society* 124.1-2 (2007), pp. 98–105.

[Sch+10a] M. Schinhammer, A. C. Hanzi, J. F. Loffler, and P. J. Uggowitzer. "Design strategy for biodegradable Fe-based alloys for medical applications". In: *Acta biomaterialia* 6.5 (2010), pp. 1705–1713.

[Sch+10b] K. Schlüter, C. Zamponi, A. Piorra, and E. Quandt. "Comparison of the corrosion behaviour of bulk and thin film magnesium alloys". In: *Corrosion Science* 52.12 (2010), pp. 3973–3977.

[Sch+12a] M. Schinhammer, C. M. Pecnik, F. Rechberger, A. C. Hänzi, J. F. Löffler, and P. J. Uggowitzer. "Recrystallization behavior, microstructure evolution and mechanical properties of biodegradable Fe–Mn–C(–Pd) TWIP alloys". In: *Acta Materialia* 60.6-7 (2012), pp. 2746–2756.

[Sch+12b] K. Schlüter, C. Zamponi, N. Hort, K. U. Kainer, and E. Quandt. "Polycrystalline and amorphous MgZnCa thin films". In: *Corrosion Science* 63 (2012), pp. 234–238.

[Sch+13a] M. Schinhammer, I. Gerber, A. C. Hanzi, and P. J. Uggowitzer. "On the cytocompatibility of biodegradable Fe-based alloys". In: *Materials science & engineering. C, Materials for biological applications* 33.2 (2013), pp. 782–789.

[Sch+13b] M. Schinhammer, P. Steiger, F. Moszner, J. F. Löffler, and P. J. Uggowitzer. "Degradation performance of biodegradable Fe-Mn-C(-Pd) alloys". In: *Materials science & engineering. C, Materials for biological applications* 33.4 (2013), pp. 1882–1893.

[Sch+14] K. Schlüter, Z. Shi, C. Zamponi, F. Cao, E. Quandt, and A. Atrens. "Corrosion performance and mechanical properties of sputter-deposited MgY and MgGd alloys". In: *Corrosion Science* 78 (2014), pp. 43–54.

[Sch67] H. Schumann. "Die martensitischen Umwandlungen in kohlenstoffarmen Manganstählen". In: *Archiv für das Eisenhüttenwesen* 38.8 (1967), pp. 647–656.

[Sch96] J. F. Schenck. "The role of magnetic susceptibility in magnetic resonance imaging: MRI magnetic compatibility of the first and second kinds". In: *Medical physics* 23.6 (1996), pp. 815–850.

[Sie+14] G. Siekmeyer, A. Schüßler, R. Lima de Miranda, and E. Quandt. "Comparison of the Fatigue Performance of Commercially Produced Nitinol Samples versus Sputter-Deposited Nitinol". In: *Journal of Materials Engineering and Performance* 23.7 (2014), pp. 2437–2445.

[Sin+15] N. B. Sing, A. Mostavan, E. Hamzah, D. Mantovani, and H. Hermawan. "Degradation behavior of biodegradable Fe35Mn alloy stents". In: *Journal of biomedical materials research. Part B, Applied biomaterials* 103.3 (2015), pp. 572–577.

[SON86] K. Sumiyama, N. Ohshima, and Y. Nakamura. "Magnetic Properties of Metastable α-Mn-Type Mn1-yFey Alloys Produced by Vapor Quenching". In: *physica status solidi a* 98 (1986), pp. 229–238.

[SS10] A. B. Santamaria and S. I. Sulsky. "Risk assessment of an essential element: manganese". In: *Journal of toxicology and environmental health. Part A* 73.2 (2010), pp. 128–155.

[Tho74] J. A. Thornton. "Influence of apparatus geometry and deposition conditions on the structure and topography of thick sputtered coatings". In: *Journal of Vacuum Science and Technology* 11.4 (1974), p. 666.

[Tho77a] J. A. Thornton. "High Rate Thick Film Growth". In: *Annual Review of Materials Science* 7.1 (1977), pp. 239–260.

[Tho77b] J. A. Thornton. "Internal stresses in titanium, nickel, molybdenum, and tantalum films deposited by cylindrical magnetron sputtering". In: *Journal of Vacuum Science and Technology* 14.1 (1977), p. 164.

[Tho86] J. A. Thornton. "The microstructure of sputter-deposited coatings". In: *Journal of Vacuum Science & Technology A: Vacuum, Surfaces, and Films* 4.6 (1986), p. 3059.

[Tos05] K. H. Tostmann. *Korrosion: Ursachen und Vermeidung*. Weinheim: Wiley-VCH, 2005.

[Ulu+14] M. F. Ulum, A. Arafat, D. Noviana, A. H. Yusop, A. K. Nasution, M. R. Abdul Kadir, and H. Hermawan. "In vitro and in vivo degradation evaluation of novel iron-bioceramic composites for bone implant applications". In: *Materials science & engineering. C, Materials for biological applications* 36 (2014), pp. 336–344.

[VKČ15] D. Vojtěch, J. Kubásek, and J. Čapek. "Comparative mechanical and corrosion studies on magnesium, zinc and iron alloys as biodegradable metals". In: *Materiali in tehnologije* 49.6 (2015), pp. 877–882.

[Wan+17a] H. Wang, Y. Zheng, C. Jiang, Y. Li, and Y. Fu. "In vitro corrosion behavior and cytocompatibility of pure Fe implanted with Ta". In: *Surface and Coatings Technology* (2017).

[Wan+17b] H. Wang, Y. Zheng, Y. Li, and C. Jiang. "Improvement of in vitro corrosion and cytocompatibility of biodegradable Fe surface modified by Zn ion implantation". In: *Applied Surface Science* 403 (2017), pp. 168–176.

[Wan+17c] H. Wang, Y. Zheng, J. Liu, C. Jiang, and Y. Li. "In vitro corrosion properties and cytocompatibility of Fe-Ga alloys as potential biodegradable metallic materials". In: *Materials science & engineering. C, Materials for biological applications* 71 (2017), pp. 60–66.

[Wit+08] F. Witte, N. Hort, C. Vogt, S. Cohen, K. U. Kainer, R. Willumeit, and F. Feyerabend. "Degradable biomaterials based on magnesium corrosion". In: *Current Opinion in Solid State and Materials Science* 12.5-6 (2008), pp. 63–72.

[Wit10] F. Witte. "The history of biodegradable magnesium implants: a review". In: *Acta biomaterialia* 6.5 (2010), pp. 1680–1692.

[Yar17] E. Yarar. "Inverse-Bilayer AlN/(Fe90Co10)78Si12B10 Magnetoelectric Composites". PhD thesis. Kiel: Christian Albrechts Universität, 23.11.2017.

[YYM81] E. Yasuo, N. Yasuhisa, and I. Masashi. "Lattice Dynamics and Invar Properties in f.c.c. FeMn Alloy". In: *Journal of the Physical Society of Japan* 50 (1981), pp. 469–475.

[Zam+08] C. Zamponi, H. Rumpf, C. Schmutz, and E. Quandt. "Structuring of sputtered superelastic NiTi thin films by photolithography and etching". In: *Materials Science and Engineering: A* 481-482 (2008), pp. 623–625.

[ZC15] Q. Zhang and P. Cao. "Degradable porous Fe-35wt.%Mn produced via powder sintering from NH4HCO3 porogen". In: *Materials Chemistry and Physics* 163 (2015), pp. 394–401.

[Zhu+09] S. Zhu, N. Huang, L. Xu, Y. Zhang, H. Liu, H. Sun, and Y. Leng. "Biocompatibility of pure iron: In vitro assessment of degradation kinetics and cytotoxicity on endothelial cells". In: *Materials Science and Engineering: C* 29.5 (2009), pp. 1589–1592.

Acknowledgments

Zunächst bedanke ich mich bei Prof. Dr.-Ing Eckhard Quandt für die Aufnahme in die Arbeitsgruppe, sowie für die gebotene Möglichkeit zur Promotion.

Als nächstes möchte ich mich bei der Initiatorin dieses Projektes, Frau Dr. rer. nat. Christiane Zamponi bedanken. Ich freue mich über die Möglichkeit zur Mitwirkung an dem Projekt und bin sehr dankbar für die ausgezeichnete fachliche Betreuung, gegenseitige Motivation und auch die freundschaftliche Zusammenarbeit. Im Zuge Dessen Danke ich ebenfalls der DFG für die Finanzielle Förderung des Projektes.

Auch Prof. Dr. rer. nat. Lorenz Kienle möchte ich an dieser Stelle für die Bereitschaft zur Zweitbegutachtung danken.

Ausdrücklich möchte ich mich bei David Haffner bedanken, da diese Arbeit durch die fachliche Nähe und von vielen produktiven Diskussionen profitieren konnte.
Danke auch an Jan Johansen, Bastian Hirsch, Ana Maria, Victor Schell und Lea Jessen, die durch Ihre Abschlussarbeiten und HiWi Tätigkeit ebenfalls einen wichtigen Beitrag zu dieser Arbeit geleistet haben.
Weiterhin hat diese Arbeit von der Zusammenarbeit, Hilfe und fachlichen Diskussionen einer Vielzahl von (ehemaligen) Kollegen profitiert, daher ein Danke an: Rodrigo, Dirk, Ali, Christoph, Claas, Klaas, André, Antonio, Rahel, Ulli, Gero, Torben, Niklas, Enno, Emanuel.
Auch Bernd Neumann und der gesamten Werkstattcrew danke ich für Ihre immer wieder tolle Unterstützung.
Vielen Dank auch an Gislinde und Jessica, die uns bei der Bewältigung des täglichen Bürokratiewahnsinns immer tatkräftig unterstützten.
Ebenfalls möchte ich der gesamten Arbeitsgruppe für anorganische Funktionsmaterialien für eine angenehme Zusammenarbeit danken.

Explizit ein großes Dankeschön an die Bürokollegen Patrick und Erdem sowie Iris, Christoph, Lars und Volker für die gegenseitige Motivation, super Arbeitsatmosphäre und den vielen manchmal hitzigen Diskussionen vom Substrat über Politik, bis hin zum Universum. Auch den ehemaligen Kommilitonen Arne und Torben möchte ich im Zuge dessen meinen Dank aussprechen.

Nicht zuletzt gilt mein Dank auch meiner Freundin Femke die mir immer zur Seite gestanden hat und mich immer wieder ermutigt und unterstützt hat.
Auch bei meiner Familie, Alexandra, Nils, Alfred, Christian und Stefan, danke ich für die Unterstützung abseits der Arbeit. Mein Dank gilt hier in besonderem Maße meiner Mutter, die mich mein gesamtes Leben, vor allem in schweren Zeiten, immer wenn es nötig war in jeder Hinsicht unterstützt und ermutigt hat.

Abschließend bedanke ich mich bei meinem Vater Ulrich. Die Gespräche und Unternehmungen mit Dir haben mich animiert zu fragen warum Dinge sind wie sie sind. Damit hast du schon frühzeitig zu meinem Interesse an naturwissenschaftlichen/technischen Zusammenhängen beigetragen. Die Zeit die wir hatten, ist somit sicherlich ein Teil der Triebkraft für diese Arbeit.